UNIVERSITÀ DEGLI STUDI ROMA TRE

Dipartimento di Fisica "Edoardo Amaldi"

Dottorato di Ricerca in Fisica - XVI Ciclo

Study of gamma/hadron discrimination in the Argo-YBJ experiment by means of muon identification

Katia Fratini

Coordinatore

prof. Filippo Ceradini

Tutore

prof. Pio Pistilli

April 2003

Introduction

The Argo-YBJ (Astrophysical Radiation Ground-based Observatory at YangBaJing) experiment is located in Tibet, at 4300 meters above the sea level. It is an extensive air-shower particle detector array whose active elements consist in RPCs (Resistive Plate Chambers). One of the main purposes of Argo is the observation and study of γ-ray astrophysical sources in the energy range from about 100 GeV up to tens of TeV.

Ground-based experiments reveal air-showers, namely the products of the cascade originating from the interaction of a primary highly energetic particle (a photon or a hadron) with the nuclei composing the atmosphere. Photon detection suffers from the huge background constituted by ordinary cosmic rays, whose flux is 3 orders of magnitude larger than the typical γ-ray emitter flux.

For the purpose of observing astrophysical sources, which can often be considered as point-like objects, one has to get rid of cosmic rays, which are instead isotropically distributed. Therefore, the sources are surveyed within a suitable solid angle in order to optimize the signal-to-background ratio. Even if the source is point-like, the size of the opening angle is limited by the finite angular resolution of the detector.

The different characteristics of photon-initiated and hadron-initiated showers allow the development of software algorithms and experimental methods capable of further reducing the background component. One of the features differentiating the two kind of showers is their muon content: electromagnetic showers are poor in muons while hadronic ones are rich in them. Exploiting this fact, a technique based on muon identification is being explored by the Argo experiment.

The effectiveness of this technique is expected to raise with the primary shower energy. Indeed, for hadronic cosmic rays, the muon content increases with the energy, while photon-initiated showers continue to be almost lacking of muons. On the other hand, the γ-ray sources flux decreases as a function of the photon energy. Care must be taken when considering this technique: a good rejection could be achieved when the photon flux is too low.

This work is a study aimed at improving Argo sensitivity to source detection at high energy (tens of TeV) by increasing the hadronic background rejection by means of muon identification. An efficient background rejection is of paramount importance in this research field. In order to apply the muon identification technique, an upgrade of the detector with respect to the original project, consisting in the addition of a muon tracker system, is required. Moreover, an increase of the detector active surface is mandatory to work at high energy, because of the lower γ-ray flux.

The effectiveness of the method is studied in the case of photons coming from the Crab nebula, which is the standard "candle" for γ-ray astronomy: the sensitivity to this source at high energy has been estimated exploiting the background rejection allowed by the muon identification. Moreover the application of this rejection technique could be determinant for the observation of the possible end point of the Crab nebula spectrum in the energy region of tens of TeV.

Cosmic rays are almost entirely composed of protons and helium nuclei. Heavier nuclei are present as well. This last component will not be considered in this study, while the helium component will be taken into account by appropriately increasing the number of simulated protons. This leads to a slight underestimate of the total number of muons. With respect to the evaluation of effectiveness of the discrimination method presented in this work, this corresponds to a conservative approach.

This thesis is organised in five chapters. The first chapter presents a summary of the main subjects currently studied in γ-ray astronomy, together with a description of some of the experiments involved in the field. The characteristics of the Crab nebula are reviewed in chapter 2: here, the agreement between all collected data relative to the radiation emission from the nebula, and the theoretical models trying to retract the nebula itself are discussed in order to highlight the questions left open. The Argo experiment (described in chapter 3), in particular if upgraded with the addition of a muon identification system, can contribute in understanding some of them.

The work presented in this thesis required the production of a Monte Carlo data sample. The software used to generate it, is described in chapter 4. Both physical processes concerning the shower development and its simulation by means of the CORSIKA program - the code used by the Argo collaboration - are treated, focussing on the muon production mechanisms, as the capability of discrimination between hadronic and electromagnetic showers strongly depends on the number of muons present in atmospheric showers. The detector simulation program ARGO-G, a GEANT-based code developed by the collaboration, is then described. Details of the production of the generated samples of photon and proton-initiated showers which simulate the Crab nebula emission and the cosmic-ray background are also described in this chapter. In the last chapter, the sensitivity to the Crab nebula at the highest energies is estimated with an upgraded configuration of the apparatus consisting in a larger active surface with respect to the standard setup of the detector. Moreover, a very general muon detection system is considered to operate together with the modified experimental setup, in order to estimate the effectiveness of the background rejection by means of muon identification: thus, the quality factor Q, the quantity which measures this effectiveness, is evaluated using the sample of simulated photons and protons coming from the direction of the Crab nebula. Finally, the improved sensitivity to this source is estimated. The good rejection of the background component achievable with the muon identification technique, allows the study of the Crab spectrum behaviour at the highest energies observable: several scenarios are discussed.

Chapter 1

γ-ray astronomy

γ-ray astronomy, the study of high energy photons coming from the astrophysical sources, is a relatively new field that has only lately become part of mainstream astronomy. In fact, the techniques needed to detect the highest energy photons have only become available in the last 30 years. γ rays are electromagnetic waves which occupy a very broad (in principle, unbounded) range of the electromagnetic spectrum, which extends from several hundreds keV. Therefore γ radiation provides information about the most energetic processes and phenomena in the Universe. Moreover its large energy range allows the study of a wide variety of objects and phenomena.

In order to classify such a large electromagnetic band, a scheme was first proposed by Weekes [1] and then revised by Hoffman [2]. Table 1.1 shows this practical scheme based on the detection techniques used for several intervals in the energy spectrum. In fact, such a large range of energy, cannot be investigated by means of a unique observational technique. There are two main detection methods: the first one consists in revealing γ rays directly, by making use of satellite-based telescopes that convert the photon and track the resulting electron-positron pair to determine the photon direction; the second one consists in detecting the extensive air showers (EASs) produced when photons interact with the Earth's atmosphere, using ground-based instruments. To date satellite experiments have succeeded in detecting photons with energy up to about 30 GeV, while ground-based data lie in the energy range above $\sim$ 100 GeV. Thus there is a lack of data in the energy range from 30 GeV to $\sim$100 GeV and moreover there is no superposition

Energy	Nomenclature	Detection technique
10 - 30 MeV	medium	satellite-based Compton telescope
30 MeV - 30 GeV	high (HE)	satellite-based tracking detector
30 GeV - 30 TeV	very high (VHE)	ground-based atmospheric Čerenkov detector
30 TeV - 30 PeV	ultrahigh (UHE)	ground-based air shower particle detector
30 PeV - and up	extremely high (EHE)	ground-based air shower particle detector

Table 1.1: *γ-ray astronomy nomenclature*

of measurements from the two different kinds of technique. Owing to the continuos efforts aimed at improving the experimental techniques, these limits in the observational energy range and consequently the classification scheme have being changed during the years. Indeed satellite experiments reaching energies of 300 GeV and ground-based experiments with an energy threshold as low as 30 GeV are under construction. The experimental techniques employed in γ-ray astronomy as well as the reasons for the use of these different techniques will be explained in detail in Sec. 1.2.

A very intense experimental activity has brought γ-ray astronomy to become an important branch of astronomy. In the next sections a review of some of the major topics which keep alive the interest in this subject, together with the experiments supporting it, will be given.

1.1 Motivation for the study of high energy γ-ray astronomy

For several decades, cosmic rays were the only known very high energy astrophysical phenomenon: a very interesting and puzzling one, not yet completely understood today. All space detectors, from SAS-II [3] and COS-B [4], launched in the 1970s, to COMPTEL [5] and EGRET [6] aboard CGRO, launched in 1991, were designed primarily for searching cosmic rays acceleration sites and for investigating acceleration mechanisms.

Before EGRET, there were no other known HE phenomena apart from a few pulsars and a single extragalactic source, discovered by COS-B and already identified as an active galactic nucleus (AGN). At the end of the 1980s, results in high-energy γ-ray astronomy were scanty and often somewhat confusing. As far as ground-based observations are concerned, except for the TeV γ rays emission from the Crab nebula (observed by the Whipple group [7]), all other claimed detections of VHE and UHE sources were controversial.

Finally, in the 1990s, the COMPTEL and EGRET telescopes on board CGRO provided the first complete all-sky surveys in γ-ray astronomy in the energy ranges 1-30 MeV and from 100 MeV to $\sim$ 10 GeV, respectively. Figure 1.1a shows the all-sky map of γ-ray sources detected by EGRET [8]: seven high energy γ-ray pulsars have been observed; a new class of sources, high energy γ-ray blazars, has been identified; high energy sources which are not detected at other wavelengths constitute a catalog of about 50 "unidentified" objects. Besides, in the same decade, more than eight earth-based detectors confirmed the TeV emission from the Crab Nebula, giving credibility to the existence of sources of TeV γ-rays. A map, as of January 2003, of the known TeV γ ray emitting sources is shown in Fig. 1.1b [9]. This map represents a catalog of fourteen objects, among which there are confirmed and probable sources together. The confirmed sources (A) are those objects detected by multiple experiments at high significance levels: Crab, Markarian 421, Markarian 501, PSR 1706-443, H1426+428, and 1ES 1959+650. The probable sources (B) are the eight sources detected at a high significance level by at least one group: Vela, 1ES 2344+514, SN1006, Cassiopeia-A, RXJ 1713-3846, TeV J2032, PKS 2155-304, and NGC 253. These sources are classified as 3 pulsar nebulae, 3 supernova remnants, 1 starburst galaxy, 6 AGN, and 1 unknown. All AGN are of the BL-Lac type, and all confirmed AGN detections have so far been made in the northern hemisphere. The possible sources (C) are two other sources which have been claimed: Centaurus X-3, and 3C66A.

All these measurements reveal that the phenomenon of γ-ray emission is typical of the most compact and energetic objects in the Universe, like pulsars, accreting X-ray binaries and supernova remnants in the Milky Way and active galactic nuclei in the extragalactic spaces. The present knowledge about some of these interesting objects, together with

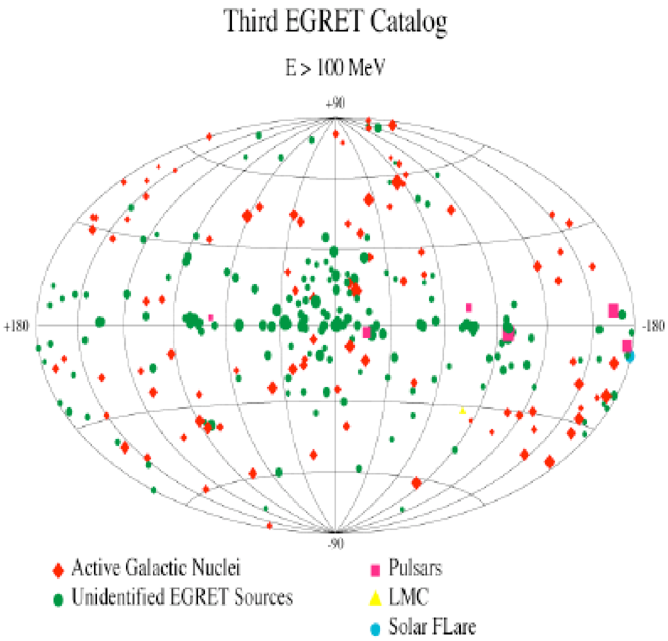

(a)

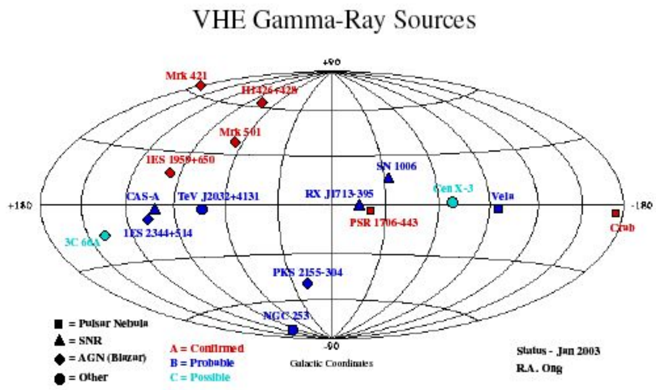

(b)

Figure 1.1: *γ-ray sky from the Third Egret Catalog (a) and VHE Sky Map, as of January 2003 (b).*

the cosmic rays problem, will be discussed in the next subsections, focussing on their emission in the VHE energy region, with the purpose of highlighting the questions left open.

1.1.1 The puzzle of the cosmic ray origin and acceleration mechanism

Even today, almost 100 years after the first observations of cosmic radiation, the question of its origin and acceleration mechanisms is one of the main motivating items for the study of γ-ray astronomy.

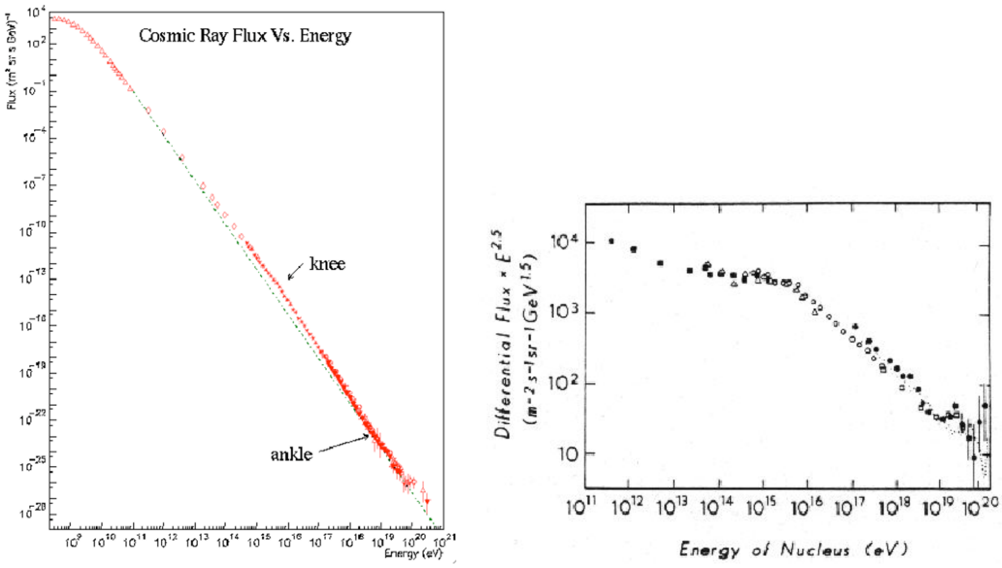

Figure 1.2: *Cosmic ray spectrum as observed at the top of the atmosphere (a): in particular, the energy range from 10^{11} up to 10^{20} eV is shown (b).*

Cosmic radiation is composed by 98% of protons and nuclei, and by about 2% of electrons. Of the former component, about 87% are protons, 12% helium nuclei and the remaining 1% are heavier nuclei. The elemental composition is still today an open question. Figure 1.2a shows the observed cosmic rays spectrum at the top of the atmosphere. It extends up to 10^{21} eV, covering more than 10 orders of magnitude in energy. It can be well represented by a power law function as

$$N(E)dE = KE^{-\alpha}dE \tag{1.1}$$

where α is the spectral index. Its value is between 2.5 and 2.7 up to $10^{15} \div 10^{16}$ eV. Then the slope of the spectrum changes twice, as highlighted in Fig. 1.2b: the first change is in fact at $10^{15} \div 10^{16}$ eV and it is called "the knee", while the second one is "the ankle" at about 10^{19} eV. The origin of these features are not yet understood, however all theoretical models which try to explain the cosmic ray origin and their acceleration mechanism must include them. Among the several hypotheses [10], there are the fact that some of the acceleration mechanisms, but not all, can stop to act and the fact that the propagation mechanism can change.

Charged cosmic particles bend in presence of magnetic fields: the bending radius R (expressed in pc) of a particle with charge Z (in unit of electron charge) and momentum p (in PeV/c), traveling in a magnetic field B (in μG) is $R = \frac{0.01 \cdot p}{z \cdot B}$. The magnetic field in our galaxy is $\sim 1\ \mu$G and it is roughly parallel to the local spiral arm, but with large fluctuations. Thus, even for protons of energy equal to 10^{19} eV, coming from some galactic source 10 kpc far from Earth, the origin direction is completely lost.

Therefore one way to get information about cosmic rays origin is to observe the high energy photons (which do not bend in presence of magnetic fields) produced in their interaction with matter. This is not the best way to investigate on cosmic ray origin because photons can be also generated as a consequence of the acceleration of the electrons. Moreover, high energy photons interact with photons of the infrared radiation background and with the cosmic microwave background to create electron-positron pairs. This effect suppresses any possibility of surveying the sky at distances greater than 100 Mpc with high energy ($>$10 TeV) gamma rays (Sec. 1.1.5). Neutrinos from astrophysical sources are instead a clear evidence of hadron acceleration. The acceleration of protons to energies as high as 10^{20} eV, whatever the accelerator object, must generate a flux of photo-produced mesons, which decay to yield gamma rays and neutrinos.

Nearly the totality of the cosmic rays flux is thought to be of galactic origin: only the highest energy cosmic rays, in typical galactic magnetic fields, have a bending radius whose value is larger than the size of the galaxy. These could be of extragalactic origin. Supernova remnants (SNRs) are thought to be the favourite candidates for the source of cosmic rays with energy up to about $Z \cdot 10^{14}$ eV, where Z is the nuclear charge of the particle. Two are the main arguments:

- The power required to produce all galactic cosmic rays can be estimated to be $L_{CR} = \frac{v_D \cdot \rho_E}{\tau_r} \simeq 5 \cdot 10^{40}$ erg/s, where v_D is the volume of the galactic disk, ρ_E is the local energy density of cosmic rays, τ_r is their residence time in the volume v_D. Supernovae can supply $L_{SN} \simeq 3 \cdot 10^{42}$ erg/s [11]. Thus an acceleration mechanism with an efficiency of a few percent could be provided by supernovae blast waves.

- The theory (diffusive shock acceleration [12] [13] [14]) which explains the mechanism that converts the energy expelled in the explosions into accelerated particles, provides a power low spectrum with index equal to 2.1 at the source, which is consistent with the local power law index observed ($\sim$ 2.7) due to the effect of propagation.

What about the rest of the cosmic rays? Compact sources, owing to their higher (with respect to the supernovae) magnetic fields, could be able to accelerate particles up to energies many orders of magnitude greater than 100 TeV, the value acquired via the shock acceleration mechanism by supernovae blast waves. The power required to energise the tail of the cosmic rays spectrum is significantly smaller than the total power because of the steepening of the spectrum. Thus even one or two powerful point sources could be important.

However, up to the present day, all detected sources are most likely electrons accelerators: there is no evidence of hadronic production of γ rays, in spite of the fact that the ratio of the number of primary protons to the primary electrons is $\frac{N_p}{N_e} \approx 100$. So, where are the cosmic rays sources?[11]

1.1.2 Active galactic nuclei

Galactic nuclei (like galaxies themselves) are composed of stars and interstellar matter (mostly gas, plus small dust grains). An active galactic nucleus (AGN), is one in which processes are observed that cannot be readily explained by the mere presence of normal stars and interstellar gas clouds.

Active galaxies can be distinguished from the ordinary ones by means of observational differences:

1. The images of normal galaxies are basically an assembly of stars, while the images of active galaxies show bright nuclei.

2. Normal galaxies radiate most of their energy, interpreted as the sum of the starlight in the optical band. On the contrary the overall active galaxy spectrum is often dominated by nonthermal emission, and characterised by optical broadened emission lines and luminosity maxima in IR, UV, X-rays or even γ-rays.

3. Normal galaxies look always the same apart from when a supernova explosion occurs, while active galaxy emission changes significantly on short time scales, down to days or even less.

These objects are classified according to their observational properties (both optical and radio), thus creating a big number of classes and subclasses: quasars (quasistellar radio sources), Seyfert galaxies (types 0,I and II), optically violent variables, etc. Seyfert galaxies, discovered by the homonymous astronomer, are unresolved bright cores (star-like) that emit broad optical emission lines: more in detail Seyfert type I galaxies show both broad and narrow emission lines, type II only narrow emission lines and type 0 weak emission line or even no emission line at all. AGNs are called radio-loud when the ratio of the radio emission flux at 5 GHz to the emission flux in the optical B range ("blue") is such that $\frac{f_{5GHz}}{f_B} \geqslant 10$, otherwise they are called radio-quiet. The scheme in Tab. 1.2 summarises this classification of AGNs owing to both their optical emission

Radio loudness	Optical emission line properties		
	Type 2 (narrow lines)	Type 1 (broad lines)	Type 0 (weak/absent)
Radio-quiet (85-90%)	Seyfert 2	Seyfert 1 QSO	
Radio-loud (10-15%)	NLRG (FR I, FR II)	BLRG SSRQ, FSRQ	Blazars (BL Lac, FSRQ)
	Decreasing jet angle to line of sight $\Longrightarrow$		

Table 1.2: *Classification of AGNs. The main types of AGN are sorted in this table [15].*

lines (horizontal direction) and their radio emission (vertical direction). The distinctions in the horizontal direction are thought to be due to a viewing effect, while the cause of distinction in the vertical direction, i.e. radio-loud or radio-quiet, is still unknown.

A theoretical model [16] unifies most of these classes, explaining them as the same object observed from different viewing angles. Figure 1.3 shows this unified AGN model. Despite the fact that many details are not yet understood, this scheme is commonly ac-

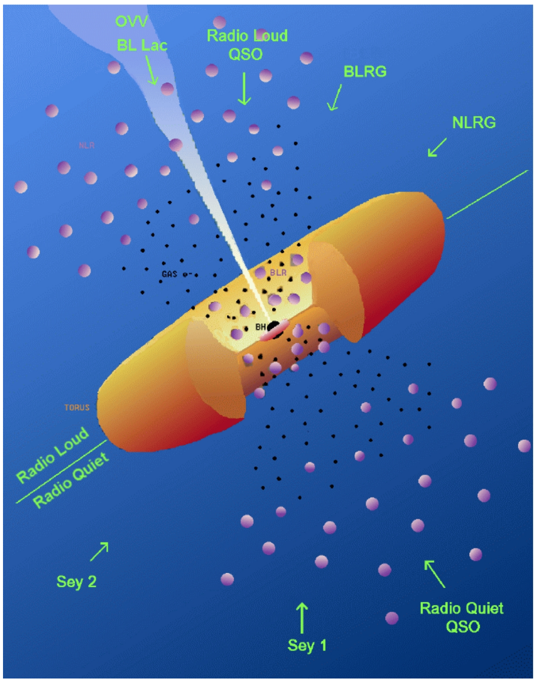

Figure 1.3: *Picture of the AGN unified model. Above the torus axis, a radio-loud AGN is drawn: the jet is visible. Below the axis, a radio-quiet AGN is shown. Credit: M. Urry and P. Padovani (Space Telescope Science Institute)*

cepted because it explains the major observational facts reasonably well and consistently. The central engine of an AGN is thought to be a supermassive black hole with masses of the order of $10^7 - 10^{10} M_\odot$. The black hole sucks up stars and gas from the surrounding galaxy to form a thin accretion disk consisting of ionised material, which is surrounded by a thick torus of gas and dust lying in the equatorial plane of the hole. Accretion is a very efficient process: it may convert 10% of the rest mass of accreted matter into radiation. Within the molecular torus and near the center of the active galaxy there are fast moving ($v \geqslant$ 2000Km s^{-1}) gas clouds which are ionised by the accretion disk radiation and which emit the observed broad emission lines (this is why they are known as Broad Line Region). Further out other clouds move slower ($v \leqslant 2000$ km s^{-1}) and therefore give rise to the observed narrow emission lines (Narrow Line Region). In radio-loud AGNs, strong jets of relativistic particles emanate perpendicular to the plane of the accretion disk. Although the exact mechanism of how these jets are formed is unknown, it is believed that TeV emission originates in them. They are thought to be composed of relativistic particles and to cause from radio to high-energy γ emission.

This general structure is assumed for all AGNs, which constitute roughly 3% of all galaxies: thus, the several types of AGNs correspond to the different spatial orientations of the same object with respect to line of sight of the observer. Two are the phenomena which determine the observational properties at different viewing angles:

- The shadowing of the torus, which obscures indeed certain emission regions from direct view.

- The relativistic jets observed at small view angles determine the relativistic beaming of the emitted radiation and also the superluminal motion which has been revealed in many AGNs. The relativistic beaming cause the apparent luminosity radiation to increase:

$$L_{app} = D^n \cdot L_{int} \tag{1.2}$$

  where D is the Doppler factor and n is a model-dependent factor which for current emission models assumes values between 3 and 4. The Doppler factor is defined as:

$$D = \frac{1}{\Gamma(1-\beta\cos\theta)}, \qquad \beta = \frac{v_{jet}}{c}, \qquad \Gamma = (1-\beta^2)^{-\frac{1}{2}} \tag{1.3}$$

  where v_{jet} is the speed of the jet, c the velocity of the light and θ is the jet orientation angle with respect to the observer's line of sight. Also the time variability of the AGN emission is an effect of the relativistic beaming because of the Doppler contraction of the time scale.

Figure 1.4 summarises the connection between viewing angle and observational properties. When a radio-loud AGN is observed at large angles with respect to the jet axis, the torus hides the clouds located near the center of the active galaxy, while the distant clouds

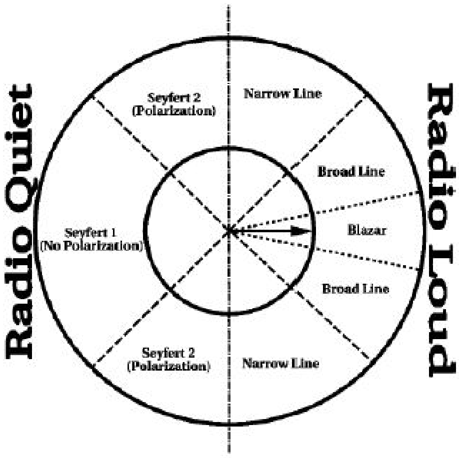

Figure 1.4: *The AGN subclasses. The right side of the circle gathers the radio-loud AGNs: the arrow represents the jet direction. The left side describes the radio-quiet classification.*

which move slower, can still be seen: therefore narrow emission lines are observed. Moving the line of sight closer to the rotational axis of the AGN, also the faster clouds become visible and broad emission lines appear to the observer. BL Lacertae objects or a quasars are radio-loud AGNs observed towards the "central engine". Also the temporal variability of the emitted signal depends on the viewing angle: the time interval of variability decreases as the viewing angle becomes smaller. For the radio-quiet objects, a Seyfert Type I galaxy or a QSO is seen for viewing angles at which both the narrow and broad line regions are visible. At larger angular offsets the broad line region will be hidden by this extended molecular torus, giving rise to Seyfert Type II galaxies.

AGNs emit radiation over the entire electromagnetic spectrum from radio waves to TeV γ rays. Thermal emission originates from the accretion disk (infrared to X rays) and the torus (infrared). The nonthermal emission (radio to γ ray) comes from the jets. As far as γ-ray emission is concerned, blazars were found occasionally to be emitters of this kind of radiation, some nearby BL Lac objects up to TeV energies. Although the γ-ray production mechanism is widely believed to be the inverse Compton scattering off soft photons by relativistic electrons, the nature of the accelerated primary particles which constitute the jets is still unknown. Depending on the nature of these accelerated primary particles, leptonic (electrons and positrons) or hadronic (mainly protons) models have been developed. Considering different origins for the soft target photons, there are various subclasses of these models.

1.1.3 Pulsars

Pulsars are astrophysical objects whose peculiarity is to emit pulsed radiation. They are thought to be very strongly magnetised rotating neutron stars. Very recently pulsars have been found in globular clusters. They are believed to have been formed there by accretion of matter onto white dwarf stars in binary sistems. Other pulsars, like the Crab are born in supernova explosions. The possibility of the existence of neutrons stars was postulated very soon after Chadwick's discovery of the neutron in 1932. In 1934, Baade and Zwicky tentatively linked supernovae with the collapse of ordinary stars to neutron stars, and the first theoretical models for neutron stars were developed by Oppenheimer and Volkoff in 1939. However, there was surprisingly little astronomical and theoretical interest in neutron stars until the accidental observational discovery of pulsars by Hewish and Bell in 1967.

Pulsars emit pulses of radiation at short and remarkably regular intervals. Many pulsars have been observed with periods ranging from milliseconds to seconds. The regularity of pulses is phenomenal: observers can now predict the arrival times of pulses a year ahead with an accuracy better then a millisecond.

The principal argument for the identification of pulsars with rotating neutron stars is based upon the shortness of the pulsar periods. The only possibility for so rapid and so precise a repetition is for the star to be rapidly rotating and emitting a beam of radiation which sweeps round the sky like a lighthouse, pointing towards the observer once per rotation. The only kind of star which can rotate fast enough without bursting by its own centrifugal force is a neutron star. The rotational period is not constant: on long time scales pulsars are observed to slow down.

The most likely mechanism explaining the loss of energy by means of radiation emission, in a rotating neutron star, is magnetic dipole radiation. There is a compelling historical argument in favour of magnetic dipole radiation as a mechanism for energy loss from pulsars: assuming this mechanism in action, the inferred age for the Crab Pulsar is consistent with the date of the supernova explosion which produced the Crab Nebula, 1054 AD (see Chapter 2). To account for the observation of radiation pulses, the magnetic axis of the neutron star and its rotation axis must be misaligned. In this case, the spinning magnetic dipole emits electromagnetic radiation; for a star with magnetic dipole m at an angle θ to an angular velocity ω, energy is radiated at a rate given by [17]

$$\frac{dE_{rad}}{dt} = \frac{2}{3c^3}\left[\frac{\mu_0}{4\pi}\right] m^2\omega^4 \sin^2\theta \tag{1.4}$$

The radiation generated by the misaligned rotating dipole causes loss of rotational energy and accounts for the observed slowdown. Figure 1.5 shows this model of pulsars.

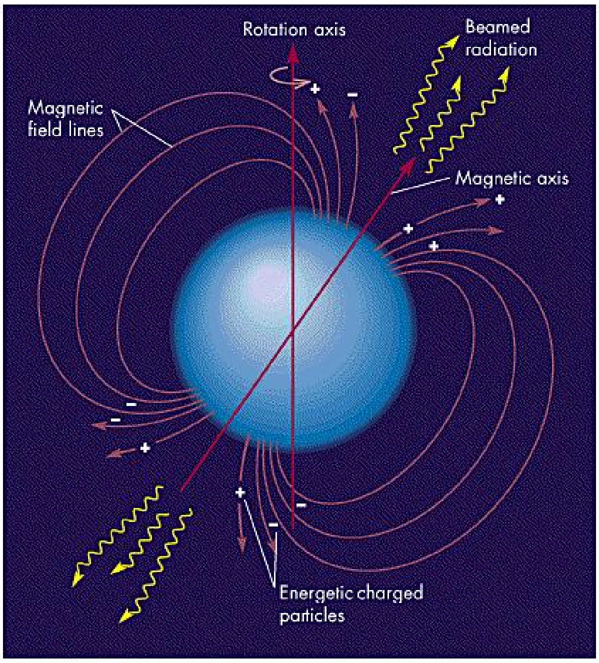

Figure 1.5: *Scheme of a pulsar*

The pulse periods of pulsars can be measured with very high accuracy, and one of the most important parameters is the rate at which the pulse period changes with time. Indeed, for most pulsars, the rate at which the pulse period increases can be measured and this can be used to derive an age estimate. The slowing down can be described by a *braking index*, n [18], which is defined by

$$\dot{\omega} = -K\omega^n \tag{1.5}$$

The braking index provides information about the energy loss mechanism slowing the rotation of the neutron star. The braking index for magnetic dipole radiation is $n = 3$. If I is the moment of inertia of the neutron star, we can write its energy of rotation as $E_{rot} = \frac{1}{2} I\omega^2$ and this decreases in accordance with

$$\frac{dE_{rot}}{dt} = I\omega\frac{d\omega}{dt} \tag{1.6}$$

Eq. 1.4 and Eq. 1.6 yield $\frac{d\omega}{dt} \propto -\omega^3$. Direct measurement of the braking index *n* can be made if the second derivative of the pulsar angular frequency $\ddot{\omega}$ can be measured:

$$n = \frac{\omega\ddot{\omega}}{\dot{\omega}^2} = 2 - \frac{P\ddot{P}}{\dot{P}^2} \tag{1.7}$$

where P is the period of the pulsar. Braking indices have been measured for a number of pulsars and not always it resulted n=3. Thus, although the magnetic braking may be the cause of the deceleration in some cases, it cannot be the only one. Part of the deceleration can also be associated with torques exerted on the neutron star by the outflow of particles which also remove angular momentum from the star. The age of the pulsar can be estimated if it is assumed that its deceleration can be described by a constant braking index throughout its lifetime. Integrating Eq. (1.5)

$$\tau = \frac{1}{K(n-1)}\left[\frac{1}{\omega^{n-1}} - \frac{1}{\omega_0^{n-1}}\right] \tag{1.8}$$

where τ is the age of the pulsar and ω_0 is its initial angular velocity. If $n > 1$ and $\omega_0 >> \omega$ the age of the pulsar is found to be $\tau = \frac{P}{(n-1)\dot{P}}$. It is conventional to set $n = 3$ to calculate the age of pulsars.

The fastly variable magnetic field generated by the rotating magnetic dipole produces an electric field. Positive and negative particles in the conducting pulsar experience the Lorentz force in opposite directions. Moreover this charge separation generates an electric field which opposes to the electric field induced by the variable magnetic field in such a way that no permanent currents flow inside the conductor. Outside the star the fastly variable magnetic field produces such a huge electric field at the pulsar's surface, that the electric force on a charged particle (either ion or electron) is much stronger than the force of gravity. Charged particles are ejected from the neutron star's surface and fill the pulsar magnetosphere, where they rearrange themselves in the same way as the internal charges of the star until the electric and magnetic forces are in equilibrium. The following condition is satisfied.

$$\vec{E} + \frac{\vec{\omega}\Lambda\vec{r}}{c}\Lambda\vec{B} = 0 \Leftrightarrow \vec{E}\cdot\vec{B} = 0 \tag{1.9}$$

Thus the magnetic field lines are very nearly electric equipotential in this zone. The charged particles in the magnetosphere move along the magnetic field lines which rotate rigidly with the star's angular velocity. The magnetosphere terminates at the light cylinder where the speed of the corotating particles reaches the velocity of light c. Beyond the light cylinder the particles, which cannot exceed the speed of light, are spun away. Field lines trying to extend across the radius of the light cylinder are forced to open to the outside. The charged particles moving along the opened magnetic field lines nearby the

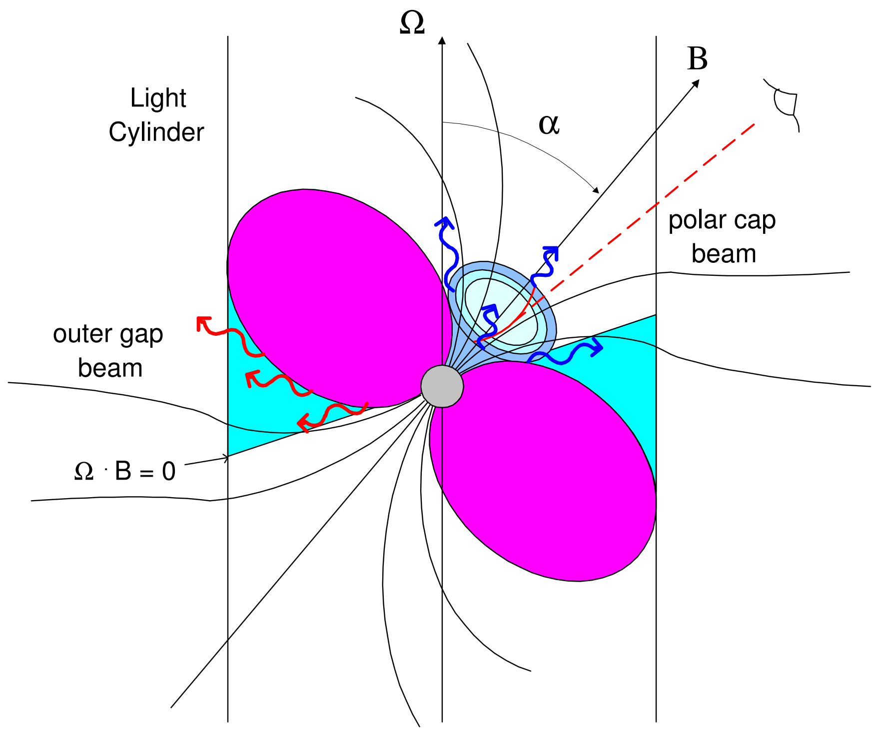

Figure 1.6: *Scheme of a pulsar*

magnetic poles are rapidly accelerated to relativistic speeds by the induced electric field which is no more counterbalanced by the plasma electric field. As these lines are curved, relativistic electrons emit curvature radiation. Therefore, acceleration can take place only in regions not filled with plasma. These regions are thought to be created near the magnetic poles and near the light cylinder as shown in Fig. 1.6. Pulsed emission from radio to GeV γ-rays is believed to originate from these "vacuum gaps". This description of the environment surrounding the pulsar is important for the plerion system which will be discussed in the next section.

1.1.4 Supernova Remnants

Supernova remnants are those objects produced by the violent explosions of massive stars at the end of their life. This explosion, called a supernova, is one of the most energetic events in the universe, and causes a single star to briefly outshine the entire Galaxy in which it is located: the observed kinetic energy of the debris formed in the explosion is typically 10^{44} J and the optical energy output during the year following the explosion is of $\approx 10^{42}$ J [17].

These explosions are primarily classified according to their optical spectra with particular attention to the presence or absence of spectral lines associated with hydrogen.

It is widely accepted that two are the causes to have a supernova explosion: either the gravitational collapse of the dense core of a massive star at the end of its evolution or the explosive thermonuclear burning of a less massive but equally dense white dwarf which is accreting matter from a nearby companion in a binary system.

Notwithstanding these events are quite rare (one or two times every hundred years on average in the galaxy), they are really interesting and important. Such an enormous explosion produces primarily three effects. First, the ISM (InterStellar Medium) is strongly modified together with the distribution of the surrounding gas and dust. Second, cosmic rays acceleration seems to be related to supernovae (Sec. 1.1.1). Moreover the remnants from these explosions eventually cool and form interstellar matter from which new stars can born. Finally supernovae are also important for the distribution of the heavier elements throughout interstellar space.

Most of the SNRs appear to be almost circular in shape with a brightened edge. This may suggest the simplest hypothesis of a progenitor star embedded in a uniform medium. Thereafter, fragments ejected from a spherically symmetric supernova explosion expand rapidly into a medium of uniform and constant matter density, sweeping up the surrounding matter. A low-density region is left in the interior and behind the expanding shell.

Three phases characterise the life of a SNR.

1. The "free" expansion: the mass of the swept-up material is negligible compared to the mass of the ejected one, and the expansion proceeds at uniform velocity. The total ejected mass might be 1 $M_{\odot}$ and the density of the surrounding medium 0.3 atoms cm^{-3}. If so this phase will last until the radius is 3 pc, when the swept-up mass becomes equal to that of the ejecta. If the initial velocity is 15000 km s^{-1}, the age of the remnant at this time will be 200 yr. The velocity of the ejected stellar mass is much larger than the speed of the sound in the assumed uniform ISM. A shock wave consequently forms at the leading edge of the ejecta. Atom caught by the shock will be ionised and the temperature increases to 10^7-10^8 K. All the material is propelled outward, in the direction of the shock.

2. As time passes the expansion slows and the SNR enters an adiabatic expansion: "Sedov phase" or "blast wave phase". The mass of the swept-up material is large compared to the mass of the original ejected one, but the energy radiated by the material in the shell is still small compared with its internal (kinetic) energy. As the SNR expands, its mass becomes larger and cooler because it sweeps up cold ISM.

3. Eventually, after the cooling of the material in and behind the shock, the "radiative phase" is reached, when most of the internal kinetic energy is radiated away.

The SNR radiation emission ranges from radio to γ-rays. As far as the γ-ray emission is concerned, this is mainly caused by four processes, namely π^0 production in ion-ion collisions, electron bremsstrahlung, inverse-Compton scattering and synchrotron emission of electrons in the SNR magnetic field. γ-ray emission from π^0,

$$p + p \rightarrow \pi^0 X \rightarrow \gamma\gamma X$$

peaks at the beginning of the Sedov phase and then slowly decays with the SNR evolution in time. The intensity of this kind of emission depends on the possible presence of a dense molecular cloud in the neighbourhood of the SNR, which acts as a target. The expected γ-ray spectrum is very hard. The other three processes involve electrons: primary electrons are directly accelerated in the shock, secondary electrons and positrons come from the decay of charged pions produced in pp and pα collisions. The density of the secondary electrons and positrons, n_{sec}, is much smaller than that of the primary electrons (n_{pr}): $n_{sec} \sim n_{pr}\frac{t_{SNR}}{t_{pp}}$, where t_{SNR} is the age of the SNR and $t_{pp} \sim (n_p c \sigma_{pp\rightarrow\pi^\circ X})^{-1}$ is the time-scale for collisions involving 1 GeV protons that result in pion production plus anything else, which is typically $\sim 10^7$ yr, while $t_{SNR} \sim 10^5$ yr. Therefore the contribution of the secondary electrons to the bremsstrahlung, inverse-Compton scattering and synchrotron emission of SNRs is negligible. The photons produced by means of the bremsstrahlung process are due to electrons scattered off the ambient gas, while the inverse-Compton radiation is composed by the upscattered photons of the synchrotron emission, of the IR/optical background photons and of the cosmic microwave background (CMB).

Three basic types of SNRs are generally known: the shell-type SNRs, the Crab-like SNRs and the composite SNRs.

Shell-type SNRs

The shock wave which generates from the supernova explosion expands, hitting any interstellar material it encounters, thus producing a big shell of hot material in space. The radiation emission which mainly extends from radio to X-ray is generated by this hot shell, not by the whole volume of the SNR. Figure 1.7 shows an example of shell-type remnants: the Tycho SNR, which reveals the ring-like structure whose appearance is explained by the fact that there is more hot gas along the line of sight to the shell-remnant edge than to its center. Shell-type remnants constitutes more than 80% of all SNRs.

Crab-like SNRs

The Crab Nebula, as can be seen in left side of Fig. 1.8, is approximately spherical with a filled center. The radiation emission is from the whole volume of the object. This kind of remnants are called plerions. The appearance of a plerion is thought to indicate

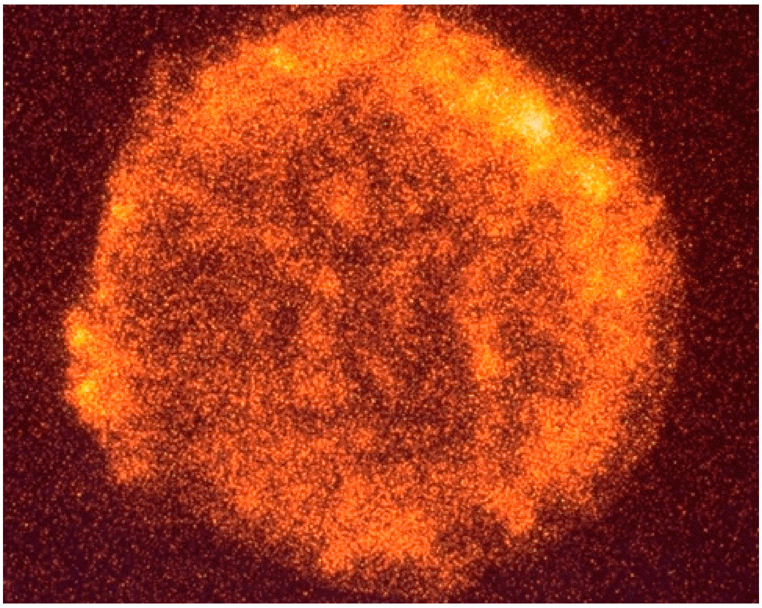

Figure 1.7: *Image of the X-rays emitted by the Tycho's supernova remnant, made by a telescope onboard the ROSAT spacecraft.*

the presence of a pulsar. The middle picture in Fig. 1.8 shows a Hubble Space Telescope image of the inner parts of the Crab: the pulsar is visible as the left one of the pair of stars near the center. Surrounding the pulsar is a complex of sharp knots and wisp-like

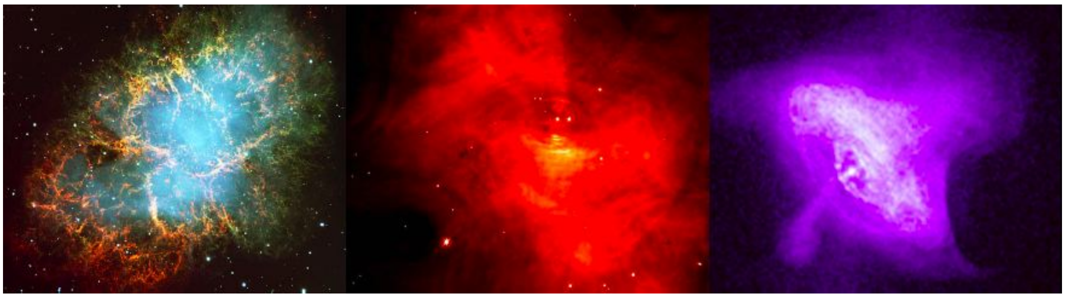

Figure 1.8: *Some images of the Crab nebula: the first one has been taken from one of the telescopes which consitutes the Very Large Telescope [19]. The color indicates what is happening to the electrons in different parts of the Crab Nebula. Red indicates the electrons are recombining with protons to form neutral hydrogen, while blue indicates the electrons are whirling around the magnetic field of the inner nebula. The second one shows a Hubble Space Telescope image of the inner parts of the Crab [20]. The pulsar itself is visible as the left of the pair of stars near the center of the frame. Surrounding the pulsar is a complex of sharp knots and wisp-like features. The third one is a Chandra X-ray image [21].*

features. In the outer regions of the Crab nebula many emission lines, including the red glow from hydrogen, are present.

Pulsars have already been described in Sec. 1.1.3. Figure 1.9 shows a pulsar together with the surrounding SNR. Outside the magnetosphere there is the pulsar region wind, where the magnetic field lines are open and charged particles can be accelerated. The wind region terminates at the shock front beyond which there is the nebular region. The magnetic field lines close in the nebular zone (they cannot penetrate the interstellar gas because of its high electrical conductivity).

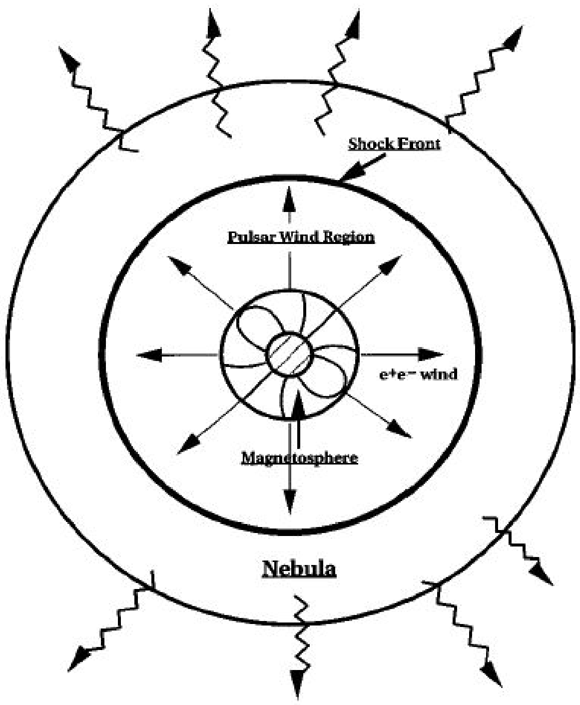

Figure 1.9: *Schematic diagram of a plerion.*

The relativistic wind of electrons interacts with the nebular magnetic field causing synchrotron radiation to be emitted. Moreover, high energy electrons interact by inverse Compton scattering with their own synchrotron emission (SSC, synchrotron self-Compton model [22]) and also with the other photon fields present in the nebula. These are the two main mechanisms which characterise the emission spectrum from the Crab nebula, which will be discussed in detail in the next chapter.

Composite SNRs

This kind of SNRs is a cross between the first and the second type of remnants discussed. A composite SNR appears as a shell-like shock-heated hot gas with a small central synchrotron nebula. It appears either shell-like or Crab-like, depending on the region of the electromagnetic spectrum in which it is observed. Often it is believed that the shock wave is moving out making the shell while the hot gas still fills the central part of the SNR. The Vela SNR is an example of such composite SNRs: observed at X-ray energies, it shows a central source with a 1′ diameter synchrotron nebula around it, while it shows very high energy γ-ray emission as a plerion at the Vela pulsar birth position with a possible extended nebula around it.

1.1.5 Interactions with the diffuse extragalactic background radiation

The diffuse extragalactic background radiation (DEBRA) consists in different components:

- the cosmic microwave background (CMB), a thermal radiation at a temperature of 2.7 K which fills the whole space;
- the diffuse radio noise;
- the cosmic infrared and optical background (EBL, extragalactic background light), a thermal emission produced respectively by dust and stars during the evolution of the Universe.

Photons from γ-rays sources can interact with the diffuse photons background by means of the reaction:

$$\gamma\gamma- > e^+e^-$$

This reaction sets a limit on the distance γ-rays can travel, causing the universe to be more or less opaque to them, depending on their energy. Its threshold is $2m_e^2 \simeq 0.5 \cdot 10^{12}$eV^2. Figure 1.10 shows the mean free path λ for γ rays versus their energy E. The behaviour is essentially determined by the intensity of the photon background and the

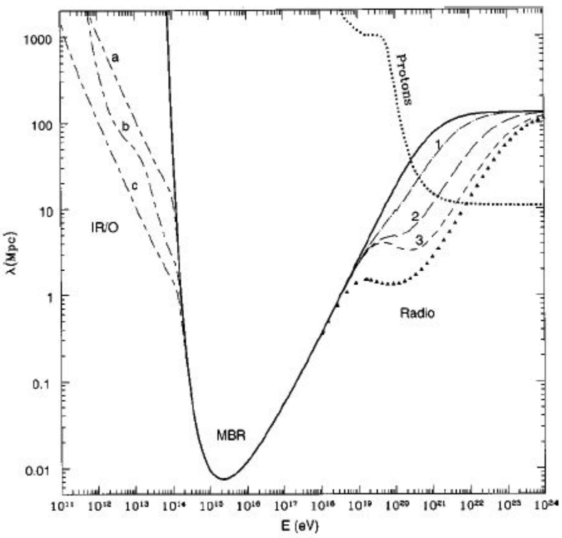

Figure 1.10: *γ-ray mean free path as a function of their energy E.*

cross section expression which is maximised at

$$\epsilon(E) \simeq \frac{2 \cdot m_e^4}{E} \simeq 0.5 \left(\frac{1\text{TeV}}{E} \right) \tag{1.10}$$

where ϵ is the energy of the soft photon, while E is the γ-ray energy. Therefore, from Eq. 1.10 IR light (0.1eV) and CMB (at 10^{-4}eV) absorb TeV and PeV γ-rays respectively. Beyond 10^{20}eV the universe has regained some transparency to γ-rays.

At TeV energies the universe opacity is determined by the EBL. This component of DEBRA is not yet directly measured. It could provide cosmological information about the formation epoch and evolution of galaxies. Because of the γ-rays absorption mechanism, an indirect measurement of the strength of the EBL can be inferred by the observation of appropriate sources.

1.2 Experiments working on γ-ray astronomy

Photons from γ-ray astrophysical sources, depending on their energy, have to be detected either outside the atmosphere, before interacting with it, by devices located on space vehicles or on the Earth, at sea level or at high mountain altitude, after their interaction with the atmosphere. The interaction of photons and hadrons with the atmosphere is described in some detail in Chapter 4. Figure 1.11 shows the plot of the γ-ray shower size (number of charged particles which develop in the air-shower) as a function of the atmospheric depth or of the altitude at several values of the primary energy: γ-rays with energy larger than 10^{11} eV have low probability to be detected on Earth. The atmosphere is opaque to HE photons and to some of the VHE photons, depending on the observational altitude. In this energy range instruments working outside the atmosphere are needed. On the other hand, the flux of γ-ray sources is typically very low and decreases

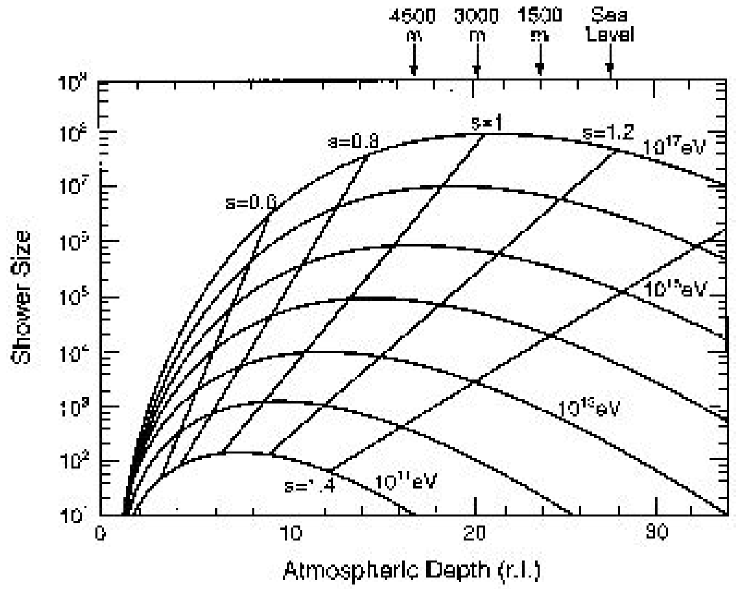

Figure 1.11: *Shower size as a function of the atmospheric depth for photon-initiated showers. The values of the energy showed on the curves are the photon primary energies.*

rapidly with the energy: therefore, in order to observe a statistically significant sample of VHE and even higher energy photons, detectors with an effective area larger than 10^4 m^2 are needed. The higher the photon energy, the larger the detection surface required. Such extended detectors can be built only on Earth. The sensitivity of satellite-based detectors is limited by the detection area they can support which is of the order of 1 m^2.

A serious problem for this kind of measurements is the huge background constituted by the hadronic cosmic radiation. Figure 1.12 shows the grand-unified photon spectrum and the cosmic rays spectrum. The background flux is three order of magnitude larger than the integral γ-ray flux. γ-rays are unambiguously identified with satellite based

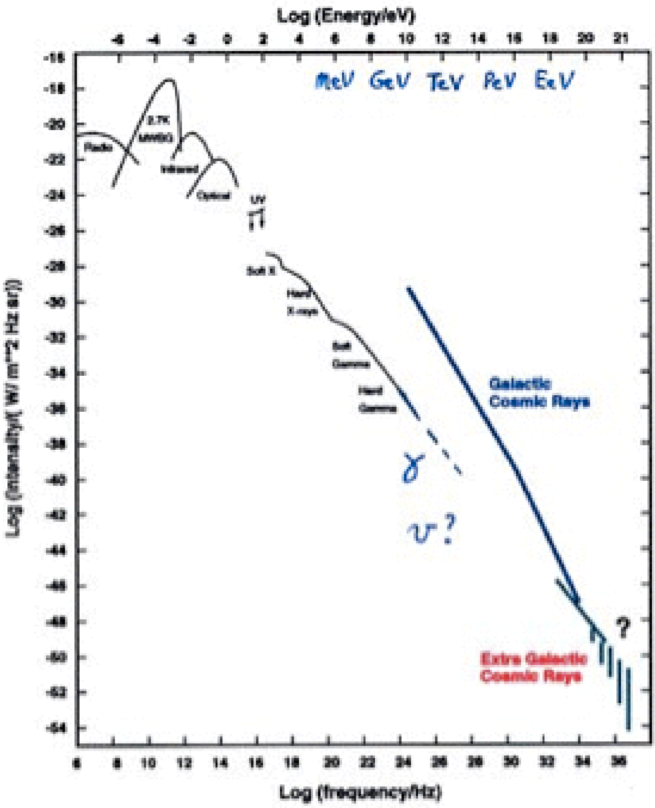

Figure 1.12: *A sketch of the grand-unifed photon spectrum and the cosmic ray spectrum.*

experiments, while the rejection of background using ground-based detectors is more involved.

A space-borne γ-ray detector consists in:

- a particle detector in which photons interact, converting into an electron-positron pair, whose tracks are recorded;
- a calorimeter in which the electrons and positrons release their energy;
- an anti-coincidence detector usually constituted by a thin sheet of scintillator, surrounding the tracker to reject charged cosmic rays.

EGRET, one of the most successful satellite-experiment, operated in the energy range from 20 MeV to 30 GeV with an energy resolution of about 20%, an angular resolution improving from $\sim 10°$ at 60 MeV to $\sim 0.5°$ at 10 GeV, an effective area of ~ 1000 cm^2 at several hundred MeV and a field of view of ~1.5 sr. It reached a 3σ sensitivity limit of $\sim 10^{-7}\mathrm{cm}^{-2}\mathrm{s}^{-1}$ [15] (see Fig. 1.18)

Along the last decade, ground-based detection has become an effective investigation method. They make use of an indirect technique: the primary particle, a photon from the source observed or a cosmic ray, interacts with the atmosphere, producing a lot of secondary particles which in turn interact with the atmosphere. The extensive air-shower thus formed can be detected by observing:

1. the secondary particles arriving on the ground;
2. Čerenkov light emitted by charged secondary particles;
3. fluorescence light emitted by charged secondary particles.

These particle signals are observed by means of different experimental techniques which are summarised in Fig. 1.13 and briefly described in the next sections.

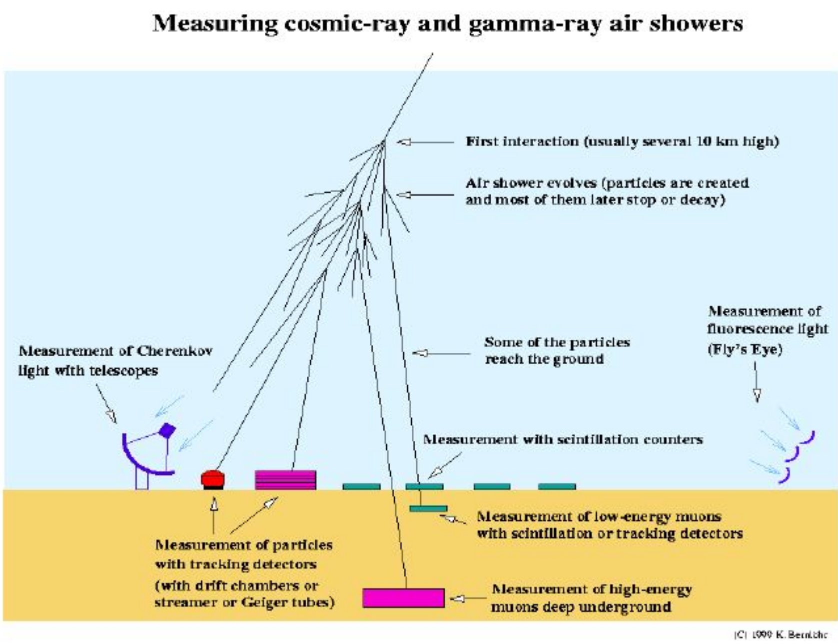

Figure 1.13: *Summary of the experimental techniques used in order to detect γ-ray and cosmic-ray air showers.*

In order to understand what are the relevant features that determine how ground-based detectors work to optimise their functioning, the general expression for the signal-to-noise ratio as a function of the parameters of the detector is considered:

$$\left(\frac{\text{signal}}{\text{noise}}\right) \propto \frac{R_\gamma Q\sqrt{A^{\text{eff}}T}}{\sigma_\theta} \tag{1.11}$$

where A^{eff} is the effective detector area, T is the exposure time, σ_θ is the angular resolution, R_γ is the relative γ/hadron trigger efficiency, Q is the γ/hadron identification efficiency. The signal-to-noise ratio is a linear function of Q and R_γ. The development of atmospheric air-showers for primary photons and protons with fixed energies has been simulated [23] in order to study the longitudinal development as a function of the altitude and then to give an estimate of the quantity R_γ. Figure 1.14 shows the results. Apart from

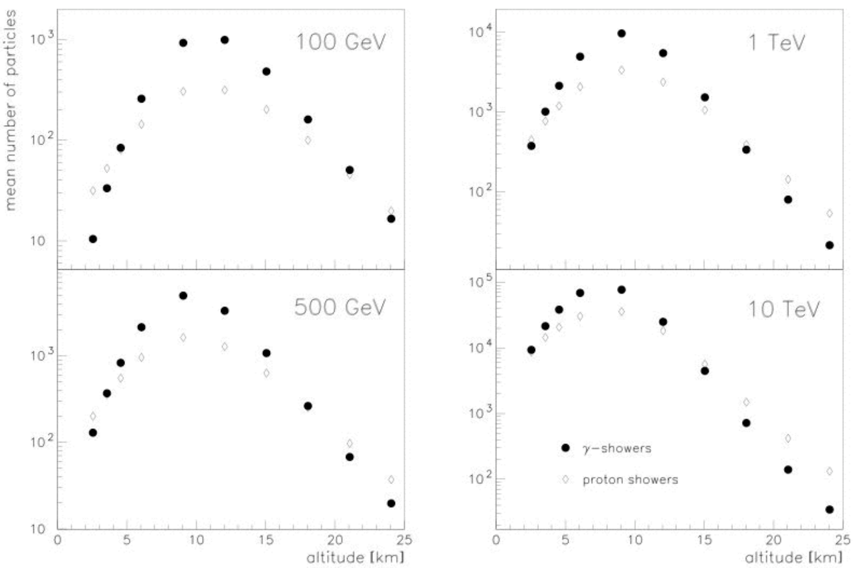

Figure 1.14: *Mean number of particles (γ, $e^\pm$, $\mu^\pm$, hadrons) as a function of the altitude for air-showers generated by protons and photons with several primary energies*

the small number of particles reaching the ground, which set tight limits on observations at the lower energies, at low altitude the number of particles present in proton-induced cascades is larger than that in γ-induced showers. This implies that the trigger probability is such that the effective area is larger for protons than for photons, thus giving a ratio of γ-ray to proton trigger efficiency, R_γ, of less than 1. This ratio favourites γ-ray earth-observation at altitudes above 4000 m.

The signal-to noise ratio improves with the square root of exposure and linearly as the angular resolution gets better. Thus, the angular resolution is a really important characteristic of the detector. Ground-based photon observations suffer from the difficulty to separate γ rays from charged cosmic rays, since there is no veto against charged particles as can be done around a compact detector in space. A good angular resolution is essential for this kind of devices. Indeed the uniformly distributed background is reduced when observing a point source within a solid angle of such an aperture so as optimize the signal-to-background ratio.

1.2.1 Atmospheric Čerenkov telescopes (ACTs)

The indirect detection of charged secondaries by Čerenkov light gives access to much lower γ energies: the light propagates with limited absorption down to the ground while charged secondaries interact again and get absorbed. Most of the earth-based detector currently taking data, are Atmospheric Čerenkov telescopes (ACTs) and they have been used with great success in the energy region from 250 GeV to 10 TeV. They detect Čerenkov photons emitted by relativistic charged particles developing in an EAS, which travel faster than the speed of light in air. The simplest configuration of such a detector is one parabolic or spherical mirror with diameter size between 2 and 10 meters, collecting the Čerenkov light which is then reflected to an array of photomultiplier tubes (PMTs), placed in the focal plane of the mirror. Array of Čerenkov telescopes also exist. Some of the existing telescopes are listed in Tab. 1.3 with their main characteristics.

γ-ray observation with these instruments is affected not only by the cosmic ray background but also by the night-sky background, which amounts to about 1 photon ns^{-1} m^{-2}, mostly from the Milky Way. The ratio between the Čerenkov signal S and night-sky background B can be expressed as:

$$\frac{S}{\sqrt{B}} = \frac{A\rho_\gamma\epsilon}{\sqrt{\Phi_B \Omega A \epsilon t}} = \frac{\rho_\gamma}{\sqrt{\Phi_B}}\sqrt{\frac{A\epsilon}{\Omega t}} \tag{1.12}$$

where A is the collecting area, ρ_γ is the photon density on the ground, ϵ the efficiency of light collection, Φ_B the night-sky background flux, t the width of the trigger time window

Experiment	Site	$N_{tel} \times$ Area (m^2)	Pixels	E_{thr} (GeV)
Whipple	Arizona	$1\times$ 75	109	250
7 TA	Utah	$7\times$ 3	3 $\times$ 256	250
Cangaroo	Australia	$1\times$ 30	512	300
HEGRA	Canaries	$5\times$ 8.5	271	1000 (1 t.)
NARRABRI	Australia	$3\times$ 42	91	300
CAT	France	$1\times$ 18	546(+50)	250
TACTIC	India	$1\times$ 18	349	300

Table 1.3: *Existing ACTs [24]*

and Ω the solid angle subtended by each photomultiplier. Equation 1.12 evidences that in order to improve the Čerenkov light detection, the area A must increase while the time t and the solid angle Ω must be as small as possible. The mirror size is mainly limited by costs. Fortunately, some characteristics of the atmospheric Čerenkov light facilitate its detection:

1. Most of the air-shower Čerenkov light is produced by charged particles near the shower maximum development, which occurs at a height of between 10 and 7 Km a.s.l. for gamma rays of energies between 100 GeV and 10 TeV. At this altitude the Čerenkov angle is about 1° and it mostly determines the extension of the area illuminated on the ground.

2. The Čerenkov radiation front is thin. At ground it results in a pulse of duration $<$5 ns.

3. The wavelength emission spectrum varies as λ^{-2}, where λ is the photon wavelength. Therefore, much of this light is in the ultraviolet band (short wavelengths), while the night sky light peaks at long wavelengths.

The success of ACTs in detecting γ-ray sources relies on the techniques developed to reject the huge cosmic ray background. These techniques exploit two features:

- The cosmic ray background is uniformly distributed, while the γ-rays come from the source direction which is followed by the telescope. Thus the incident direction of the air-shower is reconstructed in order to reject those events whose reconstructed direction does not match with the source direction.

- The Čerenkov light distribution is different between γ-initiated shower and proton-initiated one.

The imaging technique utilises a pixel camera, placed at the focal plane of the mirror collecting the light, constituted of an array of PMTs. The orientation in the focal plane and the shape of the images thus inferred allow the reconstruction of the arrival direction and the discrimination of the signal against the background. The image formed is circular for a shower falling directly on the detector and it becomes elliptical with the major axis pointing towards the center of the camera for showers arriving parallel to the optical axis but displaced from the telescope by some distance on the ground. On the contrary, a shower arriving at an angle tilted relative to the optic axis produces an ellipse whose major axis is not pointing to the center of the camera. This axis forms an angle called α with the axis which point from the center of the ellipse to the center of the camera. The angle α is shown in Fig. 1.15 together with a schematic example of the image collected by means of the photomultipliers in the mirror focal plane. The α angle distribution for cosmic-rays events is uniformly distributed, while the same distribution for the signal shows a peak at zero. In Fig. 1.15 also other parameters which provide background rejection are shown.

With the wavefront timing technique, the arrival time of the Čerenkov pulses is measured by large arrays of moderate size telescopes, each instrumented with a PMT. The wavefront has an approximately conical shape. A fit to the arrival times gives the arrival direction of the shower. These array of telescopes also discriminate against the cosmic ray background by sampling the lateral distribution. Much of the discrimination is done at the trigger level, since the overall trigger is usually determined by requiring a minimal Čerenkov signal in a number of different reflectors.

The high capability in rejecting the cosmic-ray background is the main feature of Čerenkov detectors. Their angular resolution is better than 0.15°. Their energy threshold, which is determined by the number of Čerenkov photons required to detect a signal, is at present several hundreds of GeV. The small field of view, few degrees, and the low duty

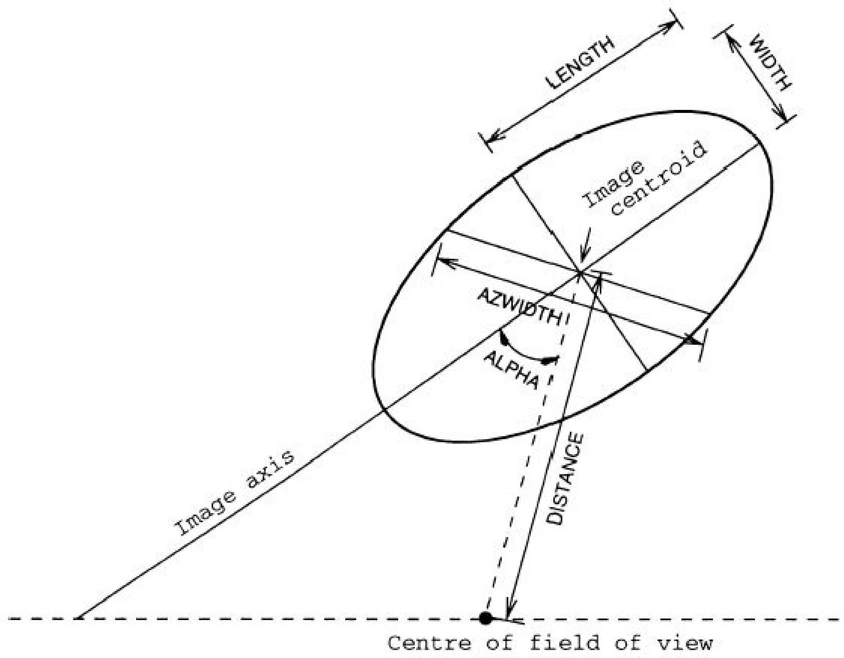

Figure 1.15: *Schematic view of the shower image seen by a Čerenkov telescope. Some parameters useful for background rejection are shown.*

cycle penalise this kind of detectors, which however achieve very high sensitivities (see Fig. 1.18).

From the first successful detection of the Crab nebula by the Whipple experiment [25], few other observatories have reached comparable sensitivity by means of smaller collection mirrors, either exploring a stereoscopic multi-telescope technique, as in the case of HEGRA, or a higher resolution imaging, as in the case of CAT [26] and CANGAROO. Both kinds of improvement will be implemented by the HESS [27], VERITAS [28] and CANGAROO-III [29] experiments. The MAGIC [30] experiment is based on highly improved imaging. Some of the future ACTs are listed in Tab. 1.4.

1.2.2 Extensive air-shower particle detector arrays

Primary particles entering the atmosphere, interact with it; so do the products of the first and subsequent interactions: a particle cascade, called air-shower, is thus generated. The shower front can be assumed to be a thin disk with a diameter of the order of 100 m.

Experiment	Site	$N_{tel}\times$ Area (m^2)	Pixels	year of first light
Cangaroo III	Australia	$4\times$ 57	512	2001 (2003)
HESS	Namibia	$4(16)\times$ 100	800	2002 (2004)
VERITAS	Arizona	$7\times$ 75	499	2005
MAGIC	Canaries	$1(\rightarrow 2)\times$ 220	800	2002
MACE	Canaries	$4\times$ 57	800	2007

Table 1.4: *Future ACTs [24]*

This disk lays in the plane approximately defined by the leading particles in the front. The arrival direction of the primary particle is assumed to be perpendicular to this plane.

Extensive air-shower particle detector arrays (EAS-PADs) sample the charged particles of the shower front at ground level. They generally consist of a certain number of charged-particle detectors, like scintillation counters, each ~ 1 m^2 in size, spread over a large area, more than 10^3 m^2, in order to obtain statistically significant photon samples since source fluxes are expected to be small.

The area of the individual detectors and their spacing determines the energy threshold of the apparatus. Moreover these parameters are important in determining the angular resolution of the array. The accuracy of shower angle determination results from a compromise between the desire for a large lever arm (i.e. large detector spacing) and the need to sample the shower front in a region of sharp arrival time distribution.

The primary incident direction can be inferred by the measured relative times at which the array detectors are hit. Thus the accuracy in the measurement of the primary direction is related to the accuracy of the relative time measurements and to their total number:

$$\sigma_\theta \propto \frac{\sigma_t}{\sqrt{\rho}} \tag{1.13}$$

where σ_t is the time resolution and ρ is the density of independent detector elements sampling the shower front. Thus, fast-timing array detectors are needed, with a time accuracy comparable to the fluctuations in the arrival times of the shower particles. Once the detector area is larger than the typical lateral extension of air showers, thus providing an optimal lever arm, the angular resolution can be further improved by increasing the sampling density.

Another important parameter of an air-shower detector is its threshold energy. It is generally defined as the primary energy at which the trigger probability reaches either 10% or 50%. It depends on the minimum number of counters required in order to reconstruct the events, on the size and spacing of the array detectors and on the location altitude. Usually at least about ten counters are required for a good accuracy in the direction reconstruction. The energy threshold is not a well-defined quantity. Figure 1.16 shows

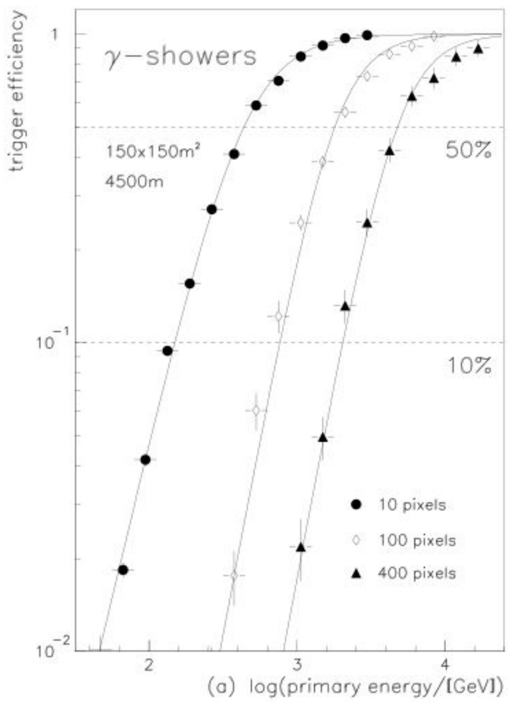

Figure 1.16: *Trigger efficiency as a function of the primary particle energy for three trigger conditions.*

the trigger probability of air-showers as a function of the primary energy. The function describing this relation is not a step-function because of the fluctuations involved in the development of the atmospheric shower, mainly due to the altitude of the first interaction point, and also to the core position and to the incident angle. The energy threshold which is possible to reach by a certain apparatus, lowers with altitude. Figure 1.17 shows the shower size as a function of the altitude relative to electromagnetic showers for several primary energies. The primary energy of electromagnetic showers with a given size which is possible to observe lowers as the altitude increases. Also some experiments are indicated in the figure: CASA, HEGRA and Tibet ASγ, whose energy threshold is lower and lower. They use the sampling technique for their apparatus, i.e. the base detectors are spaced. At a given altitude the implementation of the full coverage technique allows lower energy thresholds to be reached: at Yanbajing site (4300m a.s.l.), a threshold of few hundreds of GeV can be obtained.

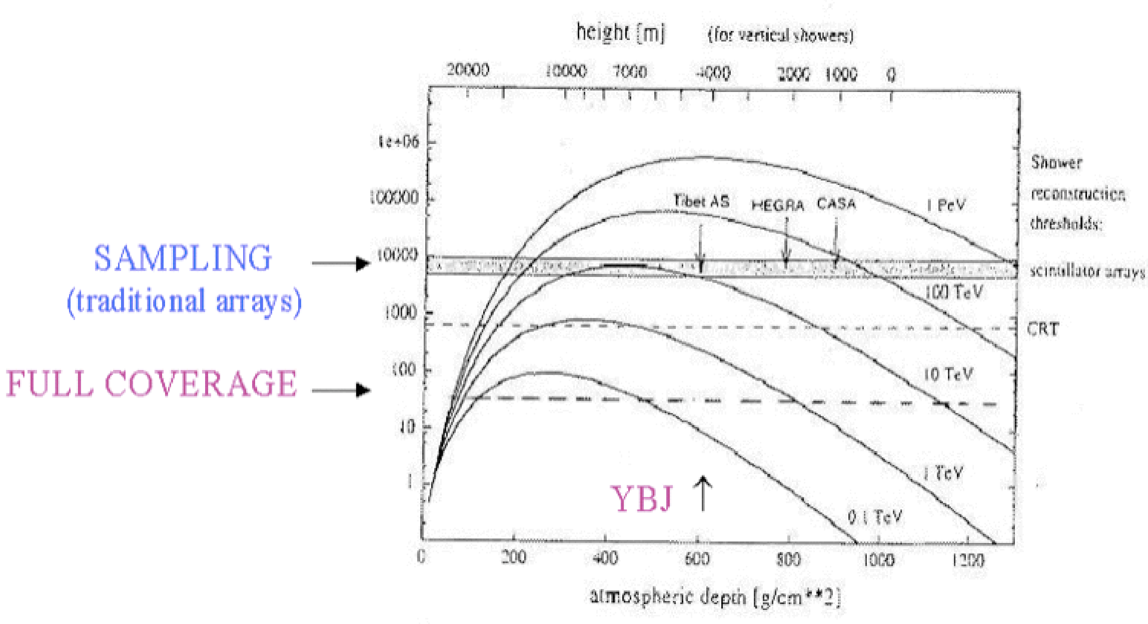

Figure 1.17: *Shower size as a function of the atmospheric depth for photon-initiated showers. The values of the energy showed on the curves are the photon primary energies. See text for details.*

The higher energy regions (VHE and above regions) of γ-ray astronomy are not very well explored: to date only six astrophysical sources are unambiguously known to emit electromagnetic radiation in the VHE range, and no sources in the regions above. Till now no systematic survey of the VHE γ-ray sky has been performed owing to the fact that all VHE detections have been made by means of air-Čerenkov telescopes, which only have a ~5-10% duty cycle and relatively narrow field of view ($\sim 10^{-2}$ sr) for observations. Unfortunately this research field is poor of data. Extensive air-shower particle detector arrays can provide a continuous monitoring of the VHE γ-ray sky and large field of view.

1.2.3 Air-fluorescence detectors

This technique relies on the fact that an ionising particle can excite N_2 molecules in the atmosphere. Such excited molecules can then emit fluorescence photons, typically within 10 to 50 ns after excitation. Most of the light is emitted in the wavelength band between 3000 an 4000 Å which is characterised by an attenuation length of approximately 15 Km for a vertical beam of light. The fluorescence yield per particle is small, about 5 photons m^{-1} electron^{-1} but mildly dependent on altitude and atmospheric temperature[31]. The photon signal, like for the Čerenkov telescopes must be detected in presence of night-sky background photons. The fluorescence of nitrogen in the atmosphere is an isotropic source of radiation. Therefore the number of secondary shower particles needed to detect a signal is larger than the one required for beamed radiation such as Čerenkov light. As a consequence of that, air fluorescence detectors have energy threshold of the order of 10^{18} eV and effective apertures of 10-100 Km^2. On the other hand, this peculiarity allows the detection of EHE cosmic rays. The very low flux of highly energetic cosmic rays need to be detected with huge effective volumes which cannot be reached by means of beamed signature.

Fly's Eye [32] was the first air fluorescence detector to produce significant physics results. It consisted of two systems of 67 spherical mirrors of 1.5 m diameter each viewed by a set of 12-14 photomultipliers. Each photomultiplier observed a different 5.5° hexagonal region of the sky. Isotropically emitted fluorescence light from an EAS was detected by those tube whose solid angle intersects the EAS. The relative arrival times of this light as well as the total integrated light, were recorded for each tube. The amount of light detected by each phototube could be related to the number of electrons in the shower at a specific level of the development of the shower. Unlike other detectors this technique allows the direct measurement of the longitudinal development of the EAS.

1.3 Summary and future

The observations performed during the 1990s have greatly enriched the map of the high energy sky. First of all, CGRO surveys have proved the existence of a lot of γ-ray sources emitting in the HE energy range, both galactic and extragalactic. The VHE sky was surveyed mainly by Čerenkov telescopes and therefore only a small fraction of it has been investigated. Indeed it is data-starved apart from the detection of a few sources. No evidence of UHE emission from bright souces has been found either steady or episodic.

However these years mark the success of the ground-based detection technique. For the first time a source, the AGN Mrk 501, has been discovered by the ground-based experiments before observations in space. Moreover the Crab Nebula emission up to 50 TeV has been detected.

The current efforts are aimed to improve VHE detector technique. Lower energy threshold in the field of the ground-based technique, will be reached by STACEE [33], CELESTE [34] and Solar-2 [35]. Thus the energy region from 30 GeV to 300 GeV will be surveyed and satellite and ground-based measurements could finally be compared. MILAGRO [36] and ARGO belong to the EAS-PAD category. They are designed to reach lower energy threshold than the previous air-shower particle detectors. Their sites are at altitude of about 2000 m a.s.l. and 4300 m a.s.l., respectively therefore the ARGO experiment should reach a lower energy threshold than Milagro. Their advantages are the large field of view and the high duty cycle. These two characteristics allow the continuous monitoring of the VHE sky. The future Čerenkov experiments are HESS, CANGAROO-III, VERITAS and MAGIC. On the low energy side (<1TeV) they will complement the GLAST mission and will overlap with the solar arrays. At the highest energies to which they are sensitive they overlap with the Tibet-ASγ. They will cover the same energy range as MILAGRO and ARGO but with a greater sensitivity. On the other side the MILAGRO's and ARGO's large field of view and high duty cycle will allow the discovery of new sources or the monitoring of transient sources which can be studied in more detail by the Čerenkov detectors. Figure 1.18 shows the sensitivities of some of these experiments with respect to the Crab nebula flux.

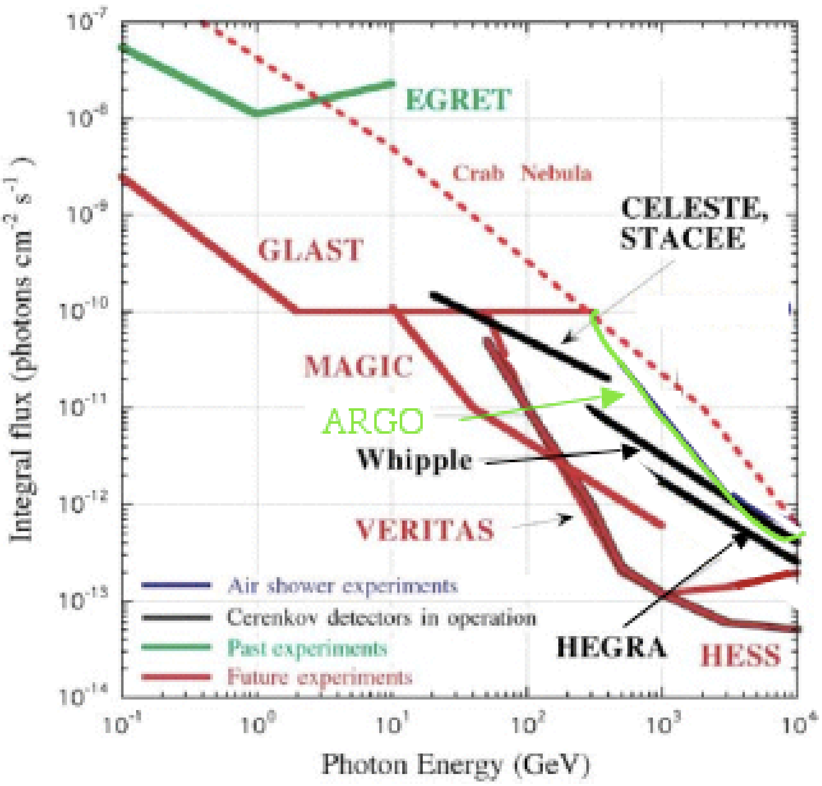

Figure 1.18: *Comparison of the point source sensitivity of some experiments involved in γ-ray astronomy. Cerenkov telescopes sensitivities (Veritas, MAGIC, Whipple, Hess, Celeste, Stacee, Hegra [37]) are for 50 hours of observations. Large field of view detectors sensitivities (EGRET, GLAST, ARGO) are for 1 year of observation [38].*

Chapter 2

The Crab Plerion

The supernova explosion that created the Crab plerion was seen in the Taurus constellation on about July the 4th 1054 AD. It was recorded by Chinese astronomers and probably also by Anasazi Indian artists (in present-day Arizona and New Mexico), as findings in Navaho Canyon and White Mesa (both AZ) as well as in the Chaco Canyon National Park (NM) indicate. It happened at a distance of about 6,000 light-years and it was about four times brighter than Venus. According to the records, it was visible in daylight for 23 days, and 653 days to the naked eye in the night sky.

The nebulous remnant from this explosion was discovered by John Bevis in 1731, while Charles Messier independently found it on August 28, 1758. This nebula was named the "Crab Nebula" after a drawing made by Lord Rosse about 1844.

On November 9, 1968, a pulsating radio source, the Crab Pulsar (also catalogued as NP0532, "NP" for NRAO Pulsar, or PSR 0531+21 since its coordinates are RA 5.35 and Dec 22.01), was discovered in the object M1 of the Messier catalogue by astronomers of the Arecibo Observatory 300-meter radio telescope in Puerto Rico. It is the rotating neutron star that survived the explosion of the original star, placed about at the center of the Crab nebula. Its period is 33 ms.

2.1 Characteristics of the Crab plerion.

The Crab plerion is the system composed by the Crab nebula and the Crab pulsar located inside it. The theory describing plerions has already been summarised in chapter 1. The Crab pulsar is slowing down; its angular frequency, $\omega = 190 \ \mathrm{s}^{-1}$, is not constant, but changes at a rate given by

$$\frac{d\omega}{dt} = -2.4 \times 10^{-9}\mathrm{s}^{-2} \tag{2.1}$$

Few observations which seem to confirm that the system observed in that location is a plerion are:

1. The rate of loss of rotational energy of the Crab pulsar calculated with Eq. 1.6 (assuming a moment of inertia consistent with the estimate given for a neutron star $\sim 10^{38}$Kg m^2 [17]), is $4.6 \cdot 10^{31} W$.This energy loss is comparable with the estimated luminosity of the Crab nebula, $5 \cdot 10^{31} W$ [17]. It is therefore highly likely that the power lost by the rapidly rotating neutron star is the source of the luminosity of the Crab nebula.

2. The age of the Crab pulsar can be estimated using Eq. 1.8, supposing that the mechanism responsible for the radiative energy loss is magnetic dipole radiation and thus assuming the braking index n to be equal to 3. The constant K appearing in Eq. 1.8 can be calculated using the current values for the angular frequency and its rate. The Crab pulsar has been rotating in the crab nebula for a time t bounded by

$$t < \frac{1}{2K\omega^2} = 4 \times 10^{10}\mathrm{s} = 1253 \text{ years} \tag{2.2}$$

value that is consistent with the historical age of the Crab nebula.

2.2 Observations of the Crab

The Crab is a cornerstone of high energy astrophysics. It has been observed throughout the electromagnetic spectrum to emit both pulsed and unpulsed radiation which are thought to be from the pulsar and the nebula respectively. The Crab nebula is so far the unique case in which the energy spectrum has been revealed over almost twenty decades of photon energies: the unpulsed radiation emission has been observed from radio to TeV energies. The nebula is powered by the collapsed residual star, the Crab pulsar, which is observed to emit photons with energies from radio up to $\sim$ GeV. Pulsed radiation is thought to be caused by the electrons of the pulsar wind which are accelerated along the opened magnetic field lines, emitting curvature radiation. These electrons reach the shock front behind the nebular region where they are further accelerated. This latter acceleration mechanism lets the electrons reach energies of the order of tens of PeV. Therefore the radiation emitted as a consequence of the electron shock acceleration has a higher energy. The current collected data seem to form an energy unpulsed spectrum up to 50 TeV and maybe beyond.

The observation of the Crab nebula is fundamental not only to understand the mechanisms through which its emission is produced, but also for calibration of the various γ-ray astronomy experiments. Above all, the Crab nebula can be detected from both the hemispheres. Moreover, its steady emission is particularly suitable to this aim. It is thus called the “standard candle”. Its observation allows the comparison of the results obtained by the many experiments operating at these energies. Using this emission as a test beam, the localization of a source position and the cosmic-ray rejection can be refined.

2.2.1 VHE unpulsed radiation detected by ground-based experiments

Data from satellite-based and ground-based detectors are summarised in Fig. 2.1. Of course, the satellite experiments, Gris, COMPTEL and EGRET, observed the low energy spectrum, up to about 20 GeV, while the ground-based experiments gave their contribution to the high energy spectrum, starting from about 200 GeV.

In 1989 Whipple was the first ground-based experiment providing a detection of the unpulsed radiation coming from the Crab nebula [7]. It is an observation at a 9σ confidence level. In spite of that, because of the quite new detection technique, which observes the γ-ray emission through the products of their interaction with the atmosphere, the question of the calibration was settled. Indeed, the measured flux is too intense to match with the extrapolated values of the lower, either pulsed or unpulsed, energy spectrum. Another detection by the Themistocle experiment, which used the wavefront timing tech-

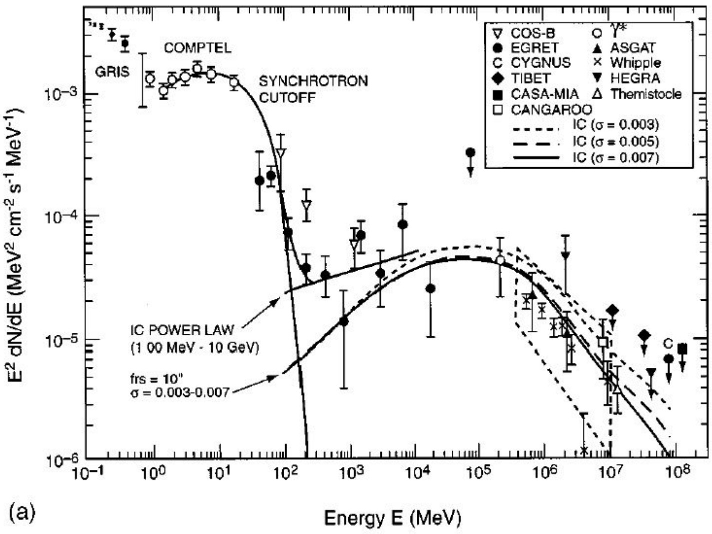

Figure 2.1: *The observed energy spectrum from the Crab nebula.*

nique instead of the imaging one, confirmed the Whipple data[39]. There was no evidence of pulsed radiation, so the emission was thought to be from the nebula.

Thus was clearly established by ACTs that a new process was responsible for the production of the most energetic photons. Ever since, a number of other groups detected the unpulsed emission from the Crab nebula: Hegra and Cangaroo experiments used the imaging technique[40] [41], Tibet-ASγ CASA-MIA CYGNUS ASGAT are EAS-PADs. The results obtained by Čerenkov telescopes are consistent with each other. On the contrary, those coming from the Tibet array provide a higher value for the Crab flux. Apart from the CANGAROO experiment which extends its measurements up to 50 TeV, the other VHE detectors observed the crab spectrum up to about 10 TeV. With the exception of Tibet-ASγ, all cited air-shower experiments are off-line. They have a quite high energy threshold and thus they measured upper limits to the Crab flux. There is no conflict between these UHE upper limits and the current theoretical model.

Tibet

The detection of the Crab nebula by the Tibet-ASγ Collaboration in 1999 [42], was the first detection of γ-ray signals from point sources with an EAS-PAD. The detector,

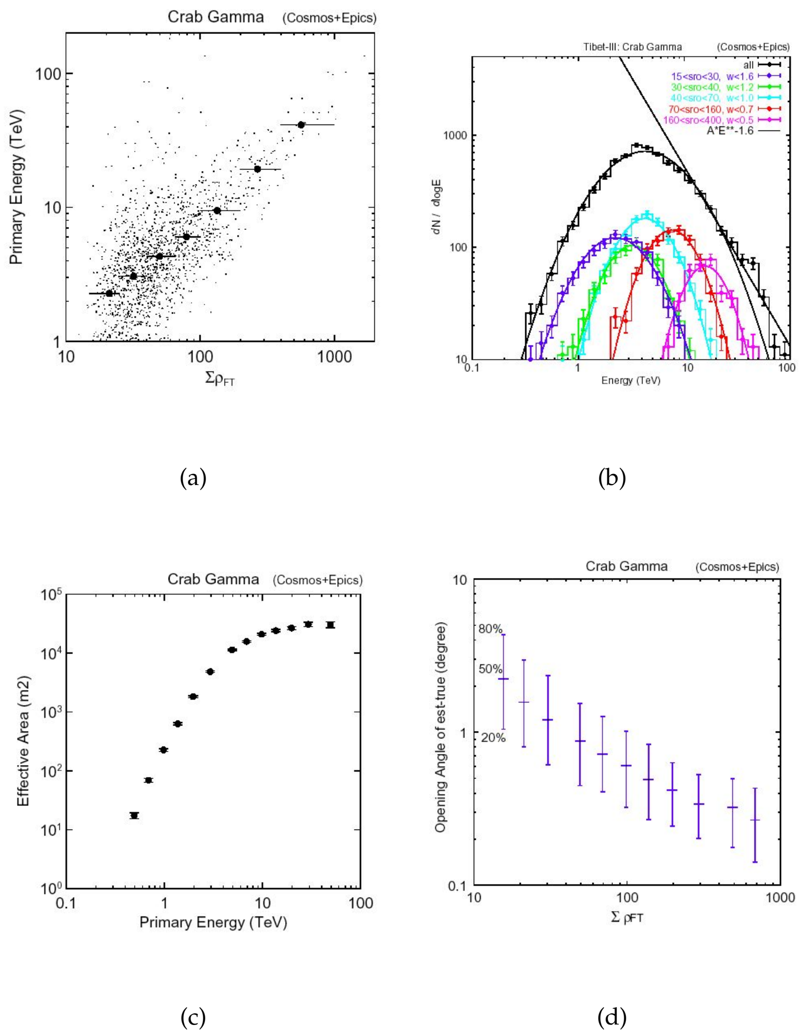

Figure 2.2: *The correlation between the primary γ-ray energy and the quantity $\sum \rho_{FT}$, defined in the text (a), the primary γ-ray energy distribution (b), the effective area (c) and the angular resolution (d)*

located in Tibet at 4300 m above sea level, consisted of two overlapping arrays: Tibet-II, constituted of 185 scintillation detectors with a surface of 0.5 m^2 each and spaced by 15 m, occupies an area of 36900 m^2 and HD (High Density) inside the Tibet-II array whose scintillation detectors are placed on a denser grid (indeed they are spaced by 7.5 m) to cover an area of 5175 m^2. In the late fall of 1999 the HD array was enlarged to cover 22000 m^2 (Tibet-III array). Each counter is supported by a 2 inch diameter PMT. Tibet-III array started to take data in November 1999 ending in May 2001. A signal from the Crab Nebula was observed.

Most of the detected events are initiated by primary cosmic rays rather than γ-rays. The correlation between the primary γ-ray energy and $\sum \rho_{FT}$, where ρ_{FT} is the particle density in each detector and the sum is extended over all fired detectors, the primary γ-ray energy distribution in each $\sum \rho_{FT}$ bin, the effective area and the angular resolution which reproduces the measurements of the shadow of the moon, have been all simulated in order to measure the flux of the Crab Nebula. These quantities are shown in Fig. 2.2a, b, c, d respectively. The differential γ-ray flux shown in Fig. 2.3, is also calculated using the events in excess for each bin, the simulated effective area, the correlation between $\sum \rho_{FT}$ and the primary γ-ray energy. The statistical significance of the detected signal is

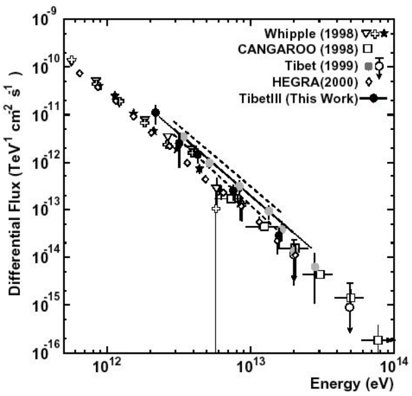

Figure 2.3: *γ-ray differential flux from the crab nebula as observed by the Tibet-III detector.*

4.8σ. It has been calculated using the formula $\frac{(N_{ON}-N_{OFF})}{\sqrt{N_{OFF}}}$, where N_{ON} and N_{OFF} are the numbers of on-source and off-source events.

CANGAROO

The CANGAROO experiment is located at Woomera in South Australia. Its detector consists of a 3.8 m IACT (Imaging Atmospheric Čerenkov Telescope), briefly discussed in Sec. 1.2.1 equipped in the focal plane with a high resolution camera made of 10 mm

$\times$ 10 mm square-shaped photomultiplier tubes. The number of photomultipliers was 220 in 1993 and was increased to 256 in 1995, reaching a total field of view of about 3°. The Crab Nebula was observed by means of the large zenith angle technique [43], at angles between 53° and 56°, during three periods: in 1992, from December 1993 to January 1994 and from December 1995 to January 1996. The imaging analysis of the data use some parameters which define the image of the air-shower formed on the camera of photomultipliers: "width", "length", "distance", α, the image orientation angle (see Fig. 1.15), and "conc", the concentration of the yield of the Čerenkov light in the image. The distribution of all the on-source events as a function of the parameter α is shown in

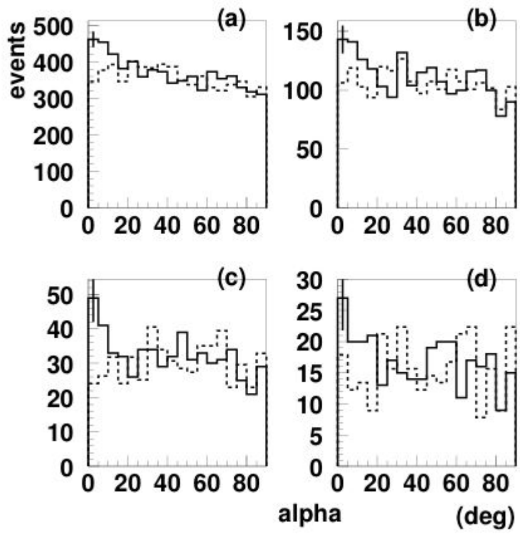

Figure 2.4: *The α distributions for all the on-source events (a) and for events with energies* $\geqslant$ 20 TeV *(b),* $\geqslant$ 37 TeV *(c) and* $\geqslant$ 47TeV *(d).*

Fig. 2.4a. The peak near the origin ($\alpha \leqslant 15°$) is thought to be produced by the γ-rays coming from the Crab Nebula. The background in this angular region is estimated from the flat distribution of the on-source events when $30° \leqslant \alpha \leqslant 90°$. Therefore, the statistical significance of this peak is calculated with:

$$\frac{N_{on} - \beta \cdot N_{back}}{\sqrt{N_{on} + \beta^2 \cdot N_{back}}} \tag{2.3}$$

where N_{on} is the number of the on-source events in the angular region $0° \leqslant \alpha \leqslant 15°$, N_{back} is the number events when $30° \leqslant \alpha \leqslant 90°$ and β is the ratio of the width of the two angular ranges (respectively 15° and 60°). The distribution of the on-source events

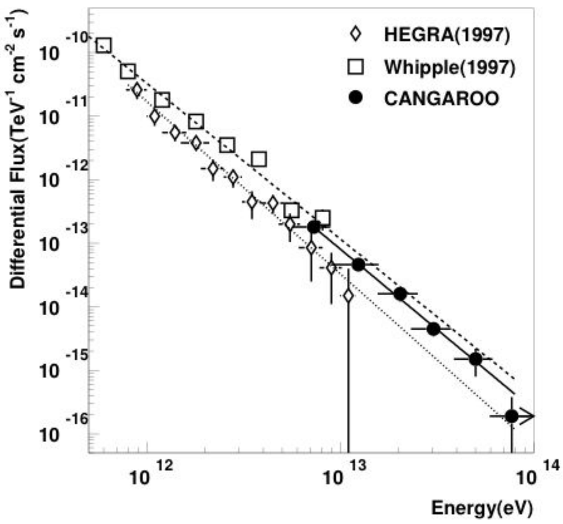

Figure 2.5: *The differential flux of the Crab nebula as measured by CANGAROO.*

as a function of α, the trigger efficiency, the collecting area and the threshold energy have been inferred for different values of the minimum and maximum number of detected Čerenkov photons, in order to obtain the energy spectrum. The "$alpha$ plots" for the events with energy $\geqslant 20$ TeV, $\geqslant 37$ TeV and $\geqslant 47$TeV are shown in Fig. 2.4b, Fig. 2.4c and Fig. 2.4d respectively. The differential flux J(E) as a function of the γ-ray energy is plotted in Fig. 2.5 and reported in Eq. 2.4.

$$J(E) = (2.01 \pm 0.36) \times 10^{-13} \left(\frac{E}{7\mathrm{TeV}}\right)^{-2.53\pm0.18} \quad \mathrm{TeV}^{-1}\mathrm{cm}^{-2}\mathrm{s}^{-1} \tag{2.4}$$

The total systematic error on the flux is 58%. There is no evidence for a cutoff up to 50 TeV.

Most of the experiments which observe the VHE sky are Atmospheric Čerenkov Telescopes. Notwithstanding these detectors can currently reach very high significances, the systematic uncertainties on the flux estimates are still large. It seems to be very difficult to obtain accurate measurements of the Crab nebula flux. However, all data sets are consistent within statistical and systematic errors. In order to understand the possible biases or errors in applying the Čerenkov technique for detections, estimates inferred using other detection methods could be very useful. The Tibet-ASγ experiment uses an alternative detection method to study the Crab nebula spectrum at energies between 3 TeV and ~ 20 TeV. Therefore its measurements partially overlap those of Čerenkov experiments. Tibet data show significantly higher (by a factor 2) γ-ray fluxes compared with the results obtained using IACTs in the energy range 3-18 TeV and is in favour of a gradual steepening of the spectral slope at high energies even if it may not be incompatible with the CANGAROO data.

The Argo experiment bases on an alternative detection technique with respect both Čerenkov telescopes and the Tibet-ASγ scintillation detector arrays. Therefore, the ARGO detector observation of the Crab nebula spectrum could reveal very interesting.

2.3 Theoretical models and open questions

Figure 2.6 shows the broad band nonthermal spectrum emitted by the Crab nebula: the general behaviour is due to two major mechanisms, namely the synchrotron radiation of relativistic electrons which are accelerated up to 10^{16} eV [44] and their inverse Compton (IC) scattering in the ambient photon fields. The first process is responsible for the emission in the energy range from radio to relatively low γ-rays (first bump in Fig. 2.6, $\nu < 10^{23}$ Hz), while the second one is considered to be the most probable for the rest of the spectrum emission at higher energies (second bump in Fig. 2.6). The IC scattering occurs mainly on three photon fields: the synchrotron radiation of the nebula; the far-infrared (FIR) radiation, probably associated with the dust; the 2.7 K microwave background radiation.

The nonthermal emission from the Crab nebula can be calculated knowing the spatial distribution of the magnetic field and the electron energy distribution. MagnetoHydroDynamic (MHD) models of the Crab nebula, even in the case of simplified hypotheses (without considering the asymmetric structure of the wind and its interactions with the optical filaments), describe the nebular environment downstream the wind shock quite

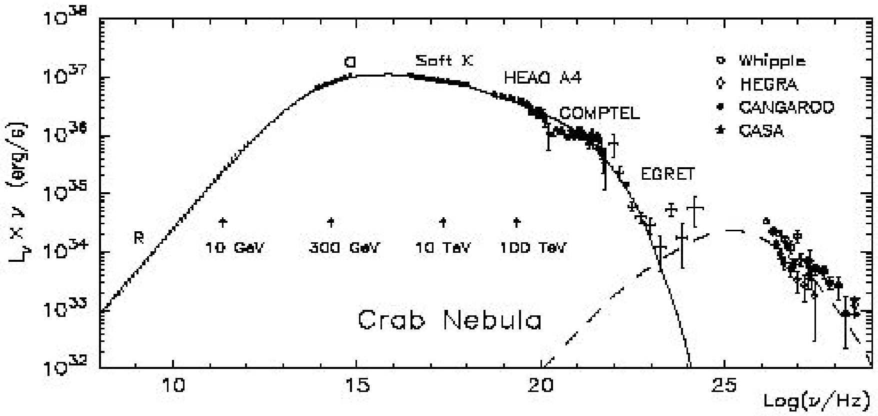

Figure 2.6: *The measurements of the nonthermal radiation emitted from the Crab nebula. The solid and dashed curves correspond to the synchrotron and inverse Compton components of radiation, respectively, calculated in the framework of the spherically symmetric MHD wind model [45].*

well. A self-consistent MHD model of the magnetic field and the flow of the relativistic plasma has been built in [45]. The main parameter, which defines the behaviour of the magnetic field and the flow of the relativistic plasma in the nebula is σ, the ratio between the electromagnetic and the particle energy flux at the wind shock:

$$\sigma = \frac{B_s}{4\pi n u \gamma m c^2} \tag{2.5}$$

where B_s is the magnetic field intensity, n the particle density, u the radial four-speed of the relativistic electron flow at the shock. σ gives the spatial distribution of the magnetic field. If $\sigma \ll 1$ the value of the resulting magnetic field increases downstream of the shock as the observations suggest. The best fit for the MHD solution is obtained for $\sigma = 3 \cdot 10^{-3}$.

The synchrotron radiation from the nebula in the framework of this MHD model has been soon calculated by the same authors [46]. This calculation could account for the observed intensity and spatial distribution of the synchrotron radiation from the infrared to the highest γ energy, but not for the radio emission. Therefore, in order to account also for the radio emission, an additional low energy component made by the so-called *radio* electrons, whose characteristics are not completely understood, has been introduced. It could be a component accumulated most probably during the whole history of the Crab [45].

Two different methods have being used to derive the spectrum of the relativistic electrons in the Crab nebula. In the first one the observed synchrotron emission and brightness distribution are used to infer the electron spectrum, assuming the magnetic field distribution of the MHD model [22]; in the second one the electron spectrum is calculated in the framework of the MHD model, using its propagation theory of the electrons in the nebula together with an injection distribution which would account for the observed synchrotron radiation spectrum and brightness distribution [44]. In Fig. 2.6 the

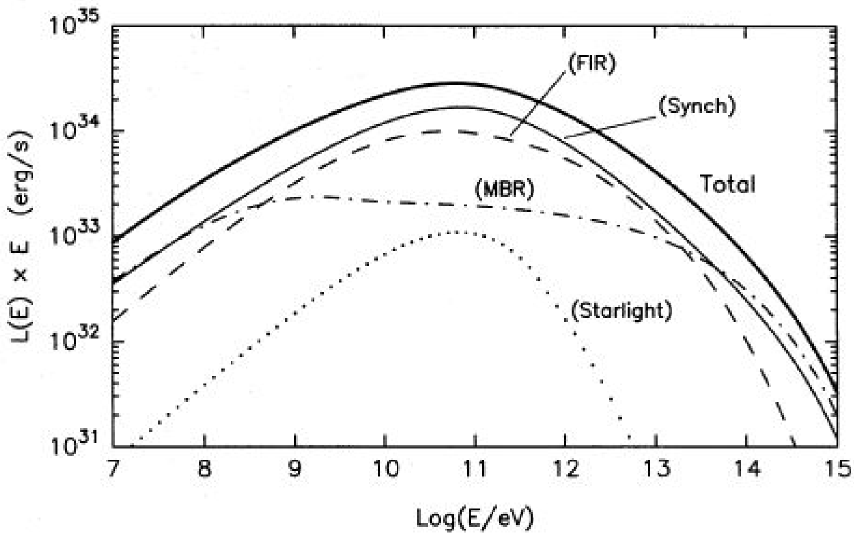

Figure 2.7: *The IC γ-ray component of the Crab nebula spectrum is the sum of different contributions due to several photon targets: the synchrotron (solid curve), the dust FIR(dashed curve), the MBR (Microwave Background Radiation) (dot-dashed curve), the galactic starlight (dotted curve) photon fields. The heavy solid curve is the total spectrum of IC γ-rays.*

experimental data as of 1998 are fitted with a solid and a dashed curve which are the synchrotron and inverse Compton components respectively, calculated with the second procedure described above, in the framework of the spherically symmetric MHD wind model [44]. Figure 2.7 shows the several contributions to the total IC scattering component due to the different photon fields present in the nebula. The contributions owing to IC scattering on the synchrotron and on FIR photons are comparable while the contribution of the microwave background radiation becomes significant already at $\sim$ 1 TeV and dominates at energies E$\geqslant$30 TeV, making the overall IC spectrum significantly harder. This gives fluxes of gamma rays at E$\geqslant$30 TeV close to the measured upper limits (see

Fig 2.8).

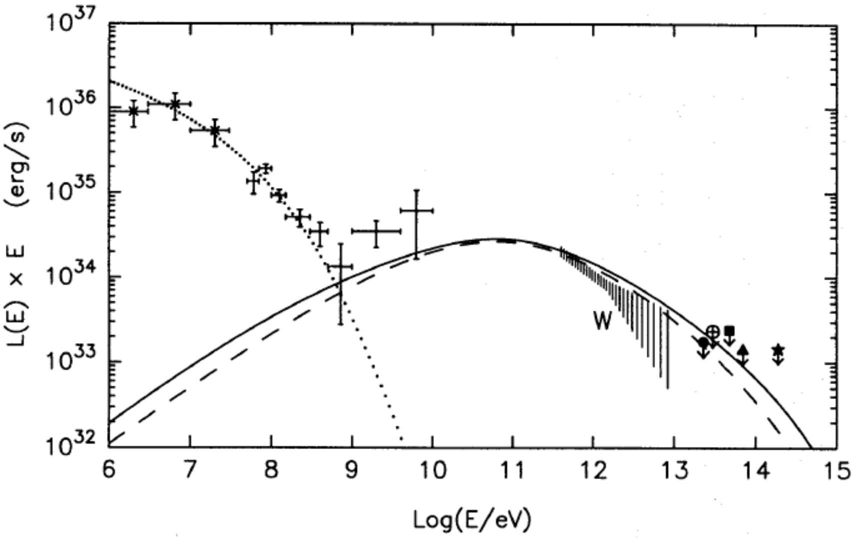

Figure 2.8: *The dashed line is the spectrum from the Crab nebula due to the IC γ-ray component upscattered off the synchrotron and dust FIR photons. The solid line consider also the contribution due to the 2.7 K photon target. The upper limits obtained at energies above 30 TeV from the Tibet, HEGRA, Cygnus and CASAMIA (from the left to the right side) experiments are shown.*

The shape of the total IC γ-ray spectrum is rather stable with respect to the basic parameters which describe the nebular environment in the framework of the MHD model [44], while its absolute flux is sensitive to the average magnetic field in the nebula. Moreover, because the target photon fields are well known, the flux of IC γ-rays can be calculated with good accuracy. Therefore the average magnetic field in a specific region of the nebula can be derived from the comparison of the predicted IC spectrum emission and the measured one in the corresponding energy range. Indeed for a given synchrotron emission, the number of electrons which determines the observed IC radiation, strongly depends on the nebular magnetic field.

The simplified synchrotron-Compton model (which requires only these two mechanisms at work) does not fit perfectly the experimental data. There are some features in the spectrum at 1-10 MeV, 1-10 GeV, and $\geqslant$ 10 TeV energies which require a more involved description of what happens. In order to explain these characteristics, it must be considered that the Crab is an object more complicated than assumed in the model, as some images (see Fig. 1.8) of the nebula from the Hubble Space Telescope and ROSAT show: its inner structure presents features like wisps, jets, knots, etc. [47]. It is believed that taking into account these complex aspects would not affect the overall nonthermal spectrum but could introduce some spectral deviations in the X-ray and γ-ray range. At these energies the overall spectrum could be influenced both by the bremsstrahlung of relativistic electrons and by π^0 decays (produced by protons interacting with matter) which could occur in regions with higher density (nearby filaments where relativistic particles could be confined). The problematic spectral features are reported in the following.

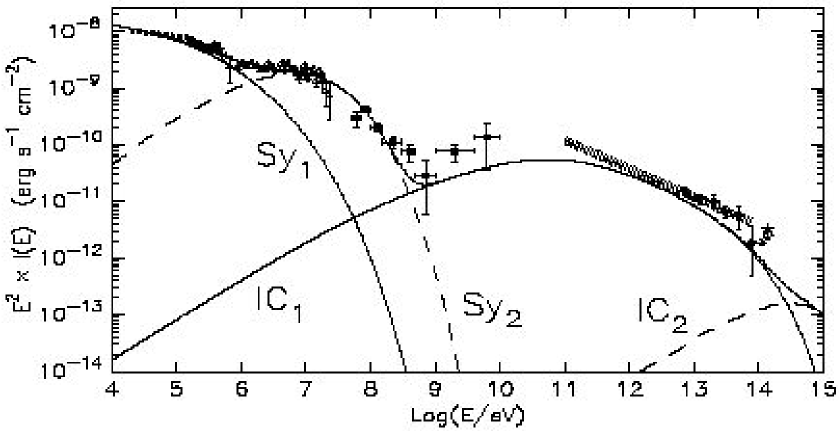

Figure 2.9: *Synchrotron and IC radiation components produced by the first (solid) and second (dashed) populations of electrons. The heavy solid line shows the total calculated flux. The hatched region correspond to* $I(E) = (2.5 \pm 0.4)(E/1\mathrm{TeV})^{-2.5}$ $\mathrm{cm}^{-2}\mathrm{s}^{-1}\mathrm{TeV}^{-1}$ *which generally describes the flux level from 300* GeV to 70 TeV reported by different groups.

- The COMPTEL experiment [48] detected an unexpected flattening of the spectrum at energies 1-10 MeV. Indeed it was well known that above 100 keV the emission spectrum was going to steepen [49] [50]. Either peculiarities in the spectrum of the injected electrons or the existence of another radiation component in terms of nuclear γ-line emission [48], cannot explain this characteristic of the nonthermal spectrum while the introduction of a second population of high energy electrons can interpret it [51]. Figure 2.9 presents a possible fit to the observed fluxes up to ~ 1 GeV by a two-component synchrotron emission [52]. The possible sites of acceleration of the second electron population could be the peculiar compact regions such as wisps, knots, etc.

- The predicted flux in the inverse Compton component at energies 1-10 GeV is lower than the measured one, and perhaps also at energies $\geqslant$10 TeV. This feature cannot be easily explained by another IC component. Different mechanisms are thought to be introduced. The nebula is characterised by a mean gas density $\bar{n}\approx 5\ \mathrm{cm}^{-3}$. This means that the flux of the γ-rays produced by bremsstrahlung cannot exceed 15% of the flux from IC. However in the filaments of the nebula the gas density reaches the value $\sim$10 ^{3} cm^{-3}. An effective gas density can be defined, and $n_{eff} \gg \bar{n}$ **??**. The presence of this process would affect also the energy spectrum at higher energies. If $n_{eff} \gg \bar{n}$, also the production of γ-rays by means of π^0 decays could show up. Figure 2.10 shows the contributions of different γ-rays production mechanisms to the total nonthermal radiation of the Crab Nebula. The Synchrotron and IC components are the same as in Fig. 2.9. The contributions from bremsstrahlung and π^0-decay processes are added for $n_{eff} = 50\ \mathrm{cm}^{-3}$. Considering only the IC mechanism, the spectrum is hard at $E \simeq$100GeV ($\alpha_\gamma \simeq$2.0) and steeper at higher energies ($\alpha_\gamma \simeq$2.7 at $E \simeq$10TeV and $\alpha_\gamma \simeq$3 at $E \simeq$30TeV). The superposition of IC and bremsstrahlung components results almost in a single power-law spectrum with an index $\alpha_\gamma \simeq$2.5 - 2.7 in the energy range from 100 GeV to 10 TeV. Finally, adding also the contribution due to the π^0-decay mechanism, a power-law spectrum with $\alpha_\gamma \simeq 2.5$ is obtained over the whole energy range from 100 GeV to 100 TeV [52].

2.4 Summary

The observation of the nonthermal radiation emitted from the Crab nebula is of extreme importance. The data collected up to now have provided deep insight into the mechanism in action inside the nebula, even if many efforts are still required. The synchrotron emission and the IC scattering mechanisms are commonly thought to be the most probable processes at the origin of the nonthermal γ-ray emission. Some of the

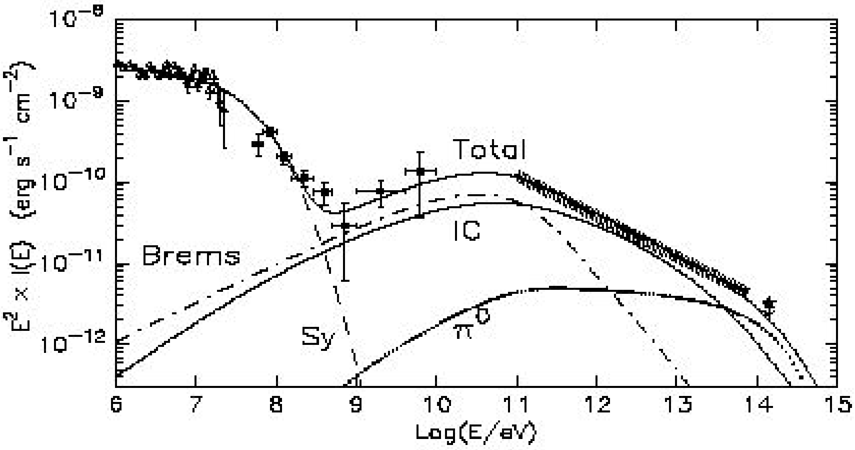

Figure 2.10: *The contributions of the several mechanisms of γ-ray production. The synchrotron and IC contributions are the same as in Fig. 2.9. The bremsstrahlung and π^0-decay γ-ray fluxes are calculated for n_{eff} = 50* cm^{-3}.

improvements made in the knowledge of the Crab system owing to the ground-based measurements are reported below:

- Observations of TeV γ-rays by the Whipple, HEGRA, Themistocle and CANGAROO experiments confirm that the seed photons for the IC process are Cosmic Microwave Background (CMB) and infrared (IR) photons emitted from dust in the nebula [44] besides the synchrotron ones.

- An alternative γ-ray production process with respect to the one described in Sec. 1.1.4, was also supposed nearby the light cylinder within the pulsar magnetosphere. In this region the magnetic field is so high that γ-rays with energy above 10 TeV are subject to the pair creation process in such a way that a multi-TeV signal from the Crab is not expected [53]. Therefore, the CANGAROO results ruled out this hypothesis.

- All models based only on electrons as particles from which the TeV radiation originates, have difficulty in explaining a spectrum which extends beyond 50 TeV. Protons from the Crab pulsar's wind could be accelerated at the nebula shock front and could thus generate π^0s which decay and produce γ radiation. However CANGAROO measurements do not exclude the action of the IC process alone, within the allowed variability of the magnetic field although they prefer the solution which includes together with the IC scattering, the bremsstrahlung and π^0 decays as γ-ray production mechanisms.

At present, the flux measurements made in the tens of GeV and VHE ranges cannot be simultaneously understood in terms of IC radiation. However, because of the current uncertainties in the measured γ-ray fluxes of both GeV and TeV energies, the possibility that γ-rays with energy from 1 GeV to 10 TeV are produced by means of the IC mechanism alone cannot be unambiguously ruled out. In the energy region from 1 TeV to 10 TeV of the Crab nebula spectrum, as can be noticed from Fig.2.10, the IC scattering is the dominating process with respect to the mechanisms which can show up as a consequence of the relativistic particle interaction with the ambient gas. The search for the proof of the action of the bremsstrahlung mechanism must be aimed to the energy range below 1TeV, where this process could significantly affect the emission spectrum. Some low-energy threshold Čerenkov telescopes like STACEE and CELESTE will provide fluxes measurement down to 30 GeV. On the other hand the satellite-experiment GLAST, could confirm the EGRET measurements, thus requiring or not the presence of this process. Moreover the detection of the energy spectrum up to 100 TeV seems to be very interesting. The detection of the nebula up to 50 TeV energies by the CANGAROO experiment is of great importance, but it would be determinant to have independent and accurate measurements in this energy region, where the first evidence of hadronic acceleration could show up.

The Argo experiment could give its contribution to this subject within the γ-ray astronomy. It was mainly designed to observe γ-ray sources at energy from about 100 GeV to about 10 TeV, with the intent to extend the energy range of operation to tens of TeV. Therefore, the Argo collaboration is planning an enlargement of the detector active surface and the introduction of an opportune muon tracker in order to obtain accurate measurements in such a high energy range. The extension of the apparatus will allow the collection of a statistically significant number of photon-induced air-showers and on the other hand the muon identification system will allow an effective background rejection. The upgrade of the apparatus is aimed not only to the detection of the Crab nebula spectrum at the highest energy ever observed but also to the detection of the rest of the point-sources which have emission in that energy range. Besides, another application could be the investigation of the cosmic ray composition which is under study.

This thesis is a study of the background rejection by means of the muon identification technique. The estimate of its effectiveness has been calculated (Chapter 5). The results thus obtained have been used to evaluate the sensitivity to the Crab nebula with the upgraded apparatus. Moreover a study of the Crab spectrum at its highest energy with some of the possible scenarios is presented.

Chapter 3

The Argo experiment

The aim of the ARGO-YBJ experiment is the study of cosmic rays, mainly γ-radiation with an energy threshold of hundreds GeV up to few tens TeV. An EAS-PAD experiment can achieve such a low energy threshold by detecting small size air-showers. This requires the experiment to operate at very high altitude in order to better approach the level where low-energy air showers reach their maximum development, and with a full coverage detector in order to maximize the number of detected particles for a small size shower. Therefore, the YangBaJing (YBJ) Cosmic Ray Laboratory (Tibet, China, 30.113 N, 90.533 E.), 4300 m a.s.l, has been chosen as the experiment site. This location will allow the monitoring of the Northern hemisphere in the declination band $-10^\circ < \delta < 70^\circ$, with wide-aperture and high duty cycle.

Moreover, γ-ray source observation demands a large detection area because of low γ-ray fluxes and an accurate reconstruction of the shower arrival direction in order to suppress the huge isotropic background constituted by hadronic cosmic rays. The Resistive Plate Chamber (RPC) detectors offer noticeable advantages owing to low-cost, thus leaving to cover a large active area, and excellent time resolution which would allow to obtain angular resolution lower than the degree.

The ARGO-YBJ apparatus consists of a full coverage array of dimension $\sim 74 \times 78\ \mathrm{m}^2$ realised with a single RPC layer surrounded by a partially instrumented ring, thus covering up to $\sim 100 \times 100\ \mathrm{m}^2$. This outer ring allows a better reconstruction of those events whose core is outside the full coverage carpet. A lead converter 0.5 cm thick will cover uniformly the RPCs layer in order to increase the number of charged particles by conversion of secondary photons and to reduce the time spread of the shower front.

The low energy threshold achievable by ARGO would allow to bridge the GeV energy region with the one of TeV and to produce data on a wide range of fundamental issues in cosmic ray physics and γ-ray astronomy [54]. Other physics items are [54]:

- Diffuse γ-rays from the Galactic plane, molecular clouds and SNR at energy of several hundreds GeV.
- Gamma Ray Burst physics, by allowing the extension of the satellite measurements over the full GeV/TeV energy range.
- $\overline{p}/\mathrm{p}$ at energies 300 GeV $\div \sim$ TeV.
- The primary proton spectrum in the 10÷200 TeV region, with sensitivity sufficient to detect a possible change in slope of the energy spectrum
- Sun and Heliosphere physics, including cosmic ray modulation at 10 GeV threshold energy, the continuous monitoring of the large scale structure of the interplanetary magnetic field and high energy gamma and neutron flares from the Sun.

3.1 Detector layout, Trigger and Data Acquisition System (DAQ)

In this section a schematic description of the apparatus will be given. The details can be found elsewhere [54], [55], [56], [57] and [58]. The basic elements of the Argo detector are RPCs of dimension 280×125 cm^2. Figure 3.1 shows the apparatus to be arranged in modules of 12 RPCs, called "clusters" (764×572 cm^2). The cluster is a logical subdivision of the apparatus: it is the basic unit for DAQ and trigger systems. The central detector consists of 130 clusters and the ring of 24 clusters.

The signals from each RPC are picked up by means of 80 read-out strips. The "Fast-OR" of 8 strips defines a logic unit called "pad" (56×62cm^2). The pad signal is used for time measurements and trigger purposes.

The trigger and the DAQ systems are built in a two level architecture. The signals coming from the cluster are managed by the Local Stations which in particular provide

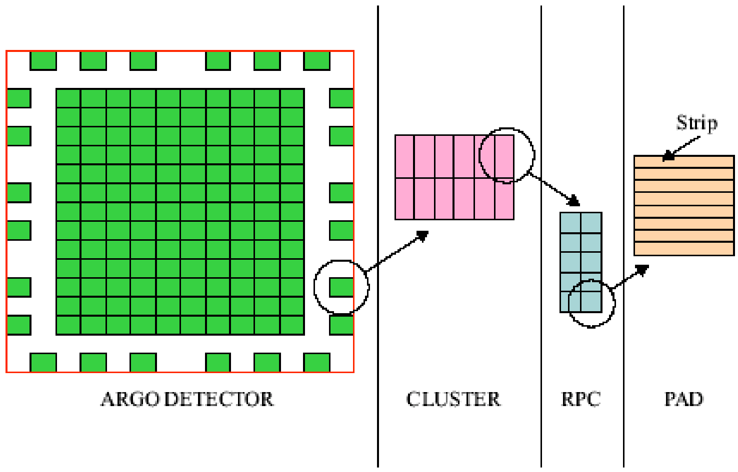

Figure 3.1: *The Argo apparatus.*

the pad multiplicity information. At any trigger occurrence the times of all the pads are read out by means of multihit TDCs operating in COMMON STOP mode. Therefore the pads are the basic elements which define the spacetime pattern of the shower; they give indeed the time and the position of each detected hit. Then, the space and time information for each Local Station is collected and elaborated in the Central Station for event building and storage.

Two main kinds of trigger have been designed for the ARGO detector: “scaler mode” trigger and “shower mode” trigger. The “scaler mode” trigger is based on the measurements of the single rate of pads with the aim of monitoring the apparatus and detecting unexpected increases of cosmic rays mainly related to solar flares or Gamma Ray Burst. The “shower mode” trigger is based on the requirements that a minimum number of pads are fired in the central carpet with the proper space-time pattern.

3.1.1 Resistive Plate Chambers

RPCs are gaseous detectors which detect the passage of charged particles because of their ionisation losses in the gas. The basic detector of the experiment is the ARGO-RPC that consists of:

- the *gas volume*, i.e. the active part of the detector;
- the strip sheet and its front-end electronics;
- the BIG PAD for the analog detection of the ionising particle signals.

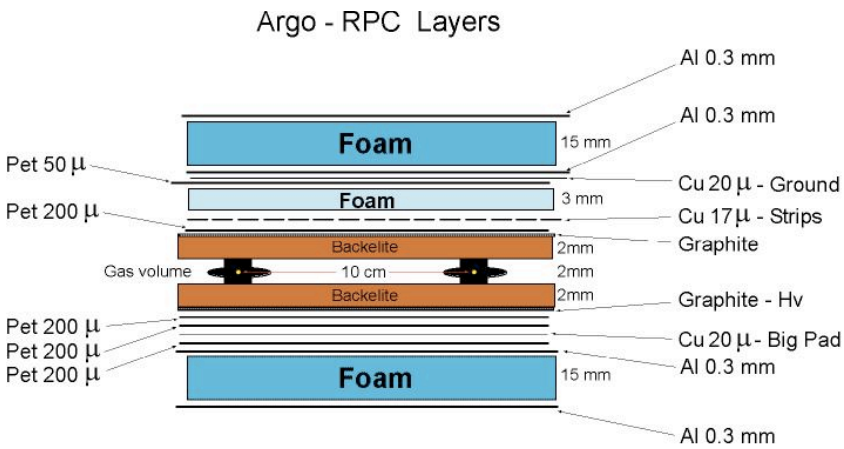

Figure 3.2: *Composition of the basic element of the Argo detector.*

The detector is built with bakelite electrode plates of volume resistivity in the range $0.5 \div 1 \cdot 10^{12}\ \Omega\ \mathrm{cm}$ [59], which form a 2 mm gas gap. Inside the gas volume, insulating disks, with a surface of about $1\ \mathrm{cm}^2$ and having a distance of 10 cm one from another, are inserted in order to guarantee the detector rigidity and uniform spacing between the two electrodes. On top of the detector, the copper strips, 6.7 cm wide and 62 cm long, collect the RPC signals. A copper foil, separated from the strips with a 3 mm thick polystyrene foam sheet, is used as a ground strip reference. The detector cross-section is given in Fig. 3.2. At the edge of the detector the strips are connected to the front end electronics and terminated with $50\ \Omega$ resistors. The front end circuit contains 16 discriminators, with about 50 mV voltage threshold, and provides the FAST-OR signal of the 8 strips which constitute the pad. The opposite end of the strips, at the center of the detector, is not terminated. The RPC bottom electrode plate is connected to the high voltage. The BIG PAD signal is collected by a copper foil which is insulated from the RPC with a sheet of plastic material (PET [1]). A rigid polystyrene foam plate is used to avoid the direct contact

[1]Poly-ethylene-tereftalate.

of the RPCs with the concrete floor.

The RPCs operating in streamer mode with gas mixtures of argon (15%), isobutane (10%) and tetrauoroethane $C_2H_2F_4$ (75%), at a voltage of 7500 V, have a single counting rate below 500 Hz/pad, provide an efficiency greater than 96% and a time resolution better than 1 ns [60]. These results confirm the ones previously obtained during the test described in [59].

3.1.2 Experiment status and detector performance

At present 36 clusters of the central detector carpet (corresponding to a total instrumented area of $\sim$ 1600 m^2) have been installed and partially put in operation for debugging and certification. Each cluster has been individually run by using "shower mode" triggers of low ($\geqslant 3$) and medium ($\geqslant 16$) pad multiplicity, in order to test the performance of the individual components, the uniformity of their response and the time alignment of all electronics channels. The overall functioning of the detector components has been tested by operating with a "shower mode" trigger $\geqslant 16$. Figure 3.3 shows the rate of the

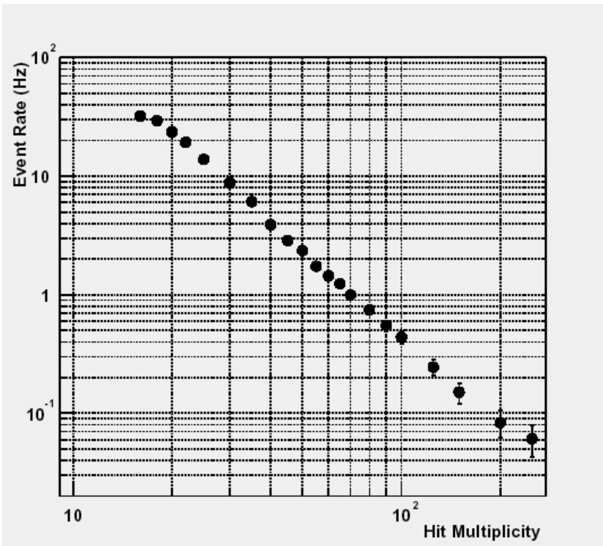

Figure 3.3: *Rate of events as a function of the hit multiplicity*

events as a function of the hit multiplicity: the linear shape with slope $\simeq 2.5$ on a double logarithmic plot proves the physics consistency of detected showers. The trigger rate is in agreement with the expected one. The experiment schedule foresees the completion of the carpet within 2005.

3.2 Detection of point-like γ-ray sources

As already explained, the study of γ-ray astronomy at the energy range from several hundreds GeV to about 10 TeV, is the main aim of the ARGO experiment. In Chapters 1 and 2, some interesting items which could be investigated have been discussed. The detection and study of γ-ray sources are aimed not only at the understanding of their structure but also of the cosmic ray phenomenon (see Sec. 1.1.1).

In order to evaluate the capability of the Argo experiment in detecting a certain source, its sensitivity to this source must be estimated. The sensitivity is defined as:

$$S = \frac{N_\gamma}{\sqrt{N_{\rm B}}} = \frac{T \int_{T(\delta)} {\rm d}t \int {\rm d}E \ \Phi_\gamma(E) \cdot A_\gamma(E, \theta(t)) \cdot \cos\theta(t) \cdot \epsilon(\Delta\Omega) \cdot Q(E)}{\sqrt{T \cdot \int_{T(\delta)} {\rm d}t \int {\rm d}E \ \Phi_{\rm B}(E) \cdot A_{\rm B}(E, \theta) \cdot \cos\theta(t) \cdot \Delta\Omega}} \tag{3.1}$$

where N_γ and $N_{\rm B}$ are the number of detected air showers generated by γ-ray and ordinary cosmic ray respectively, which are observed within the solid angle of opening Ψ', $\Delta\Omega = (1 - \cos\Psi')$: Ψ' is chosen in such a way to optimise the detection of signal against background, thus usually it is equal to Ψ_{70} defined in the next section. $\epsilon(\Delta\Omega)$ is the percentage of photons coming from the source observed within this solid angle, $\Phi_\gamma(E)$ ($\Phi_{\rm B}(E)$) is the γ-ray source (cosmic ray background) differential flux, T the effective time of data taking in days, T(δ) is the observation time of the source during a day depending on its declination δ, Q is a quantity which accounts for the discrimination of signal events against background ones and θ is the zenith angle. $A_\gamma(E,\theta)$ ($A_{\rm B}(E,\theta)$) is the photon (hadron) effective area:

$$A_{\gamma,B} = \frac{N_{gen}}{N_{rec}} \cdot A_{gen} \tag{3.2}$$

where N_{gen} are the events generated inside a large area A_{gen} and N_{rec} are those events which survive the trigger and reconstruction conditions. The factor $\cos(\theta)$ in Eq. 3.1 which multiplies the effective area takes into account its reduction when seen from the zenith angle θ.

The quantities which define the sensitivity are a function of the energy, therefore the sensitivity depends on the spectrum of the γ-ray source considered. The great relevance of the angular resolution for a sensitivity estimate has already been discussed in Sec. 1.2, where a schematic expression has been adopted for sensitivity. In the next sections the ARGO experiment sensitivity, without background discrimination, will be showed for the Crab nebula and blazars. The last section deals with the Argo experiment capacity in separating photon-initiated air-showers from hadron-initiated ones.

3.2.1 Angular resolution

An accurate reconstruction of the shower direction is the crucial point to identify γ-ray sources. The arrival direction of air-showers can be obtained from the space-time distribution of the hit pads by applying several reconstruction algorithms [61] whose performance can be estimated by means of the Ψ_{70} parameter. This is defined as the value of the opening angle Ψ between the true and the reconstructed direction within which 71.5% of the events are contained. If the Ψ distribution is gaussian, such a value optimises the ratio between the signal and the background when detecting a poin-like source.

For a given reconstruction algorithm, the accuracy of the direction reconstruction depends on the number of fired pads: thus, one algorithm can be more efficient in a certain pad range and less in another one [61].

Figure 3.4 shows the opening angle of the circular window which optimises the ratio between the signal and the background as a function of the number of fired pad, N_{pad}, for the simulation of the Crab nebula source. For $N_{\mathrm{pad}} \geqslant 150$ the distribution of Ψ is gaussian and thus Ψ' in Eq. 3.1 is the Ψ_{70} parameter. For $N_{\mathrm{pad}} \leqslant 150$ the Ψ distribution is not perfectly gaussian and the opening angle Ψ' has been separately evaluated for each class. Moreover in the range $30 \leqslant N_{\mathrm{pad}} < 50$ the shower front has been described by the planar approximation, while in the range $N_{\mathrm{pad}} \geqslant 50$ by the conical one. The Argo experiment achieves a rather good angular resolution, better of the degree. For high pad multiplicity ($N_{\mathrm{pad}} \geqslant 400$) it reaches 0.29°.

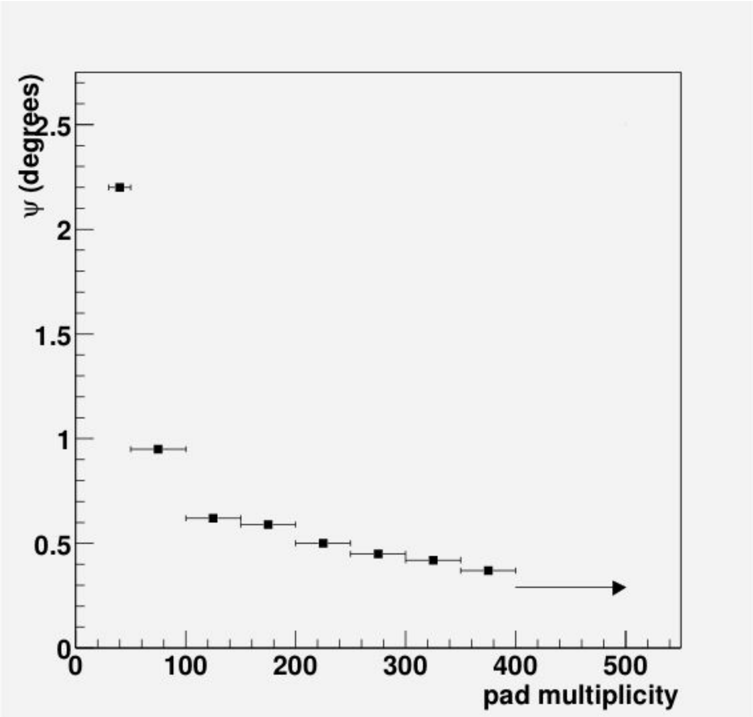

Figure 3.4: *Opening angle of the circular window around the Crab nebula position in the sky*

3.2.2 Expected sensitivity to the Crab nebula

A γ-ray flux has been simulated according to the Crab nebula spectrum measured by the Whipple collaboration [62]:

$$\frac{\mathrm{d}N}{\mathrm{d}E} = 3.2 \cdot 10^{-7} E^{-2.49} \quad \gamma\, \mathrm{m}^{-2}\mathrm{s}^{-1}\mathrm{TeV}^{-1} \tag{3.3}$$

The γ-rays have been simulated at different zenith angles following the daily path of the source for zenith angles $\theta \leqslant 30°$. Background has been simulated considering the proton and Helium fluxes [63] according to the spectra:

$$\frac{\mathrm{d}N}{\mathrm{d}E} = 8.98 \cdot 10^{-2} E^{-2.74} \quad \mathrm{p}\, \mathrm{m}^{-2}\mathrm{s}^{-1}\mathrm{sr}^{-1}\mathrm{TeV}^{-1} \tag{3.4}$$

$$\frac{\mathrm{d}N}{\mathrm{d}E} = 7.01 \cdot 10^{-2} E^{-2.64} \quad \mathrm{Helium\ \ nuclei}\, \mathrm{m}^{-2}\mathrm{s}^{-1}\mathrm{sr}^{-1}\mathrm{TeV}^{-1} \tag{3.5}$$

The simulation of the development of photon- and hadron-initiated air-showers has been performed by means of the CORSIKA program and the detector response by a GEANT-3 based code called ARGO-G. Both are described in Chapter 4. For the events with a

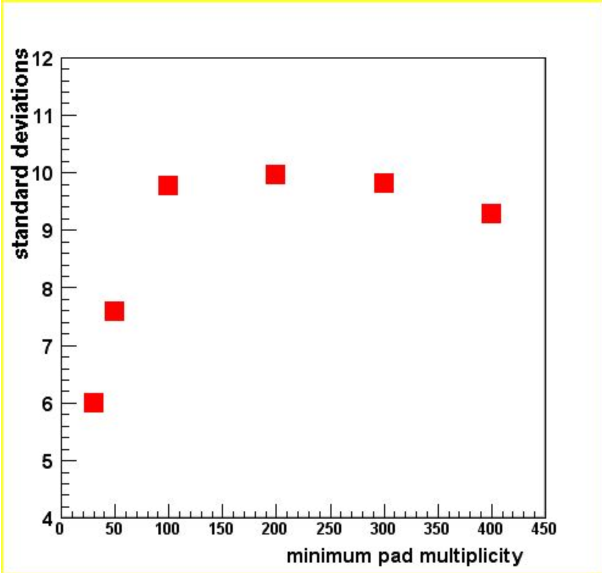

Figure 3.5: *Sensitivity to the Crab nebula versus the minimum pad multiplicity [64].*

number of fired pad $N_{\rm pad} \geqslant 50$ the core position is reconstructed and the arrival direction is evaluated by a space-time conical fit of the shower front. Only the events whose reconstructed core falls inside the "fiducial area" $A_{\rm f}$ 80×80 have been considered because the angular resolution reconstruction is less accurate as the distance of the core from the center of the apparatus increases. Any kind of selection has been applied on the events with $30 \leqslant N_{\rm pad} < 50$ whose arrival direction has been reconstructed with a planar fit. As already showed, the angular resolution strongly depends on the number of fired pads $N_{\rm pad}$ (see Sec. 3.2.1), thus the events have been divided into "classes" defined by ranges of multiplicity in which different values of the angular resolution has been adopted (Fig. 3.4). Figure 3.5 shows the significance of the expected signal from the Crab nebula after one year of observation as a function of the minimum value of the unlimited pad multiplicity range considered. ARGO-YBJ can observe in one year a source with a Crab-like energy spectrum of intensity equal to 0.7 (0.4) Crab units, at energy about $E > 0.5$ (1.0) TeV, with a significance of 4 standard deviations.

3.2.3 Expected sensitivity to blazers

Blazars are radio-loud AGNs with their jet at relatively small angles ($\leqslant 20 - 30°$) with respect to the line of sight (see Sec. 1.1.2). Figure 3.6 shows the spectral energy distri-

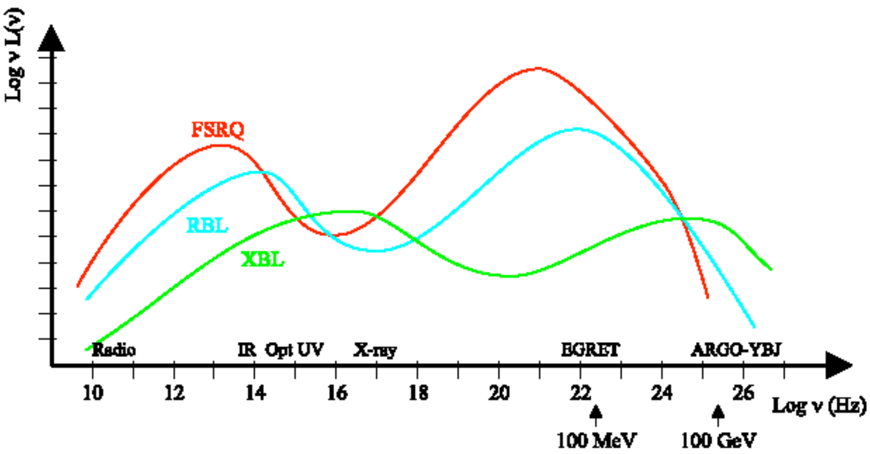

Figure 3.6: *Schematic average SED of different blazar subclasses from radio through TeV γ-rays*

bution of different blazar subclasses: FSRQ (Flat Spectrum Radio Quasar), RBL (Radio selected BL Lac) and XBL (X-ray selected BL Lac) from radio through γ-rays. The EGRET and ARGO operation energy ranges are also indicated. The ARGO experiment seems to be suitable for detection of XLBs which are the blazars with the spectrum shifted to the highest energies. In fact, the four confirmed extragalactic VHE sources so far, namely Mrk 421, Mrk 501, H1426+428, and 1ES 1959+650 are all classified as XBL.

Blazars are characterised by rapid flux variability, down to hour time scale. Therefore detectors with low exposition time are required. The Argo observation time has been estimated starting from the already estimated sensitivity to poin-like source (see previous Section) for the 1997 Markarian 501 outburst. Figure 3.7 shows this outburst as seen by HEGRA, normalised to Crab flux (top), and corresponding expected observation times $t_{\rm obs}$ to achieve 4σ detection with ARGO (bottom). The dashed lines in the Figure refer to the Crab nebula. The observation time for a Crab-like flux is ~ 70 days, while in the favourable case of source flaring up to 7-8 Crab fluxes, ~ 1 day of exposure is sufficient for a 4σ detection.

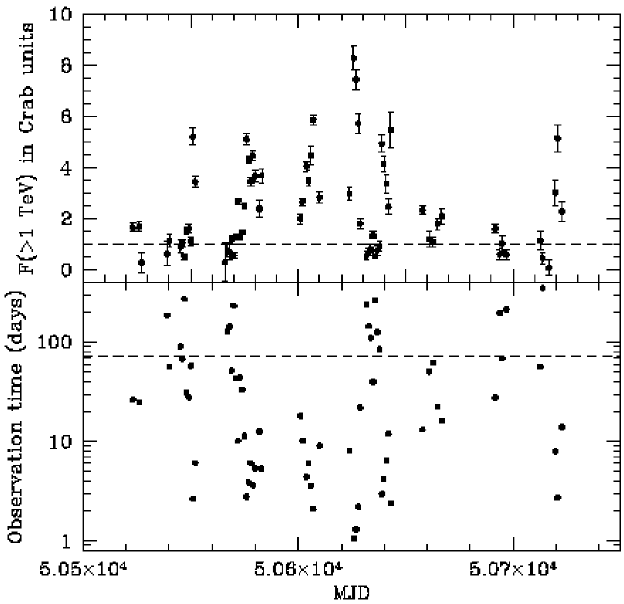

Figure 3.7: *Daily integral fluxes for the 1997 Mrk 501 outburst as seen by HEGRA, normalised to Crab flux (top) and corresponding expected observation times $t_{\rm obs}$ to achieve a 4σ detection with Argo (bottom). The dashed lines refer to the Crab.*

The cosmological horizon for blazar observation with ARGO has been found to be $z \sim 0.1$ [65]. Fixed the cosmological horizon, considering the ARGO site latitude, 14 blazars are candidates for ARGO observation.

3.2.4 γ-hadron separation

Background rejection is one of the main concerns for γ-ray source detection. Discrimination between electromagnetic and hadronic showers together with a good angular resolution, allows the reduction of the huge background constituted by hadronic cosmic rays. This difficult task can be approached with software algorithms or experimental methods. The Argo collaboration is being explored both techniques.

The Argo full coverage detector with its high space granularity can give detailed images of the shower front which can be exploited to highlight the differences between the two kinds of shower [66] [23]. These images have been analised at different length scales and their multifractal nature has been studied in [67], in order to identify characterising functions used as inputs for an Artificial Neural Network (ANN), which performs the γ-hadron discrimination. The output of the Neural Network is a parameter which assumes the value equal to 1 for γ-initiated showers and 0 for the hadron-initiated ones.

A simulated sample of events corresponding to photon- and hadron-initiated air-showers belonging to the energy range $30\ \mathrm{GeV} \div 100\ \mathrm{TeV}$ with azimuth between $0°$ and $15°$ and core at the detector center have been generated. The primary energy spectrum has been generated according to power law with spectral index γ=2.5 for photons and γ=2.7 for hadrons. The detector response has been fully simulated. Events have been classified according to their hit multiplicity. However the corresponding average primary energy has been also estimated.

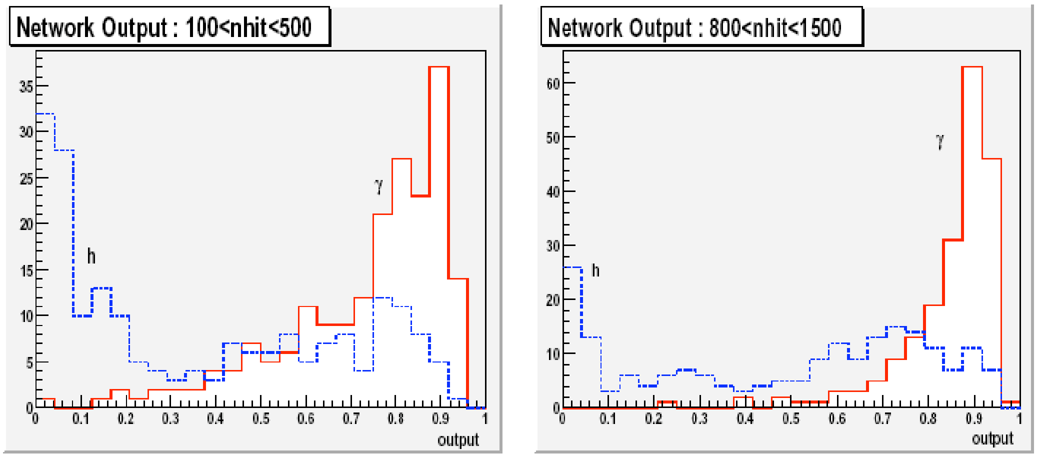

Figure 3.8: *Outputs of the neural network in two of the five considered multiplicity regions*

These events have been studied in order to choose a set of eight image parameters used as input for the ANN. The neural network training has been separately performed using several thousands of events (see Tab. 3.1). The ANN has been then tested by using an independent reduced sample of events and the γ recognition efficiency ϵ_γ together with the proton contamination $(1 - \epsilon_{\rm p})$ has been measured. Figure 3.8 shows an example of ANN output for a couple of multiplicity ranges.

The detector sensitivity to γ-ray sources is defined in Eq. 3.1. The use of a γ-hadron discrimination tool makes the sensitivity to be multiplied by the factor $Q = \epsilon_\gamma / \sqrt{(1 - \epsilon_{\rm h})}$. Table 3.1 summirises the obtained results, showing also the values reached for Q which ranges from about 1.3 for low values of hit multiplicity up to about 2 for higher hit multiplicity values.

nhits	events (γ)	events (p)	$< E_{\rm p} >$(TeV)	$< E_\gamma >$ (TeV)	Q
50÷100	6657	3862	0.8	0.5	1.28±0.01
100÷500	11556	6862	1.8	1.1	1.42±0.02
500÷800	2571	1644	4.9	2.9	2.01±0.10
800÷1500	3087	1963	7.6	4.6	1.78±0.07
1500÷6000	4329	3053	18.4	11.3	1.78±0.06

Table 3.1: Main characteristics of the simulated data sample

The Argo experiment is also being considered to discriminate electromagnetic showers from hadronic ones by means of muon identification. Indeed, as will be showed in Chapter 4, the muon content is one of the characteristics which differentiates the two kinds of shower. This is the subject of this work.

These two methods of background rejection are complementary. Thus, when possible, they can be superimposed. Indeed, the muon identification method will be showed to be effective from median energy equal to about 10 TeV. Around this energy value, the Q factor assumes values comparable to those reached with the method presented in this section. Q rises with the energy up to about 20 in correspondence of 40 TeV using the discrimination by means of muon identification.

Chapter 4

Extensive air shower: physical processes and their simulation

The major aim of this work is the evaluation of the ability of the Argo experiment in rejecting the hadronic cosmic ray background by means of muon identification. The calculation of the quality factor Q, the quantity which measures the background rejection power, has been performed relative to the observation of the Crab nebula: so, photons coming from the nebula constitute the signal to be detected, while ordinary cosmic rays are the background to reject.

Photons from the nebula and hadronic cosmic rays from the space hit the atmosphere, thus producing air showers. The discrimination of background events against signal ones relies on the differences between the two kinds of cascade, electromagnetic and hadronic, respectively. Their characteristics are briefly reviewed in the following, in order to highlight these differences with particular emphasis on the production mechanisms of muons, which are much more abundant in hadronic than in electromagnetic showers. The muon identification method relies on this feature to achieve discrimination between the two types of shower.

The estimate of the Q factor has been realised analysing the generated Monte Carlo data sample whose production is described in detail in this Chapter (Sec. 4.4). The simulation programs CORSIKA and ARGO-G utilised for the description of the atmospheric shower development and detector response simulation respectively, are also discussed in this Chapter.

The value of the quality factor strongly depends on the distribution of the muon multiplicity, determined by the hadronic interaction model implemented in the CORSIKA program: 6 different models are available. A comparison between some of them is presented.

4.1 Extensive Air Shower

Particles coming from outside the Earth's atmosphere constitute the primary cosmic radiation. This is composed by protons, alpha particles, heavier nuclei, electrons and photons. A primary cosmic ray entering the atmosphere interacts with the electrons and nuclei of the atoms and molecules constituting the air: secondary particles can thus be produced. These (together with the primary) proceed to make further collisions, and the number of particles grows. The particle cascade thus formed is named extensive air shower (EAS). Eventually the energy of the shower particles is degraded to the point where ionization losses dominate, and their number starts decreasing. All particles suffer energy losses through hadronic and/or electromagnetic processes. A very energetic primary can create millions of secondaries that begin to spread out laterally more and more from the central axis of the cascade, along their path through the atmosphere, because of transverse momenta acquired by the secondary particles at creation and due to scattering process.

4.1.1 Atmosphere

The elemental composition of the atmosphere is almost constant with altitude. Three are the main elements: N_2 (78%); O_2 (21%); Ar ($\sim$1%). The part of the atmosphere that is interesting for the development of air-showers is the troposphere, which extends from ground level to a height of about 15 Km. Assuming the troposphere to be isothermal ("isothermal atmosphere approximation"), the pressure is related to the altitude by an exponential law:

$$P = P_0 \exp\left(-\frac{h \cdot mg}{kT}\right). \tag{4.1}$$

$H \equiv \frac{kT}{mg}$ is the scale height of the atmosphere, which is usually assumed to be 6.5 Km (even if it can noticeably change from place to place). This is a good approximation: indeed the measured pressure variation in the troposphere follows an exponential form very closely. The density of the troposphere follows the same behaviour:

$$\rho = \rho_0 \exp\left(-\frac{h}{H}\right) \tag{4.2}$$

A physical quantity used in air-shower physics is the vertical atmospheric depth, expressed in g cm^{-2}:

$$X_{\mathrm{v}} = \int_h^{\infty} \rho(h')\mathrm{d}h' \tag{4.3}$$

where h is the altitude at which X_{v} is evaluated. The pressure at sea level, at standard condition, is of 1013 millibars which corresponds to the weight of a column of atmosphere (1033 g) with unitary area (1 cm^2): thus sea level is at vertical atmospheric depth of 1033 g cm^{-2}. The atmospheric slant depth $X(\theta, h)$ is the atmospheric depth along a line inclined with respect to the vertical, which for zenith angles $\theta < 75^{\circ}$ (when the Earth curvature can be neglected) can be approximated as:

$$X(\theta, h) = X_0 \exp\left(-\frac{h}{H}\right) \cdot \sec\theta \tag{4.4}$$

where X_0 is the vertical atmospheric depth at sea level, H is the atmospheric scale height, h is the height above which the slant depth has to be determined and θ is the zenith angle of the line. For zenith angles $\theta > 75^{\circ}$, the Earth curvature must be considered and thus this expression is no more quite accurate.

The interaction probability of a particle in a medium depends on the medium density. Therefore, in the atmosphere this can be well approximated by a decreasing exponential law. Moreover, for a fixed path, the atmospheric density along this path is different depending on its inclination to the vertical (zenith angle). These characteristics are determinant in defining the development of the air-showers.

4.1.2 Electromagnetic showers

Electromagnetic air-showers are those cascades initiated in the atmosphere by photons, electrons or positrons. Photons are attenuated in matter via the processes of photoelectric effect, Compton scattering and pair production. In air, the last one dominate above few tens of MeV. High energy electrons predominantly lose energy in matter by ionisation and bremsstrahlung. The critical energy E_c, that is the energy at which the energy loss by ionisation and bremsstrahlung are equal, is about 80 MeV in air. Thus the development of the electromagnetic cascade is governed by bremsstrahlung from electrons and pair production from photons.

At high energies, ("complete screening" [1]) the pair production length is approximately equal to the radiation length for bremsstrahlung. Indeed, the cross section for pair production can approximately be written as

$$\sigma_{pair} \simeq \frac{7}{9}\frac{A}{N_A} \cdot \frac{1}{X_0} \tag{4.5}$$

where X_0 is the radiation length. Moreover, the energy of the incident particle, at each interaction step, can be assumed to be equally shared among the particles participating in the process. Based on these two hypotheses, a very simple model can be built to describe the main feature of particle multiplication in electromagnetic showers: a photon of energy E_0 starts the cascade after one radiation length, by producing a pair constituted by one electron with energy $\frac{E_0}{2}$ and one positron with energy $\frac{E_0}{2}$. The two charged particles then, after another radiation length, emit energetic bremsstrahlung photons with energy $\frac{E_0}{4}$ each, and so on. Secondary particles production continues until photons fall below the pair production threshold, and energy loss mechanisms of electrons other than bremsstrahlung start to dominate: the number of shower particles decays exponentially.

At depth t (in terms of radiation length X_0), the total number of particles $N(t)$ is

$$N(t) = 2^t \tag{4.6}$$

and the energy $E(t)$ of each particle is

$$E(t) = E_0 \cdot 2^{-t} \tag{4.7}$$

The multiplication continues until the electrons fall below the critical energy E_c: thus

$$E_c = E_0 \cdot 2^{-t_{max}}. \tag{4.8}$$

[1] In air the complete screening limit applies for electrons and photons at energies above ∼40 MeV.

From then on ($t > t_{max}$) the shower particles are only absorbed by the atmosphere. The position of the shower maximum is obtained from Eq. 4.8:

$$t_{max} = \frac{\ln E_0/E_c}{\ln 2} \propto \ln E_0 \tag{4.9}$$

so, t_{max}, the depth at which the shower contains the maximum number of particles N_{max}, depends logarithmically on the primary energy, while $N_{max} = \frac{E_0}{E_c}$ depends linearly on the incident energy.

Longitudinal shower development and lateral distribution function

A more realistic treatment of the process of propagation of particles through the atmosphere involves considering complex diffusion equations taking into account the properties of the particles and their interactions, and the structure of the atmosphere. Some approximations allow to obtain analytical solutions [68]. The expression of the longitudinal development as the number of electrons and positrons as a function of the atmospheric depth, has been elaborated by Greisen [69] in the so called “approximation B”. This approximation is appropriate when the electron energy is larger than the critical energy. It consists in using the expression of the cross section in the “complete screening” limit for the pair production (Eq. 4.5) and bremsstrahlung processes, neglecting Compton scattering. There is also the so called “approximation A” which neglects collision losses, too. The air-shower is considered to have just one dimension: the angular deflection of particles in bremsstrahlung and pair production processes and that due to multiple scattering have been ignored. Eventually, under these hypotheses the electron number N_e as a function of t is:

$$N_e(E_0, s, t) = \frac{0.31}{\sqrt{y}} \exp t(1 - 1.5 \ln s) \tag{4.10}$$

$$s = \frac{3t}{t + 2y} \tag{4.11}$$

$$y = \ln\left(\frac{E_0}{E_c}\right) \tag{4.12}$$

where s is the shower “age”, which is formally a parameter entering the solution of the diffusion equations. Its value is 0 at the point of first interaction and 1 at shower maximum, and a maximum value of two is reached at the shower depth for which the number of particles is less than 1. The shower size as a function of the atmospheric depth for photon-initiated showers is shown in Fig. 1.11.

In order to evaluate the lateral distribution of charged particles in the shower with respect to its axis, besides the hypotheses of the approximation B, Nishimura, Kamata and Graisen also considered the opening angles of the particles during bremsstrahlung and pair production processes (approximation C). Thus the air-shower is described in a tridimensional fashion. The particle density as a function of the distance r from the shower axis is given by:

$$\rho(r) = \frac{N}{(r_M)^2} f\left(s, \frac{r}{r_M}\right) \tag{4.13}$$

$$f\left(s, \frac{r}{r_M}\right) = C(s) \cdot \left(\frac{r}{r_M}\right)^{s-2} \left(1 + \frac{r}{r_M}\right)^{s-4.5} \tag{4.14}$$

$$C(s) = \frac{\Gamma(4.5 - s)}{2\pi\Gamma(s)\Gamma(4.5 - 2s)} \tag{4.15}$$

$$r_M = \frac{21 X_0}{E_c} \tag{4.16}$$

where N is the total number of charged particles in the shower and r_M is the Møliere radius. The function $f\left(s, \frac{r}{r_M}\right)$ is the lateral distribution. An infinite cylinder of radius 3.5 times the Møliere radius contains 99% of the totatal energy of the air-shower. At 2000 m a.s.l. $r_M \sim 100$ m and at 4300 m a.s.l. $r_M \sim 133$ m.

Muon

Direct μ^+ μ^-- pair production and photonuclear reactions with protons and neutrons of nuclei of the atmosphere are, in spite of their small cross section, the processes responsible for muon production in an electromagnetic shower. These processes subsequently described in Sec. 4.2.1 are characterised by cross section of the order of 10 and 100 μb, respectively, to be compared to the electron-pair production cross section which is of the order of barn. That is why electromagnetic showers are poor in muons.

4.1.3 Hadronic showers

The hadronic showering process is dominated by a succession of inelastic hadronic interactions. Hadronic cosmic rays entering the atmosphere are subject to strong interactions in collisions with atmospheric nuclei, such as nitrogen and oxygen. Part of the primary energy is transformed into rest mass of new hadrons (mostly pions, and sometimes kaons), another part of it goes into their kinetic energy, and another part goes into disrupting the target nucleus with subsequent emission of protons and neutrons.

Energetic primary particles and, in case of heavy primaries, their spallation [2] fragments, continue to propagate in the atmosphere and interact successively, producing more particles along their trajectories, and likewise for the newly created energetic secondaries. This continues until the energy per hadronic particle drops below ~ 1 GeV, the energy necessary for multiple pion production. The most abundant particles emerging from energetic hadronic collisions are indeed pions, but kaons, hyperons, charmed particles and nucleon-antinucleon pairs are also produced.

The development of an EAS for a given energy and primary is mainly dependent on two factors: the inelastic cross-section σ_{inel} of primary and secondary particles with air and the average fraction of the available energy transferred into secondary particles (usually named inelasticity k_{inel}).

Cosmic radiation is composed above all by protons, thus the most frequent first interaction is proton - nucleus. The proton - nucleus (or more in general nucleon - nucleus) interaction cross section $\sigma_{p,A}$, scales with respect to the proton - proton (or nucleon - nucleon) cross section $\sigma_{p,p}$ approximately as

$$\sigma_{p,A}(E) = \sigma_{p,p}(E)A^{\alpha}. \tag{4.17}$$

Figure 4.1 shows the total and elastic cross section of the proton - proton interaction. $\sigma_{p,p}(E)$ varies slowly over a range of many decades in energy, from $\sim$40 mb at 10 GeV to $\sim$80 mb at 10^7 GeV. The interaction mean free path λ_i can be calculated from the interaction cross section σ_i:

$$\lambda_i = \frac{A}{N_A \sigma_i} \tag{4.18}$$

where N_A is Avogadro's number, and A the mass number of the target nucleus. In case of proton inelastic collisions in air, the interaction mean free path is $\lambda_i \simeq 80 \text{ g/cm}^2$, so

[2] A nuclear reaction induced by high energy bombardment and involving the ejection of two or more small particles or fragments leaving only one large residual nucleus.

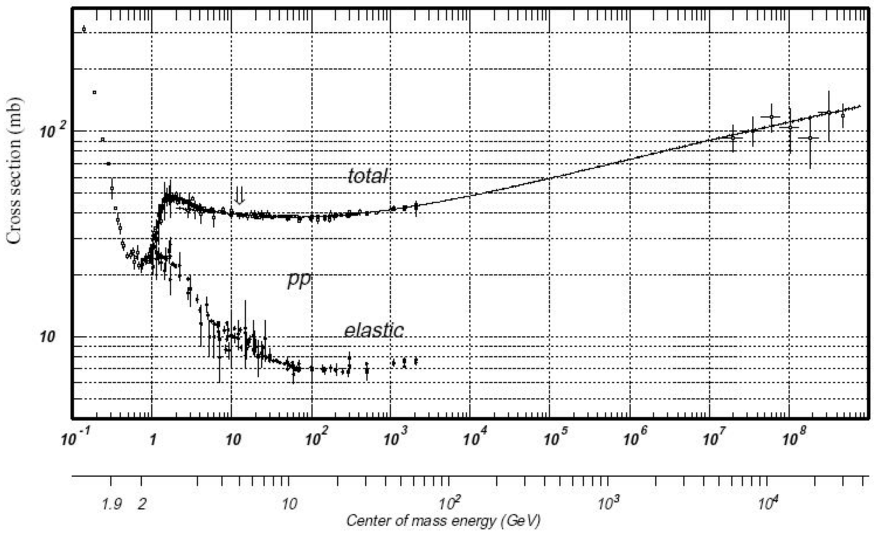

Figure 4.1: *Total and elastic pp cross section as a function of laboratory beam momentum and total center of mass energy.*

protons undergo on average 12 interactions along a vertical trajectory trough the atmosphere down to sea level. For comparison, for a projectile nucleus with mass number A = 25, the interaction mean free path is approximately 23 g/cm^2 in air, corresponding to about 50 interactions for vertical trajectory trough the atmosphere. So there is no chance for a heavy nucleus to penetrate down to the sea level. Most of the primary heavy nuclei are fragmented in the first interaction, which occurs at a higher altitude than in the case of protons because of the much larger interaction cross section and correspondingly shorter interaction mean free path.

Hadrons may suffer energy losses due to strong interactions in collisions with nucleons and nuclei when propagating in a medium. A hadron with initial energy E_0, undergoing n interactions with a mean inelasticity $< k >$ will retain on average an energy E: $E = E_0(1- < k >)^n$. For a vertically incident high energy proton traversing the full atmosphere down the sea level, $< k >= 0.5$ and n = 12, so that the energy reduction factor is $\frac{E}{E_0} = (0.5)^{12} \simeq 2.5 \cdot 10^{-4}$

Secondary particles

As already remarked, pions are the most abundant secondary particles produced in the development of a hadronic shower. Figures 4.2a and 4.2b show the interaction cross

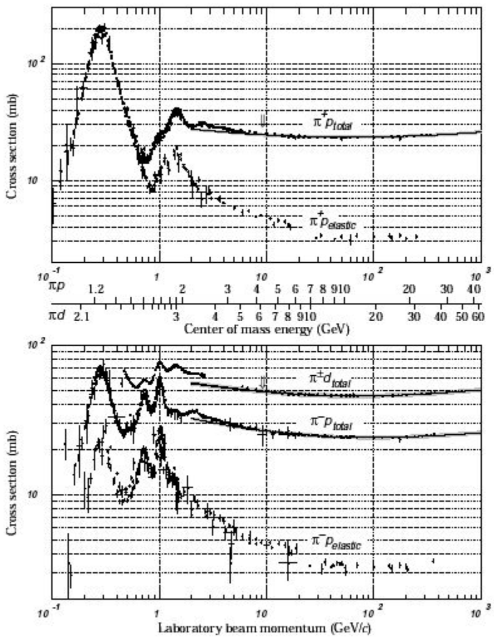

(a)

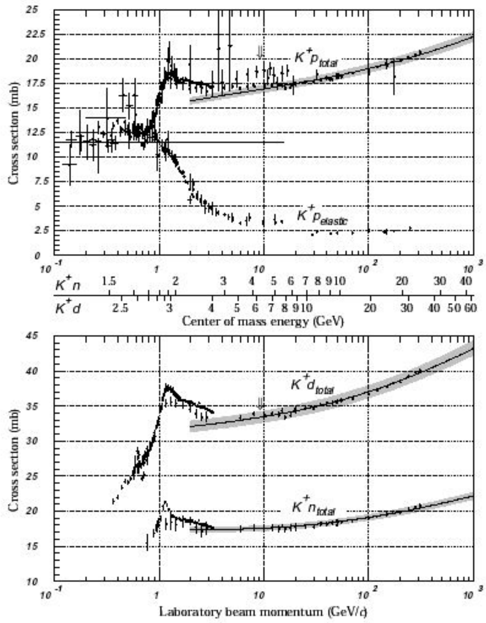

(b)

Figure 4.2: *Total and elastic π^+p (a) and k^+p (b) cross section as a function of laboratory beam momentum and total center of mass energy.*

section for pion - proton, $\sigma_{\pi,p}(p)$ and kaon - proton $\sigma_{k,p}(p)$ respectively, as a function of the incident momentum. Above an incident momentum of few GeV, the values both cross sections are approximately constant to within 10 mb and after a decrease. The interaction probability of the mesons depends on their energy and on the atmospheric density, which is a decreasing exponential function of the altitude (Sec. 4.1.1). Most of the secondary particles resulting from hadronic interactions are unstable and can therefore decay on their way through the atmosphere. Their decay probabilities must be known and properly accounted for, when calculating particle fluxes and energy spectra.

At high energies, the particle mean life $\tau(E)$ is significantly extended by time dilation.

The mean life of an unstable particle of energy E is given by

$$\tau(E) = \tau_0 \gamma(E) = \tau_0 \left(\frac{E}{m_0 \cdot c^2} \right) \tag{4.19}$$

where τ_0 and m_0 are the mean life and the mass of the particle in its rest frame. The distance l travelled during the time interval τ is $l = v\tau = \gamma\beta c\tau_0$. The mean free path in g cm^{-2} units, for spontaneous decay in a medium with density ρ is $\lambda_d = \gamma\beta c\tau_0\rho$. In the same medium, if N_0 is the initial particle population and dN is the number of particles decaying in an element of thickness dX, where X is the length in g cm^{-2}, then $N(X)$ the number of particles remaining after having traversed the thickness X, is:

$$dN = -\frac{N\mathrm{d}X}{\lambda_d} \tag{4.20}$$

$$N(X) = N_0 \exp\left(-\int \frac{m_0 \mathrm{d}X}{\rho\tau_0 p} \right) \tag{4.21}$$

and the decay probability is

$$W(X) = \frac{N_0 - N(X)}{N_0} = 1 - \exp\left(-\int \frac{m_0 \mathrm{d}X}{\rho\tau_0 p} \right) \tag{4.22}$$

If an unstable particle is incident at a zenith angle $\theta > 0°$, the probability for decay along its prolonged path to a particular atmospheric depth X is enhanced by the factor $\sec(\theta)$. So, for a given path length $X\sec(\theta)$, the particle decay probability depends on its mean life and its energy. As already noted, the interaction probability for the particle in air is not only a function of the energy but also of the atmospheric density. Therefore, eventually, the competition between interaction and decay depends on the mean life and the energy of the particles, as well as on the altitude and zenith angle.

The pion - nucleus interaction cross section can be estimated from Eq.4.17: for pion projectiles $\alpha = 0.75$ and $\sigma_{\pi,p}$ is approximately 26 mb (see Fig. 4.2a) in the energy range from 10 GeV to 1 TeV and therefore their interaction mean free path in air is $\sim$ 120 g cm^{-2}. Charged pions have a mean life at rest of $\sim$2.6$\cdot 10^{-8}$ s. Thus, below 10-100 GeV the pion decay becomes dominant over the interaction with air nuclei. Pion decays give rise to the muon and neutrino components which easily penetrate the atmosphere. Despite a mean life of $2.2 \cdot 10^{-6}$, most muons survive down to sea level because of time dilation. Kaons have behaviour similar to pions, but with a larger number of available decay channels.

Neutral pions decay almost instantly ($\tau \simeq 10^{-16}$) to two photons, which can initiate electromagnetic cascades.

Hadronic showers have a hadronic core acting as a source of electromagnetic sub-showers generated mostly from the neutral pion decays. The resulting electrons and positrons are the most numerous particles in the shower. The number of muons produced by the charged meson decays is an order of magnitude lower. The lateral spread of a shower is determined largely by Coulomb scattering of the many low-energy elecrons and thus is characterised by the Moliere radius. The lateral spread of muons is larger and depends on the transverse momenta of the muons at production as well as multiple scattering. Therefore, also in hadronic showers the lateral distribution of charged particles is rather well described by the Nishimura-Kamata-Greisen function (Eq. 4.13) which has been calculated from electromagnetic cascade theory, even if the parameter s looses its meaning of shower age parameter and showers are not described well over the whole distance range by the NKG function with a single value of s.

Muons

Muons are produced as a consequence of the hadronic interaction between cosmic rays and the nuclei of the atmosphere. Meson decay, mainly by pions and kaons (but also charmed particles) is the main mechanism for the muon production. Pions and kaons also interact with the atmosphere: the probability for a pion or a kaon to decay instead of interacting depends on its energy, as shown in Eq. 4.19, the available decay length before the particle hits the Earth surface and the density of the atmosphere. At very low energies basically, all mesons decay into muons, while, as pion or kaon energy increases, fewer particles decay because of the competition between decay and interaction described in Sec. 4.1.3. At energies below 100 GeV, the probability for a pion or kaon to decay in flight is rather large: as the energy grows, the chances for an interaction to occur before decay get higher and higher. The muon path in the atmosphere is determined by its properties:

- The muon lifetime is $\sim 2.2 \cdot 10^{-6}$ s, but it is extended for an observer on Earth because of time dilation. Muons with energy above 100 GeV can be almost considered stable particles [72].

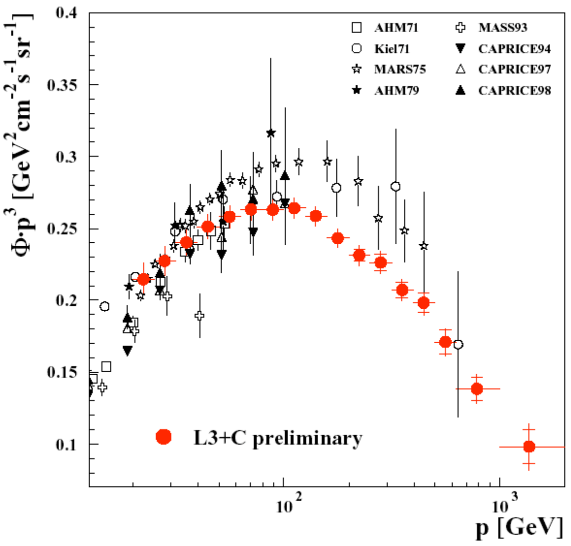

Figure 4.3: *Measured muon flux [70], [71]*

- The muon critical energy in air, at standard temperature and pressure, is $E_c \simeq 3.6$ TeV [72].
- Its cross section for interactions with hadrons is small.

This results in the muon flux shown in Fig. 4.3, as a function of muon momentum. The maximum at low energy reflects the fact that pratically all low energy mesons decay into muon whose decay-probability and energy loss are more and more important as their energy decreases. At energies between 10 and 100 GeV the meson decay probability is large and the spectrum steepens gradually to reflect the primary spectrum and steepens further at higher energy because the meson decay probability lowers and thus mesons interact with the atmosphere (pions with E >115 GeV tend to interact in the atmosphere before they decay). For higher (1 TeV) energies the muon spectrum steepens by one power of the energy. A small fraction of high energy muons are the result of direct production processes.

The vertical flux of muons with energy above 1 GeV as a function of the atmospheric depth, resulting from the action of these mechanisms, is plotted in Fig. 4.4, which shows that at atmospheric depth above about 700 $\mathrm{g\ cm^{-2}}$, the most abundant charged particles

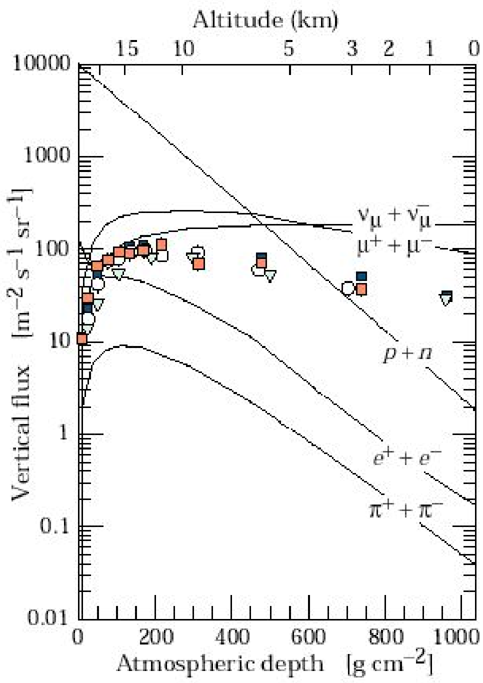

Figure 4.4: *Estimate of the vertical fluxes of cosmic rays with $E > 1$ GeV as a function of the atmospheric depth. The points show measurements of negative muons with $E > 1$ GeV [73]*

(at energies above 1 GeV) are muons. Indeed, muons are traditionally called the "penetrating component" of cosmic rays. Moreover, they are charged, and thus quite easy to detect. Most of them are produced high in the atmosphere (typically 15 Km) and lose about 2 GeV of energy because of ionisation before reaching the ground at sea level. Here, the mean energy of muons is 4 GeV.

The number of muons in an EAS depends on the probability that a pion will decay rather than interact, and hence, depends on the pion energy and the local air density. At production heights of 5 Km, pions of energy less than 30 GeV are more likely to decay than to interact; at greater heights, where the air density is smaller, the interaction process becomes less likely favouring pion decay even at high energy. It follows that the highest energy muons detected at sea level reflect processes occurring early in the shower development.

4.1.4 Differences between electromagnetic and hadronic showers

The development of the cosmic-ray and photon-initiated showers has already been described in the previous sections. Figure 4.5 gives an example of the two kinds of shower having both primary energy equal to 1 TeV: the pure electromagnetic shower is shown on the left side, and the hadronic one on the right side. Cosmic-ray showers are much more chaotic than the γ-ray ones, which tend to be very smooth and have most of their particles located near the core. Indeed, the transverse momentum of hadronic interactions is much greater than that of electromagnetic ones; the average transverse momentum of hadronic interactions is approximately 400 MeV, while the transverse momentum characterising the electromagnetic showers is mainly due to the multiple scattering. Secondary particles in electromagnetic showers are mostly electrons, positrons and photons as well as in hadronic ones, but the latter also contain other types of particle among which are muons. Moreover, on average γ-ray showers have more particles than cosmic-ray showers of the same energy. This is because much of the energy in cosmic-ray showers is carried off by muons. Since muons do not readily interact, there is less energy available for the production of new particles.

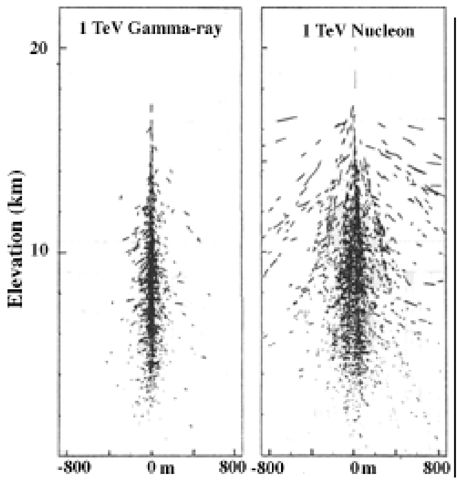

Figure 4.5: *Electromagnetic (left) and hadronic (right) air-showers generated by primaries with energy equal to 1 TeV*

4.2 Simulation of EAS: CORSIKA

CORSIKA [74] (COsmic Ray Simulations for KAscade) is a Monte Carlo program to simulate the development of the extensive air showers initiated by high energetic cosmic ray particles in the atmosphere. Primaries can be protons, light nuclei up to iron, photons and many other particles with energy equal to the highest energies observed ($E_0 > 10^{20}$ eV). The software development is based on the idea to predict not only correct average values of observables, but also to reproduce the correct fluctuations around these values.

Particles are tracked through the atmosphere until they undergo reactions with the air nuclei or, in the case of unstable secondaries, decay. The particle transportation range before it undergoes its next interaction or decay depends on the reaction cross section together with the atmospheric density distribution along the flight path and the probability to decay, as discussed in Sec. 4.1.3. Stable particles can only interact, for unstable ones the two processes compete. A decay length and an interaction length are determined independently at random and the shorter one is chosen as the actual path length. By this procedure is also decided wether a particle decays or interacts. In decays all branches down to the 1 % level are considered with correct kinematics in the 3-body decays. Charged particles lose energy by ionization which especially affects muons at energies below ≈10 GeV because of their long lifetime and low interaction cross section, while neutral particles proceed without energy loss. Because of the large penetration depth of $\mu^{\pm}$ a deflection due to multiple Coulomb scattering is taken into account. This is neglected for charged hadrons. During transport, the deflection of charged particles by the Earth's magnetic field is considered.

The CORSIKA program consists basically of 4 parts:

- a general frame including input and output management, decay of unstable particles, tracking of the particles considering ionization energy loss, deflection by multiple scattering and by the Earth's magnetic field;
- simulation of the hadronic interactions of hadrons and nuclei with the atmospheric nuclei at energies above 80 GeV which can be treated by the models DPMJET [75], HDPM [76], QGSJET [77], SIBYLL [78], VENUS [79] or NeXus [80], briefly discussed in section 4.2.2;

- hadronic interactions at energies below 80 GeV;
- interactions of photons electrons and positrons.

4.2.1 Electromagnetic interaction models

Electron and photon reactions are treated with EGS4 (Electron Gamma Shower system version 4) or with the analytic NGK (Nishimura Kamata Greisen) formula. The formers delivers detailed information (momentum, space coordinates, propagation time) of all electromagnetic particles, but need extended computing times increasing linearly with the primary energy, while the latter works fast but gives only electron densities at selected point in the detection plane.

EGS4 model

The EGS4 option enable a full Monte Carlo simulation of the air shower electromagnetic component. In the EGS4 model, gamma rays may andergo Compton scattering, e^+ e^--pair production and photoelectric effect while electrons and positrons are subjected to annihilation, Bhabha scattering, bremsstrahlung, Møller scattering and multiple scattering (according to Molière's theory). The programming of these standard interactions is well documented in [81].

Two processes despite their small cross section have been added in order to simulate muon production in electromagnetic showers:

1. the direct μ^+ μ^-- pair production;
2. the photonuclear reaction with protons and neutrons of nuclei of the atmosphere .

The μ^+ μ^- pair production is treated in full analogy with e^+ e^- pair production, substituting the electron rest mass with the muon rest mass. In the high energy limit the cross section for this process approaches to

$$\sigma_{\mu^+\mu^-} = \frac{{m_e}^2}{{m_\mu}^2}\sigma_{e^+e^-} \tag{4.23}$$

and reaches 11.4 μb above E_γ = 1 TeV.

The cross section of the photonuclear reactions with air is calculated by means of the proton cross section by multiplication with the factor $A^{0.91}$ = 11.44 [82]. In photonuclear interactions the nucleus is considerate a superposition of free nucleons and only one of them can undergo photonuclear reaction. Measurements of the proton photon produc-

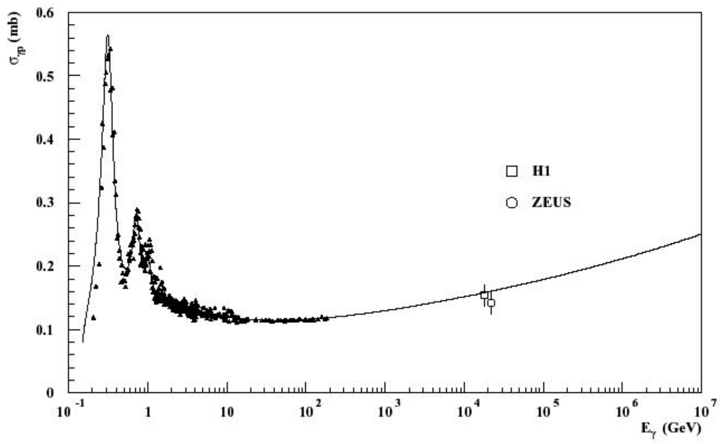

Figure 4.6: *Proton-photon production cross section as a function of the incident photon energy*

tion cross section as a function of the incident photon energy E_γ are shown in Fig. 4.6 together with their parametrization consisting of three resonances at E_γ = 0.32, 0.72 and 1.03 GeV, superimposed on a continuum which slightly increases with energy

$$\sigma_{\gamma p} = \left(73.7s^{0.073} + \frac{191.7}{s^{0.602}}\right)\sqrt{\frac{s-s_0}{s}} \tag{4.24}$$

where s is the squared cms energy and s_0 is the pion production threshold energy in the center of mass system both expressed in GeV^2. $\sigma_{\gamma p}$ is in μb. Secondary particle generation is a function of the incident photon energy:

- $E_\gamma < 0.4$ GeV only one pion is generated;
- 0.4 GeV $< E_\gamma <$ 1.4 GeV the chance to generate one pion decreases linearly in favour of the generation of two pions;
- 1.4 GeV $< E_\gamma <$ 2 GeV two pions are produced;
- 2 GeV $< E_\gamma <$ 3 GeV the chance to generate two pion decreases linearly in favour of the HDPM multi-particle generation;

- 3 GeV $< E_\gamma <$ 80 GeV multi-particle production by the HDPM package is always assumed;
- $E_\gamma >$ 80 GeV the selected high energy model is employed.

Nishimura-Kamata-Greisen model (option)

The NGK option does not provide a full Monte Carlo simulation. The air shower electromagnetic component is derived with an analytical calculation [83]. This kind of approach allows to obtain only the total electron number at varoius atmospheric depths together with some parameters that give information about the general development of the electromagnetic component of a shower. At one or two observation levels lateral electron densities are computed for a grid of points around the shower axis.

4.2.2 Hadronic interaction models

While the electromagnetic interaction and the weake interaction are well understood, the major uncertainties in EAS simulation arise from the hadronic interaction models. With the present theoretical understanding of soft hadronic interaction, i. e. those with a small momentum transfer, one cannot calculate interaction cross-sections or particle production from first principles. Therefore, hadronic interaction models are usually a mixture of fundamental theoretical ideas and empirical parametrizations tuned to describe the experimental data at lower energies.

The highest energy reached in a man-made accelerator is at present of the order of $E_{lab} = 1$ TeV. This is about 8 orders of magnitude smaller than the highest energy ever measured for a cosmic ray particle. Events triggered and examined at accelerator experiments are those that produce particles with high momentum transfer. They are well described by QCD but they constitute only a minute fraction ($\ll 10^{-6}$) of the overall reaction rate. Interactions with low momentum transfer, i. e. soft collisions, produce particles with small transverse momenta that mostly escape undetected in the beam pipe. Of special importance are the diffractive dissociation events, which originate from rather peripheral collisions with a small fraction of energy transferred into secondary particles: these reactions indeed, carry the energy deep down into the atmosphere and thus drive the air shower development. Moreover, most of the collisions contributing to the air-shower development are nucleon-nucleus or nucleus-nucleus collisions, for which accelerator data are available only at much lower energies, rather than proton-proton collisions. Therefore models based on accelerator results have to be extrapolated in order to account for interactions in the kinematic range of very forward particle production, to higher energies and to other projectile-target combination.

In order to study the influence of models on the uncertainties of EAS observables and on their correlation, 6 different hadronic interaction codes have been coupled with CORSIKA. Their basic features are summarised in Tab. 4.1. QGSJET, VENUS, DPMJET and

Model	VENUS	neXus	QGSJET	DPMJET	SIBYLL	HDPM
Version	4.12	2		II.4/II.5	1.6/2.1	
Gribov-Regge	+	+	+	+		
Mini-Jets		+	+	+	+	
Sec. Interactions	+	+				
N-N interaction	+	+	+	+		
Superposition					+	+
Max. Energy (GeV)	$2 \cdot 10^7$	$2 \cdot 10^8$	$> 10^{11}$	$> 10^{11}$	$> 10^{11}$	10^8

Table 4.1: *Essential features of hadronic interaction models [84].*

NeXus are models based on the Gribov-Regge theory (GRT) which considers single and multiple Pomeron exchange as the basic process in high energy hadron-hadron scattering, while SIBYLL is a minijet model. HDPM model extrapolates experimental data from low to high energy and from p to nuclei with simple theoretical ideas. Nuclei are trated as superposition of free nucleons.

The cross section and inelasticity are the main physical quantity which characterise the longitudinal development of an EAS. Figure 4.7 shows a summary of the experimental and simulated data relative to the inelastic p-air cross section σ_{p-air} as a function of the incident proton momentum p_{lab}. The simulated values are predicted using the different models. The cross section differences between the models have shrunk from 80 mb to 20 mb in the region at a few PeV, from 1997 to 2000: they agree to within about $\sim 6\%$

[84].

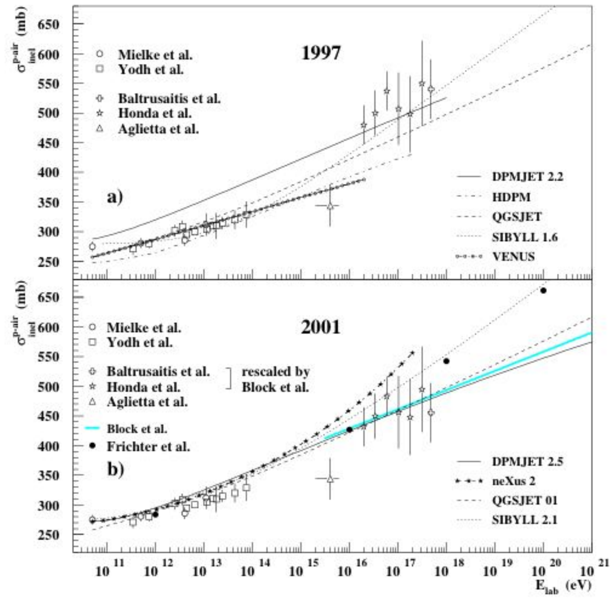

Figure 4.7: *Inelastic p-air cross sections in the years 1997 and 2000 [85] [86] [87] [88] [89] [90]*

The longitudinal development of an EAS mainly determined by the cross section and inelasticity is closely related to the most important shower observables: the particle number at ground level and their lateral distribution, the height of shower maximum X_{max} and the total energy deposited in the electromagnetic component. Figure 4.8 shows the longitudinal shower development (number of electrons and positrons as a function of the atmospheric depth) for proton and iron induced vertical showers with energy $E_0 = 10^{14}$ eV and $E_0 = 10^{15}$ eV. The X_{max} position variations between the models are below 1%. The particle numbers at sea level (1036 g/cm^2) for proton and iron showers differ of about 14% and 3% respectively at 10^{15} eV, becoming even smaller at lower energies[84].

Muon production simulation with different packages

The simulation program CORSIKA coupled to three packages VENUS, SIBYLL and QGSJET has been used to generate three different samples of proton-initiated air-showers with primary energy 20 TeV in order to study their muon multiplicity. Figure 4.9 shows the distribution of the muon multiplicity for muons with energy above 1 GeV, collected

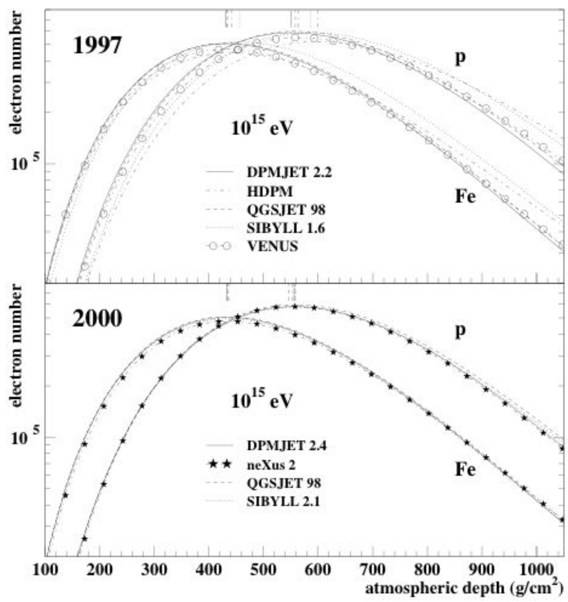

Figure 4.8: *Number of electrons and positrons as a function of the atmospheric depth in proton and iron initiated showers with primary energy* 10^{15}eV *in the years 1997 (top) and 2000 (bottom)*

on an area of about 1100 m^2 at 4300 m a.s.l.. The packages QGSJET and VENUS give results which are in good agreement while their simulated muon multiplicity differs from the one obtained with the SIBILL package by about 20%.

4.3 Detector simulation

The Monte Carlo program developed to simulate the Argo-YBJ detector is based on the GEANT3 CERN package and is called ARGO-G [91]. GEANT3 provides a set of standard tools which allow to:

- describe an experimental setup in a rather efficient and simple way;
- generate simulated events with standard or user written Monte Carlo generators;
- track particles through the setup taking into account all relevant physical phenomena (interactions, energy losses, etc.);
- record the response from the sensitive element of the detector;

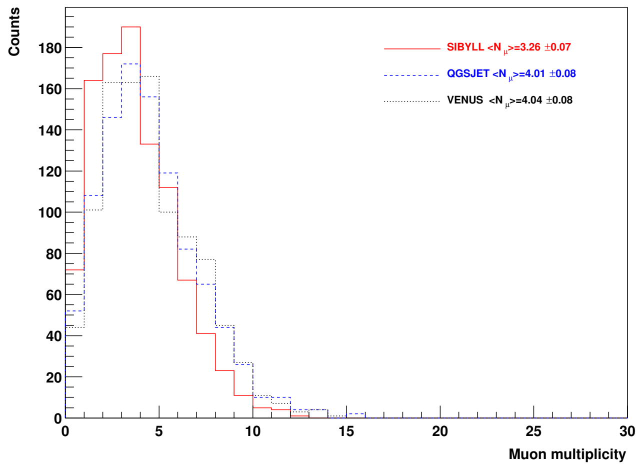

Figure 4.9: *Muon multiplicity in proton-initiated air-showers with primary energy equal to 20 TeV, generated using different models for the simulation of hadronic interaction. Muons are collected over an area of about 1100 m^2*

- visualize detectors and particle trajectories.

GEANT3 code consists in a set of routines to be assembled into a main program and sub-programs. The information which describes the experimental setup and the appropriate instructions which control the execution of the program can be provided by means of data cards. They are user instructions meant to offer the possibility to override default values of the program at execution time. They are divided in two categories:

- GEANT3 data cards which are employed for general control of the run, control of physics processes, debug and I/O operations, user applications;

- ARGO-G data cards. They are additional data cards, defined in the subroutine "GACARD", in order to manage the detector geometry, the event generation and the input/output files.

The execution of the ARGO-G program consist in a loop over any number of simulated events which are γ or hadron initiated air showers (CORSIKA) developed through the atmosphere down to the detector level: particles (mainly photons, electrons, positrons and muons) of the showers which enter the detector setup are tracked inside it, eventually producing "hits" when they traverse the sensitive volume.

4.3.1 Geometrical structure of the detector

In GEANT3 any detector setup has to be represented as a structure of geometrical VOLUMES. All volumes used so far in ARGO-G have the shape of a box. MARS, the main volume, includes the rest of the volumes which form the detector setup as sub-volumes. The Master Reference Frame used in the program has its origin in the geometrical center of MARS.

The largest sub-volume of MARS including the entire detector setup is ARGO, conceived as a fictitious box filled of air, positioned in the quadrant of positive X and Y coordinates of the Master Reference Frame.

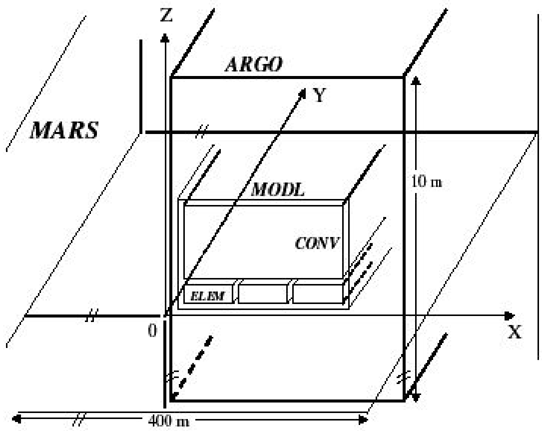

Figure 4.10: *Geometry and volume structure of Argo setup in ARGO-G*

The basic volume ARGO contains a variable number of equal sub-volumes, MODLs (their value can be set by the user), placed at Z=0 level and also another volume (TPLA) for the building roof. Each MODL consists of 3 equal sub-volumes placed along the X axis, called ELEM, and 1 upper volume, CONV, which can contain 1 or more converter planes as chosen by the user (data cards NCPL CPLA), together with their material and thickness. Figure 4.10 shows this geometrical arrangement.

The volume ELEM includes 1 RPC chamber and two gaps along X and Y directions

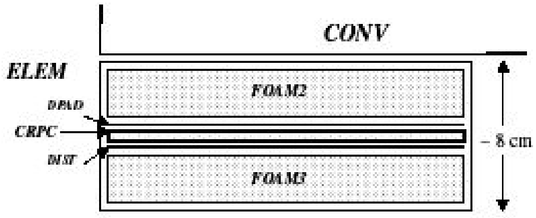

Figure 4.11: *Stratigraphy of Volume ELEM*

which separate neighboring (contiguous) RPCs. Figure 4.11 shows the structure of ELEM, namely the RPC layers.

The user can set the dimensions of the detector to be simulated by choosing the total number of CLUSTERs which consist in 2X2 MODLs, that is 12 RPCs, as shown in Fig. 4.12.

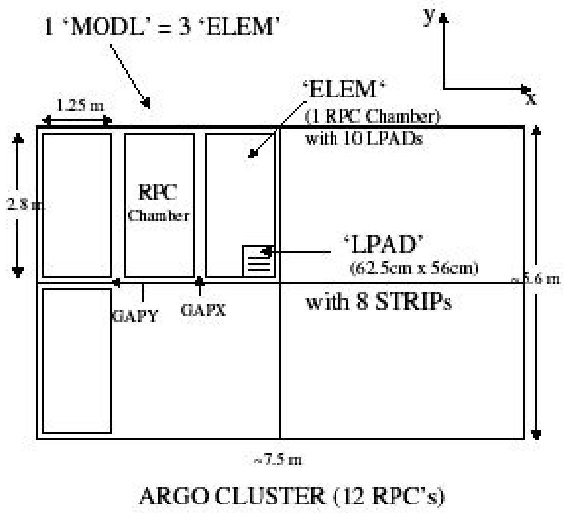

Figure 4.12: *Layout of the CLUSTER unit ARGO-G*

4.3.2 Sensitive volumes and digitization.

In any GEANT application, the sensitive volume of the detector setup are grouped in SETS. In ARGO-G (v. 1.1) RPCH is the only SET used. It contains 2 sensitive sub-volumes: CGAS and LPAD. The first one includes the RPC gas, while the second one the logical unit PAD. For each charged particle crossing the sensitive volume of the detector CGAS at least 1 HIT is generated containing the following parameters:

1. X x position of the hit in MARS
2. Y y position of the hit in MARS
3. Z z position of the hit in MARS
4. PX x-momentum of the particle producing the hit
5. PY y-momentum of the particle producing the hit
6. PZ z-momentum of the particle producing the hit
7. XEL x position of the hit in ELEM
8. YEL y position of the hit in ELEM
9. STRIP absolute number of STRIP fired by the hit
10. TIME time of flight of the particle producing the hit

LPAD is not a real sensitive volume: it is used to obtain the digitization of the signal induced on the strips by the RPC discharge. Digitization consists in the simulation of electronics response (timing and position) when charged particles produce discharges in RPC chambers. Every DIGIT includes the following information:

1. MODL number
2. ELEM number in MODL
3. PAD number in ELEM
4. number of fired STRIPs on PAD
5. STRIP pattern on PAD
6. number of charged particles on STRIP
7. PAD timing (TDC)

The tracking of an event is controlled in the routines GUTREVE and GUTRACK.

4.4 Data sample production.

The study of the background rejection by means of muon identification with the Argo experiment requires the generation of simulated events, both for signal and background. The signal has been assumed to be the photons emitted from the Crab nebula, while the background is constituted in very good approximation only by protons coming from the direction of the nebula. The simulation programs utilised for the generation of the data samples and for the simulation of the detector response are the ones described in Sec. 4.2 and in Sec. 4.3 respectively:

1. CORSIKA version 6.014;
2. ARGO-G version 1.34.

Both have been modified with respect to their standard versions. The event reconstruction, described in Sec. 4.4.3, has been performed by means of the Medea++ 3.0 program [94], [95].

4.4.1 Photon and proton simulation by means of CORSIKA

In its standard configuration, the CORSIKA program gives the possibility to generate atmospheric shower within a solid angle Ω, chosen by means of data card setting, in the Elevation-Azimuth Coordinate System of the detector.

In order to follow the emission of the Crab during its motion in the sky, the transformation equation from the Equatorial Coordinate System to the Elevation-Azimuth Coordinate System has been introduced in the CORSIKA program: thus, given the right ascension and the declination of the simulated source and its observation time, the correspondent zenith and azimuth in that instant can be calculated. In fact, the changes brought allow not only the Crab nebula but any other source to be followed in the sky. The total observation time can be chosen from 2000 January the 1^{st} by means of a new data card. The generation time of each event is then randomly determined during the total time interval in which the source path is simulated. During the motion in the sky, the plane containing the detector is seen under different zenith angles θ, and its projection on a surface perpendicular to the shower axis has a $\cos\theta$ behaviour. This effect is

RUNNR	141509	substitute by script
EVTNR	1	number of first shower event
NSHOW	100	number of showers to generate
PRMPAR	14	
ESLOPE	-1	
ERANGE	1000 10000	
DIRCTN	TRUE	
RASCEN	5.575	
DECLIN	22.01666	
DAYS	365	
THETAP	0 0	
PHIP	0. .	range of azimuth angle (degree)
SEED	673475901 0 0	substitute by script sequence1
SEED	748575073 0 0	substitute by script sequence2
SEED	0 0 0	substitute by script sequence3
OBSLEV	4300.E2	observation level (in cm)
ELMFLG	F T	em. interaction flags (NKG,EGS)
RADNKG	200.E2	outer radius for NKG lat.dens.distr.
ARRANG	0.	rotation of array to north
FIXHEI	0. 0	first interaction height - target
FIXCHI	0.	starting altitude (g/cm**2)
MAGNET	34.5 35.0	magnetic field centr. Europe
HADFLG	0 0 0 0 0 2	flags hadr.interact.-fragmentation
QGSJET	T 0	use QGSJET for high energy hadrons
QGSSIG	T	use QGSJET hadronic cross sections
ECUTS	0.05 0.05 0.001 0.001	energy cuts for particles
MUADDI	F	additional info for muons
MUMULT	T	muon multiple scattering angle
LONGI	F 100. F F	longit.distr. - step size - fit - out
MAXPRT	1	max. number of printed events
ECTMAP	1.E4	cut on gamma factor for printout
STEPFC	1.0	mult. scattering step length fact.
DEBUG	F 6 F 1000000	debug flag and log.unit for out
DIRECT		output directory1
DATBAS	T	write .dbase file
USER	root	user
EXIT		terminates input

Table 4.2: *Input data cards.*

rightly taken into account sampling the events according to a $\cos\theta$ distribution.

Table 4.2 shows the data cards included in the input file used with CORSIKA. The bold-faced data cards are the new ones introduced to allow the simulation of some source:

- "DIRCTN" is a logic parameter: when its value is "false", the standard simulation is performed, otherwise the photon emission of a source can be simulated.
- "RASCEN" and "DECLIN" are, respectively, the right ascension and the declination of the object.
- "DAYS" is the number of days during which the source motion is tracked.

The value of the "standard" data cards are the ones used by the Argo-YBJ Collaboration: hadronic interaction has been simulated by means of the GHEISHA and QGSJET models at energies below and above 80 GeV respectively; EGS4 has been used for an accurate simulation of the electromagnetic interaction and QGSJET model has been showed to provide the best overall description of EAS data by independent analyses [92] [93].

Data Sample Type	Events Number	Energy Range	Spectral Index
Photons	406820	1TeV-50TeV	-1
Protons	530718	1TeV-50TeV	-1
Protons	94130	50TeV-100TeV	-1
Photons	72150	50 TeV-100TeV	-1

Table 4.3: *Main characteristics of simulated data samples.*

The main characteristics of the simulated samples are summarised in Tab 4.3. Photon, as well as proton, initiated air-showers have been generated in two different energy ranges: the first one varies from 1 TeV up to 50 TeV, while the second one from 50 TeV up to 100 TeV. The number of the events relative to the samples with different energy has been chosen in order to obtain a continuous energy distribution within the entire range, both for protons and photons. Figure 4.13 shows the primary energy distribution from 1 TeV up to 100 TeV for proton-generated air-showers.

The simulated spectral indexes (both for proton and photon spectra) have been decided to be equal to -1 instead of the measured values, with a view to reduce the long simulation time and to generate a data sample much more populated at high energy than at low energy. This choice is a compromise between the long simulation time and the need to have a statistically significant number of events at high energy. Then, the analysed events, after the reconstruction, are properly weighted, as described in Sec. 4.4.4. As far as the background simulation is concerned, the number of generated protons is enhanced of 20% to account for the helium presence, in first approximation.

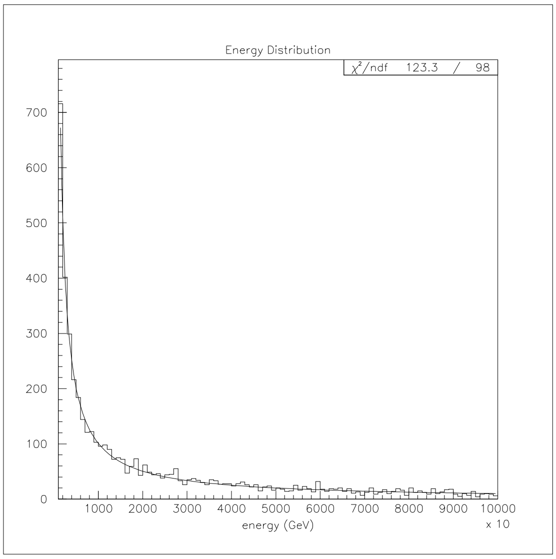

Figure 4.13: *The primary energy distribution of proton-initiated air-showers.*

4.4.2 Detector response simulation by means of ARGO-G

The simulated detector is constituted by a full carpet of 14×17 RPC clusters (the ring can be simulated turning off the appropriate clusters in the reconstruction program). It is covered by a 0.5 cm thick layer of lead in order to convert a fraction of the secondary gamma rays in charged particles, and to reduce the time spread of the shower particles. The trigger is set at a minimum pad multiplicity equal to 20. The noise is simulated by randomly generating hits with an average frequency of 400 Hz. The input of the ARGO-G program is constituted by the data sample generated with Corsika. Table 4.4 gives the values of the input data cards used in order to simulate the Argo detector response. The number of the events are ten times processed. They are randomly distributed on the generation area A_g, which has been chosen large enough in order to avoid bias on the simulated data sample. Its value for the several data samples is reported in Tab. 4.5, together with the number of events which trigger the detector. The count of the number

LIST		
KEYS		
CONF	2	C Select the detector configuration
NCPL	1	C CENTRAL CONVERTER PLANES (¡20) (1 PLAN =0.5cm)
CMAT	2	C CENTRAL CONVERTER MATERIAL (1=Fe, 2=Pb)
ZCVR	13.	C SELECT ZCONV...(cm) (Quota of converter)
NTPL	0	C ROOF CONVERTER PLANES (¡20) (1 PLAN = 0.5cm)
TMAT	1	C SELECT ROOF CONVERTER MATERIAL (1=Fe, 2=Pb)
NFMP	1	C SELECT # OF FOM1 PLANES (0-10)(1 PLAN = 5cm)
ZROF	250.	C SELECT ROOF QUOTA (cm) (15.cm ¡ Z0ROOF ¡ 390.cm !!!)
ZGEN	13.5	C Quota of particle generation
XRDM	70000. 70000.	C random sampling of shower core on area (DX x DY)...
BACK	400.	C Simulate a Poissonian PAD-DIGIT Background (D=0.):
	C EXTERNAL EVENT INPUT...	
GTYP	2	C ... TYPE (1='EPAS', 2='CORSIKA', 3='HADRAS'):
	C ...Input FILE NAME:	
INPU	1='UNFM'	C INPU 1='FORM' INPU 1='ZEBR'
*FIEV	'.DATDAT_20031207fotoniDAT201120'	
	C EXTERNAL EVENT OUTPUT...	
OUTP	1='FORM'	C OUTP 1='ZEBR' OUTP 1='UNFM'
*FOEV	'./DAT/DAT_20031207/fotoni/DAT201120.form'	
MTRG	20	C Trigger configuration
	C # DIRECTIVE DATA CARDS #	
HITS	1	to evaluate the hits
DIGI	1	to evaluate the digitisings
TRAK	1	to track the particle
	C # SET PHYS. PROCESS IN TRACKING #	
ANNI	1	
DCAY	1	
BREM	1	
COMP	1	
DRAY	1	
HADR	2	
LOSS	1	
MULS	1	
MUNU	0	
PAIR	1	
PFIS	2	
PHOT	1	
CUTS	.001 .00040 .001 .001 .001 .001 .001 .001 .001 .01	
	C SET DETECTORS	
SETS	'RPCH'	
	C # GENERATION OF THE KINEMATICS #	
KINE	1=9 11=0.	
	C # INPUT/OUTPUT DATA CARDS #	
DEBUG	1 = 0	from this event
DEBUG	2 = 0	to this event
DEBUG	3 = 10	with this frequency
SWIT	6 = 6	
SWIT	7 = 5	
TIME	3=0	

Table 4.4: *Input file for ARGO-G.*

of muons contained in the showers and hitting the detector surface has required some modifications to the standard version of ARGO-G, in order to associate to each multiplicity value the corresponding reconstructed event.

Data Sample Type	A_g (m^2)	N$_{trigger}$	Energy Range
Photons	22 A$_{\text{Argo}}$	108268	1TeV-50TeV
Photons	700×700	36388	50TeV-100TeV
Protons	30 A$_{\text{Argo}}$	90678	1TeV-50TeV
Protons	700×700	46379	50TeV-100TeV

Table 4.5: *Generation area and number of events which trigger the detector.* $A_{Argo} = 11250\ m^2$.

4.4.3 Data sample reconstruction

The ARGO-G output file constitutes the input file for the reconstruction program Medea++. The event reconstruction is performed by the program developed by the Argo collaboration called Medea++. The language code is C++. It goes through three levels of reconstruction:

- The zero level, RecLevel0, is applied only to true data in order to decode the DAQ input file and to convert the event format to be elaborated in the next reconstruction level. Monte Carlo data do not need the decoding procedure, therefore the reconstruction of this kind of event begins from the first level of reconstruction RecLevel1.
- RecLevel1 performs five operations:
  1. It connencts each hit to the pad to which it is associated. Thus from a hit, the element of the detector to which it corresponds can be accessed and for each detector element the corresponding hits can be retrieved.
  2. It rejects the hits that are in the detector elements which are not active, broken or not properly working.
  3. It sorts the hits according to the time.
  4. It applies the noise filter which reduces the number of the hits which are believed to be due to the background and not to the air-shower particles.

5. It performs the time calibration.

- The second level of reconstruction, RecLevel2, performs the reconstruction of the direction and core position of the air showers in three steps:

  1. all the hits selected by the Noise Filter are fitted according to a plane function;
  2. the core position is calculated;
  3. the estimation of the core position is used to perform a conical fit to the hits.

The final results obtained with the RecLevel2 level are stored in an object called shower, which can be accessed by the user. The algorithms available for the core position calculation are described in [96]. In this work the shower core has been reconstructed using the algorithm called Likelihood2 and the conical fit has been performed. Also the reconstruction program has been modified in order to allow the reading of the muon multiplicity.

4.4.4 Events normalization

The simulated and measured [62] emission spectra of the Crab nebula are respectively:

$$\phi_{gen} = \frac{dN}{dtdSdE} = k_g E^{-1} \tag{4.25}$$

$$\phi_{Crab}(E) = k_m E^{-2.49} = 3.2 \cdot 10^{-7} E^{-2.49} \mathrm{m}^{-2} \mathrm{s}^{-1} \mathrm{TeV}^{-1} \tag{4.26}$$

The simulated spectral index differs from the measured one. Therefore the appropriate weight ($E^{-1.49}$ in the case of the Crab nebula) must be applied to the considered distributions of the physical quantity relative to the reconstructed events. The number of events must also be normalised, in such a way that the number of detected primary particles, N_{p}, is:

$$N_{\mathrm{p}} = N_{(\mathrm{p,w})} \frac{k_m}{k_g} \tag{4.27}$$

where $N_{(\mathrm{p,w})}$ are events weighted in order to take into account the right energy slope.

The value of the parameter k_g which describes the intensity of the simulated flux, is due to the number N_g of the simulated events and to the value of the generation area A_g over which they are distributed. By using the basic relation:

$$N_g = k_g \int_{E_{range}} E^{-1} dE \int_S dS \int_T dt = k_g \int_{E_{range}} E^{-1} dE \int_T A_g \cos\theta(t) dt \tag{4.28}$$

k_g is given by

$$k_g = \frac{N_g}{\int_{E_{range}} E^{-1} dE \int_T A_g \cos\theta(t) dt} \tag{4.29}$$

Chapter 5

Background rejection by muon identification in EAS

In this work, the possibility for the Argo experiment to detect point-like sources at energies up to tens of TeV, and in particular to study the emission spectrum of the Crab nebula at the highest energy ever observed, has been investigated. The importance of this observation has been explained in Chapter 2: it could help clarify the relevance of hadron acceleration.

In order to reach this goal, an upgrade of the experimental setup has been proposed: the enlargement of the active surface of the detector with respect to the original designed size, and the introduction of some muon identification system.

In the VHE range, the point-like source fluxes are known to decrease according to a negative power law with the energy rise: the extension of the active surface of the apparatus would allow an increase in the number of photon-initiated showers detected. Moreover, these fluxes are known to be three orders of magnitude lower than the overall cosmic ray flux. Thus, rejection of the cosmic ray background is one of the main concerns in γ-ray astronomy. The detection of point-like sources is possible within a solid angle chosen in such a way as to optimise the ratio between the signal and the background, which is uniformly distributed. Therefore, the achievement of a good angular resolution is very important.

However, the background can be further rejected by exploiting the differences in composition and shape between γ-ray-initiated showers and hadron-initiated ones. In the Argo experiment, a hadron - photon separation algorithm based on a multifractal analysis of the images left on the detector by the two kinds of shower, is being developed [67]. Background reduction by means of muon identification is now also being investigated by Argo. This technique exploits the different muon content of the two types of shower.

This Chapter is aimed at evaluating the improvement that the introduction of a muon identification system would bring to the point source detection. Therefore, the Q factor, the quantity which measures the effectiveness of any given background rejection method, has been estimated. In this work, the effectiveness of the method is tested on the Crab nebula, the standard "candle" for γ-ray astronomy: the sensitivity to the nebula has been evaluated with the improved configuration of the detector. The reduction of the background obtained with the use of the muon identification would allow the study of the Crab spectrum at energies of the order of tens of TeV. The application of this technique could allow to distinguish among the several possible scenarios for the behaviour of this spectrum.

5.1 The muon identification method

It has already been explained that background rejection by means of the muon identification method relies on the count of the number of muons present in the air-showers. Figure 5.1 shows the total muon content, at 4300 m a.s.l., in air-showers generated by protons (above) and photons (below) as a function of the primary energy, from 1 TeV up to 50 TeV. The number of muons contained in hadronic showers is quite large and increases as a function of the energy of the primary particle. Photon-initiated showers show the same behaviour, but they are poor in muons. Therefore, the cascades detected by the apparatus could be identified as photon- or hadron-generated air-showers based on their different muon content. The higher the primary energy, the more efficient the method is expected to be.

The Yanbajing site in Tibet at 4300 m a.s.l. is a particularly suitable location to experiment this background rejection technique: indeed, the number of muons in the showers

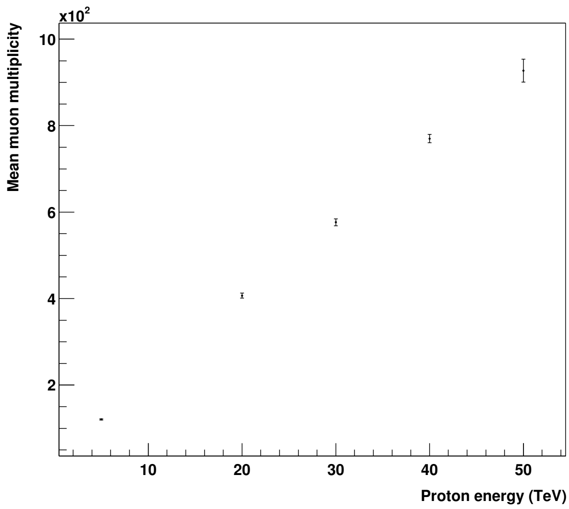

(a)

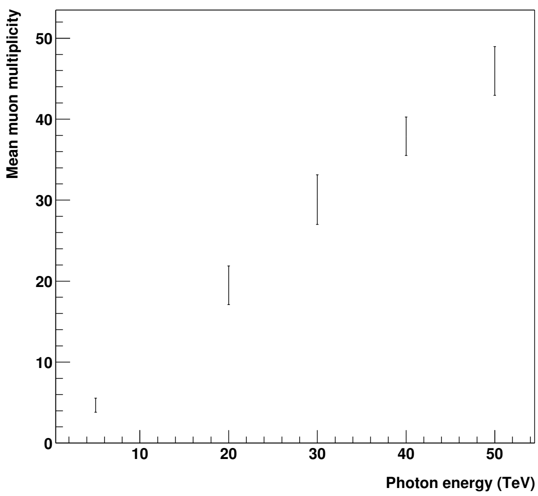

(b)

Figure 5.1: *The total number of muons present in proton (a) and photon-initiated (b) air-showers as a function of the primary energy at 4300 m a.s.l.*

grows with the altitude.

5.1.1 Upgrade of the Argo detector

The standard configuration of the detector includes a central "carpet" surrounded by a ring (Fig. 5.2, left). As already stated, the introduction of the muon identification technique requires an upgrade to this configuration. Because of the high energies considered,

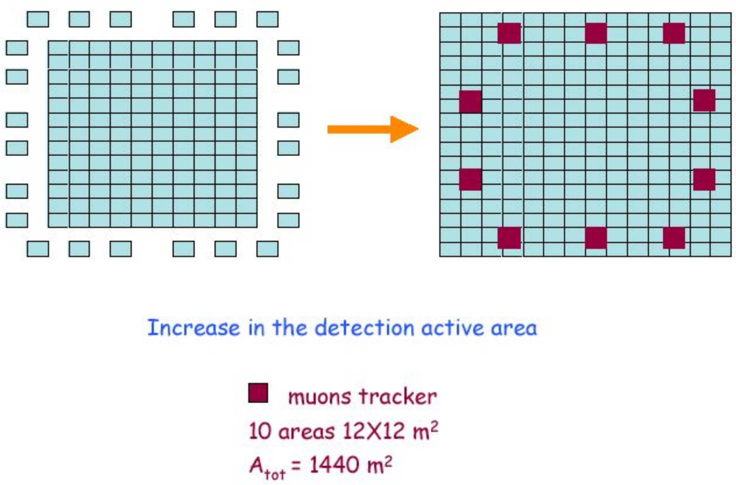

Figure 5.2: *The standard configuration of the Argo detector (left) and one of the proposed upgraded configuration consisting of about 1500 m^2 of active surface (right). The light squares represent clusters of RPCs, the dark ones the muon trackers.*

a detector layout with a larger number of active elements (RPCs) has been simulated in this work, in order to enlarge the sensitive area: the empty space between the carpet and the ring, and among the elements of the ring itself has been filled with RPCs, thus obtaining the configuration shown in Fig. 5.2, right.

The next change needed is the addition of a muon tracker. The effectiveness of the muon identification technique depends on the total number of muons populating the shower which Argo can detect. Therefore, it is important to establish the appropriate muon detection surface. Of course the larger the tracker surface, the greater the number of muons detected and the greater the efficiency. However, the cost of the detector must also be taken into account. Thus, in this work two values have been proposed for the detection surface: first, about 1500 m^2 organised in ten towers have been considered, each with a detection area of 144 m^2 (Fig. 5.2, right), and second, four larger detectors with a total active area of 2500 m^2 have been supposed to operate. The quality factor has been calculated in both configurations. Some very general constraints have been imposed on the tracker design: the muon detectors are constituted by layers of tracker interspersed with concrete absorber. The thickness of the latter determines the minimum energy threshold for the detected particles. Photons, electrons and muons are the most abundant secondary particles at ground. Photons and electrons generate electromagnetic showers in the absorber, while muons essentially loose energy by ionisation. In principle, the lower this energy threshold, the larger the number of particles (and in particular muons) detected.

The distribution of the muon multiplicity in air-showers generated by protons with energy equal to 40 TeV and collected on a surface of about 1100 m^2 is shown in Fig. 5.3, for values of the minimum muon energy considered ranging from 500 MeV to 1 GeV (with steps of 100 MeV). These two energy values correspond, respectively, to about 1m of concrete thickness and more than 2 m [1]. The average muon number slightly changes: lowering the energy threshold does not bring a noteworthy rise in the average value of the muon number, while it could enhance the probability of misidentification. The goal is to collect as many muons as possible, while keeping a high purity in the muon sample in order to reduce the probability to reject photons instead of protons.

Figure 5.4 shows the energy distribution at 4300 m a.s.l. of secondary photons (a) and electrons (b) contained in photon-initiated showers having energy from 1 TeV up to 100 TeV, whose direction points to the Crab nebula. 99.9% of the photons and electrons have energy below 20 GeV. The radiation length in concrete is 26.7 g cm^{-2} (10.7 cm) and the critical energy $E_c \sim 38$ MeV. Electromagnetic showers generated in concrete by secondary photons, electrons or positrons with energy equal to 100 GeV reach their maximum development at about 12 radiation lengths, which correspond to about 1.3 m of concrete. Therefore, there is no need for a highly segmented tracker and the absorber thickness can be assumed equal to about 2 m: thus all secondary particles producted by photon primaries with energy from 1 TeV up to 100 TeV could be absorbed, except for muons with energy greater than about 1 GeV.

[1]The minimum energy loss in concrete is 1.711 MeV$g^{-1}cm^2$. The density of concrete is ~2.5 g cm^{-3}

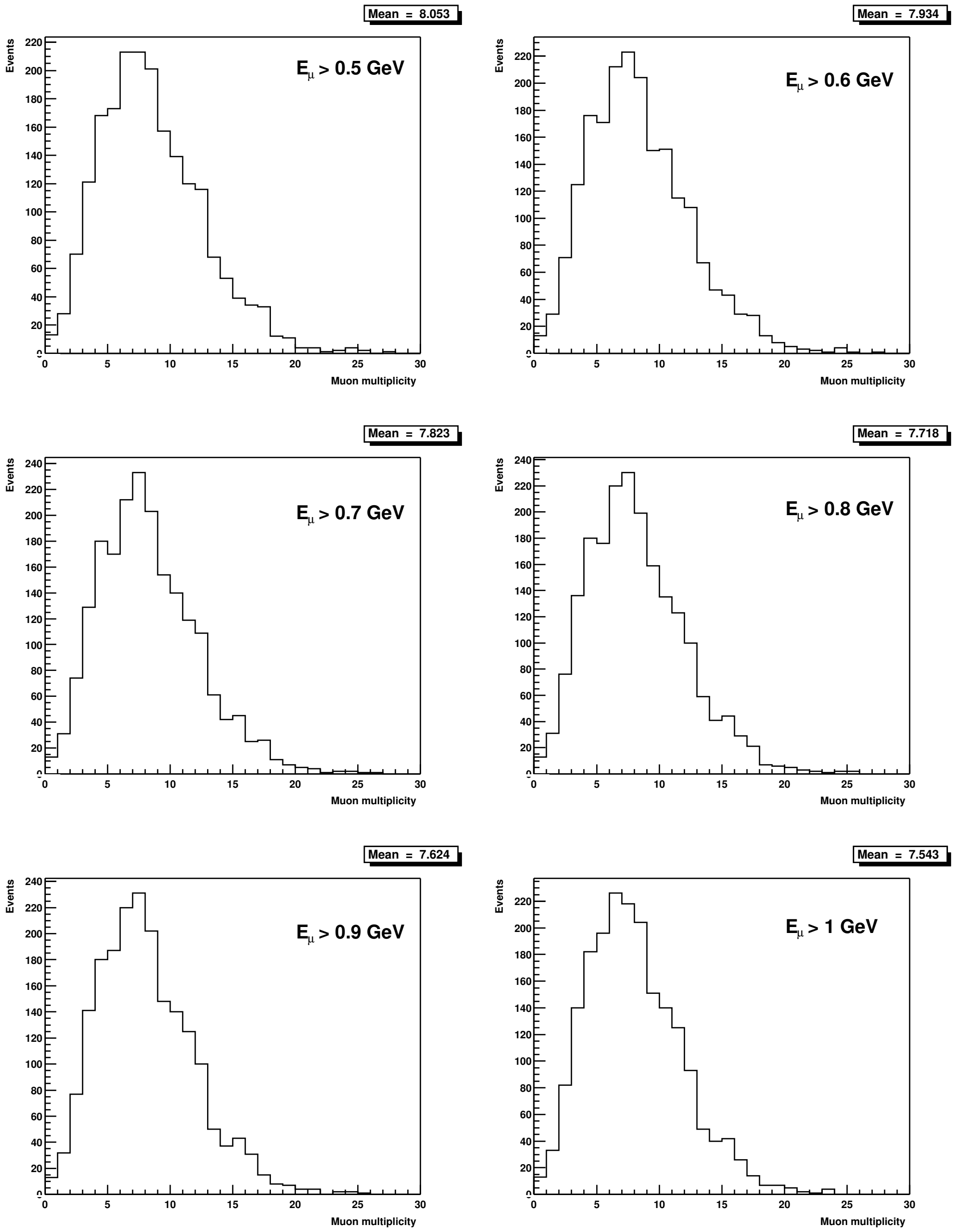

Figure 5.3: *Muon multiplicity distribution relative to proton-initiated air-showers with primary energy equal to 40 TeV and with a collection surface of about 1100 m^2, for different values of the minimum muon energy.*

The position of the towers, corresponding to the space between the carpet and the ring, has been chosen only according to building constraints: in fact the spatial distribu-

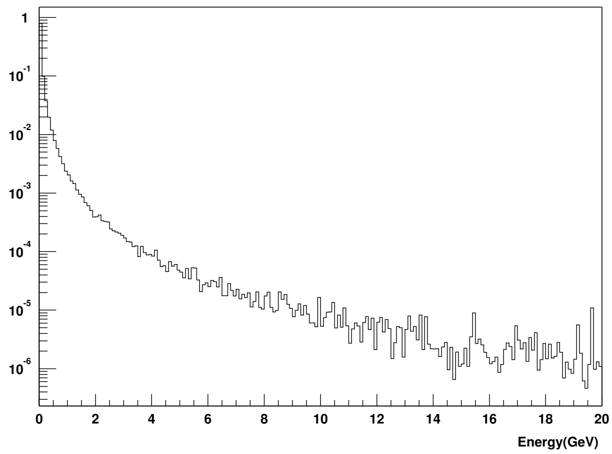

(a)

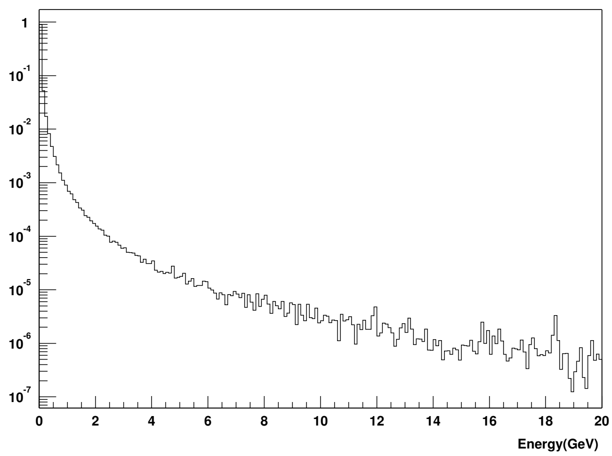

(b)

Figure 5.4: *Energy distribution at 4300 m a.s.l. of secondary photons (a) and electrons (b) in electromagnetic air-showers generated by the photons emitted from the Crab nebula in the range from 1 TeV to 100TeV.*

tion of muons from all air-showers, whose cores are randomly distributed over a large area including the detector surface, is flat. In the simulation, no specific assumption has been made for the technology that will be used to construct the detector: the results reported in this work assume that the muon detector efficiency, in the energy range of interest, is 100%.

In Fig. 5.5 the average number of muons contained in one event and falling on the ten tracking towers is plotted as a function of the primary energy for photon-(a) and proton-initiated (b) showers whose secondary particles hit more than 1000 pads. The corresponding primary annual rates as a function of their energy are shown in Fig 5.5c and d, respectively. These events satisfy other conditions required in the simulated data analysis and explained in the next Sections. As can be seen, the number of muons present in a triggered event can be used as a discriminating variable between photon-induced and hadron-induced showers.

5.1.2 Correlation between pad multiplicity and energy

Extensive air-shower particle detector arrays sample atmospheric showers by recording the charged secondary particles reaching it, their hitting times and their positions. The shower arrival direction and the core position can be deduced from the measured times and positions, while, as discussed in Sec. 4.1, the number of charged particles is related to the energy of the primary particle initiating the air-shower. Unfortunately, because fluctuations of the shower size (the number of charged particles in a shower) are very large, the energy of individual primary particles cannot be univocally determined: the number of secondary particles contained in air-showers generated by identical primaries varies enormously from one event to the other because of the interaction with the atmosphere. The main sources of fluctuations are the altitude at which the first interaction occurs and its nature. Moreover, because of the different air-shower development relative to the different kinds of primary particle, a proton initiated shower could be mistaken for a less energetic photon initiated one. The size of an event observed by the detector depends not only on the altitude interaction point and on the shower development, but also on the arrival direction and the core position. Usually a fiducial area is

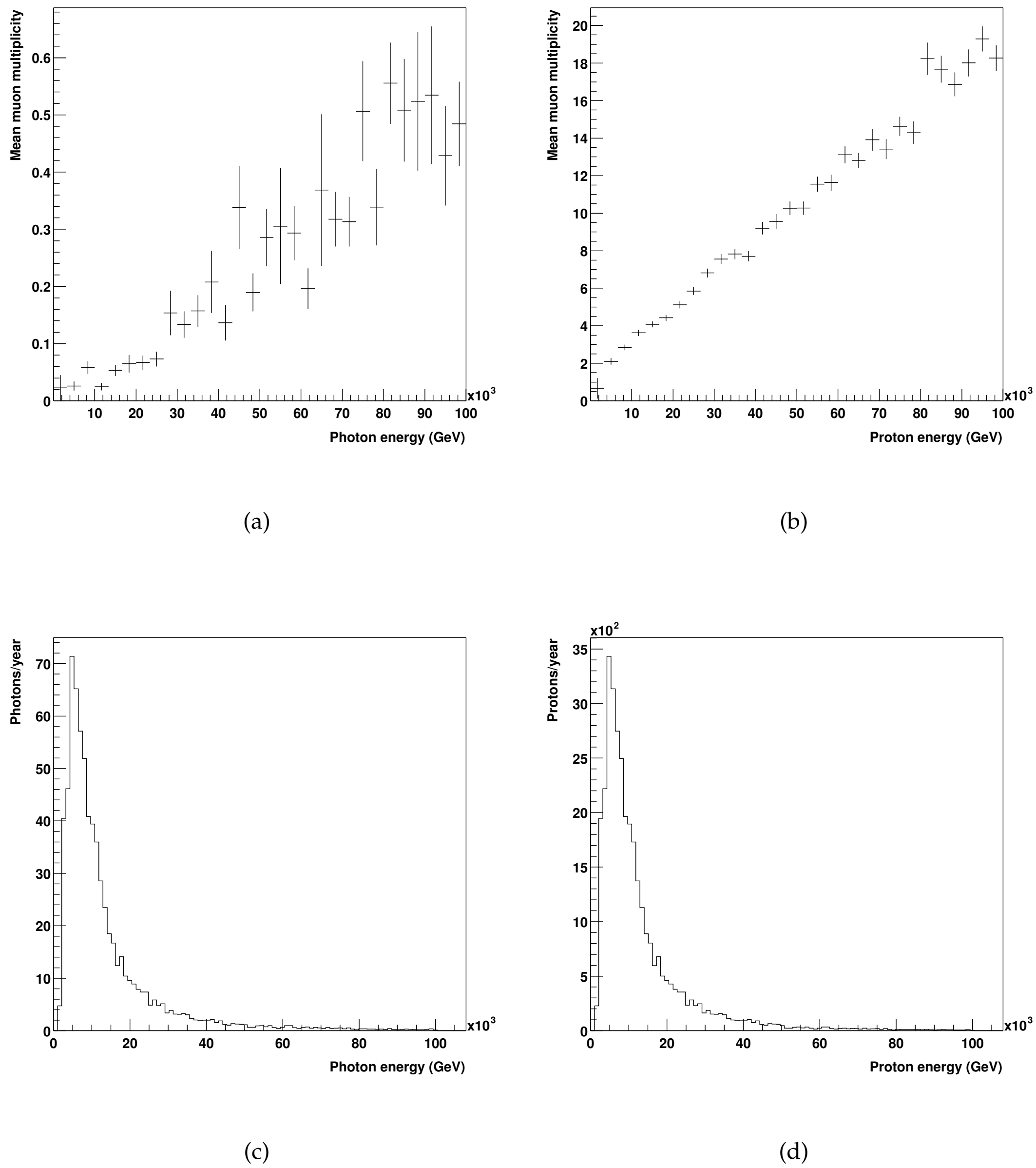

Figure 5.5: *Average muon multiplicity as a function of the primary energy of the air-showers generated by photons (a) and protons (b) and the corresponding photon (c) and proton (d) rates as a function of their primary energy. The conditions applied are the ones listed in Sec. 5.2.2.*

defined: all the events whose core falls within this area centered on the detector center, are selected. As a result, an estimate of the energy can only be given on a statistical basis for a given sample of events from the measurement of their size. Therefore the measured physical quantities are evaluated as a function of the event size whose distribution also depends on the event selection applied to calculate these quantities. This is a subtle point: the shower size is experiment-dependent and the only way to compare results from different experiments is to correlate it to the absolute scale of energy. In the case of the Argo experiment the size is measured by the pad multiplicity. In this work, the whole range of pad multiplicity is subdivided in a number of unlimited intervals (multiplicity greater than 1000, 2000, 3000 and so on) integrated on the whole angular range considered. The physical quantities are estimated as a function of these intervals, each of which is associated to the median energy of the events belonging to that range. The correlation between pad multiplicity and median energy has been calculated for each sample of conditions in which the physical quantities are estimated. Most plots shown in the following carry both energy and pad multiplicity scales.

5.1.3 The quality factor Q

The background rejection efficiency can be estimated by means of the quality factor Q, defined as

$$Q = \frac{\epsilon_\gamma}{\sqrt{1-\epsilon_B}}, \tag{5.1}$$

where ϵ_γ and ϵ_B are respectively the γ identification efficiency (the fraction of showers generated by photons and recognised as such) and the background identification efficiency (the fraction of showers generated by hadrons and recognised as such). Q depends on the energy of the primary particles hitting the atmosphere: its behaviour as a function of the energy must be determined.

The definition of the Q factor in Eq. 5.1 allows writing the sensitivity as

$$S_Q = \frac{N_\gamma \cdot \epsilon_\gamma}{\sqrt{N_B \cdot (1-\epsilon_B)}} = \frac{N_\gamma}{\sqrt{N_B}} \cdot Q \tag{5.2}$$

where N_γ and N_B are the number of detected air showers initiated by γ-ray and ordinary cosmic ray respectively. These quantities have already been defined in Eq. 3.1. Here, the numerator represents the overall number of photons identified with the chosen technique, while the denominator is the fluctuation of the background events which are left after the identification. So, Q is a measurements of the improvement obtained on the sensitivity, due to the introduction of the identification method. In this work, both the Q factor and the sensitivity to the Crab nebula as a function of the minimum pad multiplicity are calculated.

5.1.4 Evaluation of the Q factor

The method to calculate the identification efficiencies ϵ_γ and ϵ_B is straightforward. The distributions of the number of muons per event relative to photon- and proton-generated showers are obtained. Events are then identified as photon or proton type, based on a cut on the number of muons. For example, if the cut value is set at 2 muons, then an event containing 2 or more revealed muons will be tagged as a proton-generated shower, otherwise as a photon-generated one. Figure 5.6 shows the distribution of the number of muons for both protons (above) and photons (below), in the case of a muon detector surface of about 1500 m^2. The cut value is indicated by the vertical line. So all protons on the right side of the line are identified as such, while photons on the left side of the same line are identified as such. Now the Q factor can be calculated using the Eq 5.1. Several values for the quality factor can be estimated, depending on the different cuts set on the number of muons: Fig. 5.7 shows the behaviour of the rejection factor Q versus the number of muons chosen as cut value in a particular configuration (number of hit pad larger than 2000 and muon detection area equal to about 1500 m^2). For lower values of the cut the Q factor is higher because a greater number of protons can be identified and the number of photons tagged as protons and therefore rejected is not significant. The Q factor as a function of the median energy is showed for different values of the discriminating muon number in Fig. 5.8a and b in the case of a muon detection surface of 1500 m^2 and 2500 m^2 respectively. Its rise with the energy is due to the fact that at higher energy the average number of muons present in proton-initiated air-showers increases, thus allowing a better discrimination between signal and background. This estimate of the background rejection power has been performed with the upgraded apparatus and applying the conditions subsequently described in Sec. 5.2.2 when calculating the sensitivity to the Crab nebula.

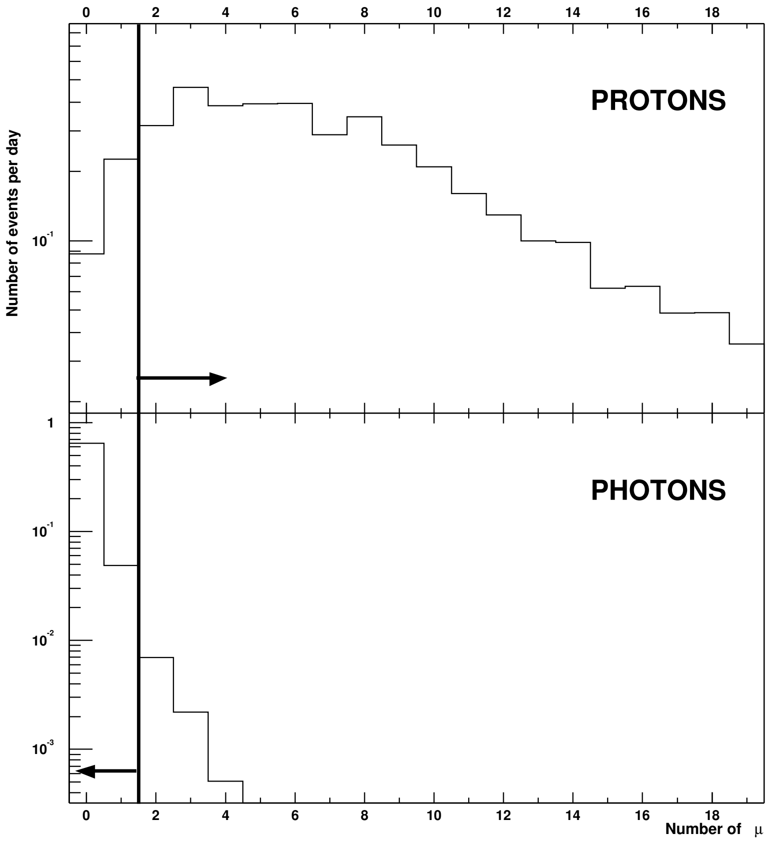

Figure 5.6: *The distribution of the number of muons per event, detected with the apparatus described in Section 5.1.1 for proton-initiated (above) and photon-initiated (below) showers. The area on the right (left) side of the vertical line representing the cut value, is equivalent to the number of protons (photons) identified as such.*

5.2 Sensitivity to the Crab nebula

γ-ray sources are identified within an appropriate solid angle through the enhancement observed in the distribution of the events collected in the appropriate angular region. The significance of the detected enhancement is evaluated with the so-called sensitivity, defined in Eq. 5.3 as the ratio of the number of photons detected N_γ to the statistical fluctuation of the background.

$$S = \frac{N_\gamma}{\sqrt{N_B}} \tag{5.3}$$

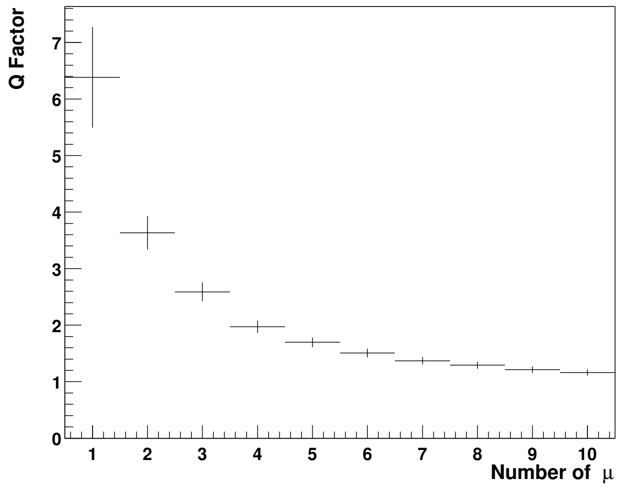

Figure 5.7: *Q versus muons number for minimum pad multiplicity equal to 2000.*

S measures the excess of signal events above background in units of standard deviations. The number of detected signal and background events, photons and protons respectively, is calculated starting from the number of reconstructed events (N'_γ and N'_B) satisfying the appropriate requirements. Details of how these numbers are extracted from the simulation are reported in Sec. 4.4. In terms of N'_γ and N'_B the sensitivity is:

$$S = \frac{N'_\gamma f_\gamma}{\sqrt{1.2 \cdot N'_B \Delta\Omega(\psi)}} \tag{5.4}$$

where $\Delta\Omega(\psi)$ is the observational solid angle corresponding to an opening ψ and f_γ is the fraction of photons viewed by this aperture. As usual, in this work the sensitivity has been estimated for 1 year of data taking. The background to a good approximation is only constituted by protons. Helium nuclei are taken into account by increasing by 20% the number of protons. The calculation of the sensitivity to the Crab nebula with the standard and upgraded configuration of the detector is presented in the next Sections.

5.2.1 Expected sensitivity with the Argo standard setup at high energy.

In the Argo usual configuration, the expected sensitivity to the Crab nebula has already been calculated in [64] at energies up to TeV. Here, the estimate of the sensitivity has been

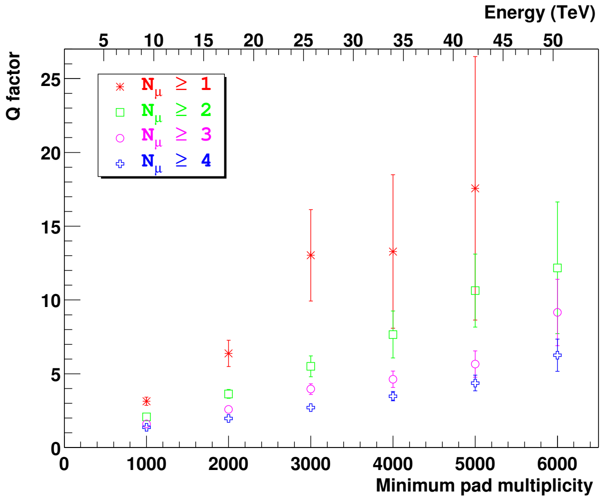

(a)

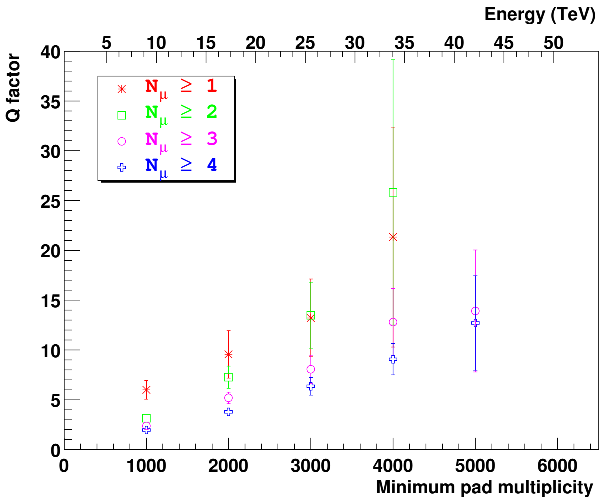

(b)

Figure 5.8: *Q factor as a function of the minimum pad multiplicity and the median energy for different values of the number of muons N_μ chosen to discriminate among the electromagnetic and hadronic showers in the case of a muon detection surface of 1500 m^2 (a) and 2500 m^2 (b).*

evaluated at higher energies, under the following assumptions:

- The Crab nebula spectrum simulated is the one measured by the Whipple collaboration [62]:
$$\frac{\mathrm{d}N}{\mathrm{d}E} = 3.2 \cdot 10^{-7} E^{-2.49} \;\; \gamma\, \mathrm{m}^{-2}\mathrm{s}^{-1}\mathrm{TeV}^{-1} \tag{5.5}$$

- The simulated proton flux on the top of the atmosphere is [63]:
$$\frac{\mathrm{d}N}{\mathrm{d}E} = 8.98 \cdot 10^{-2} E^{-2.74} \quad \mathrm{p}\, \mathrm{m}^{-2}\mathrm{s}^{-1}\mathrm{sr}^{-1}\mathrm{TeV}^{-1} \tag{5.6}$$

- The standard geometrical setup of the Argo detector is the one sketched on the left side of Fig. 5.2.

- Only events whose reconstructed core falls inside the "fiducial area" A_{f} = 80×80 m^2 and with the reconstructed zenith angle $\theta \leqslant 30°$ are selected.

- For high values of pad multiplicity, the observational opening angle is 0.29°

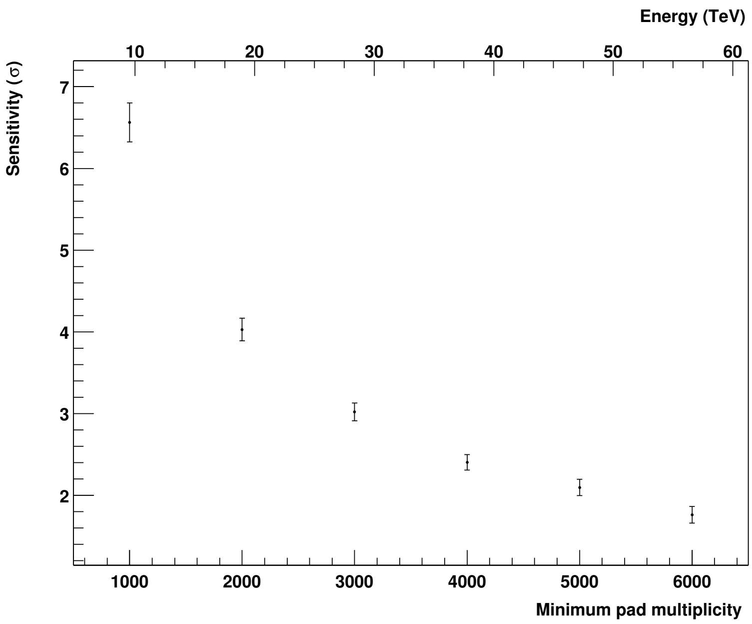

Figure 5.9: *Integrated sensitivity as a function of the minimum pad multiplicity and median energy with the standard configuration of the apparatus.*

In Fig. 5.9 the integrated sensitivity in terms of standard deviations is plotted as a function of the minimum pad multiplicity and the median energy. The error bars stand for the statistical error. There is good agreement with [64].

5.2.2 Expected sensitivity in the upgraded Argo setup

The typical energy spectrum from γ-ray sources is well described by a negative power law: the higher the emission energy, the lower the number of emitted photons. Therefore, the observation of astrophysical source spectra at elevated energies requires very large detectors as a means to detect a statistically significant number of photons.

Thus, in order to study the Crab nebula emission spectrum at high energy, a larger active surface has been considered. The new detector configuration has already been shown on the right side of Fig. 5.2. The active area has been increased in such a way

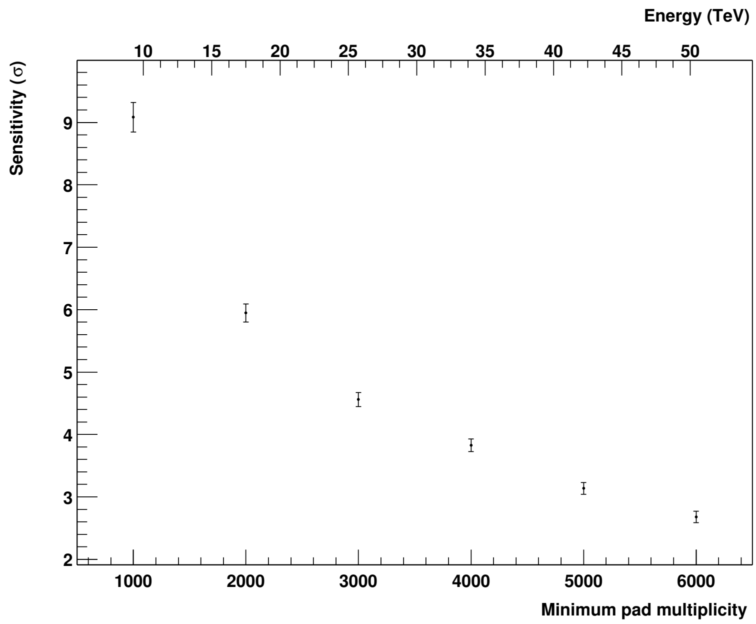

Figure 5.10: *Sensitivity as a function of the minimum pad multiplicity and median energy with the enlarged active detector surface, without muon identification.*

as to detect the maximum number of photons allowed at present. The rest of the conditions applied to estimate the Argo sensitivity to the "standard candle" has also been

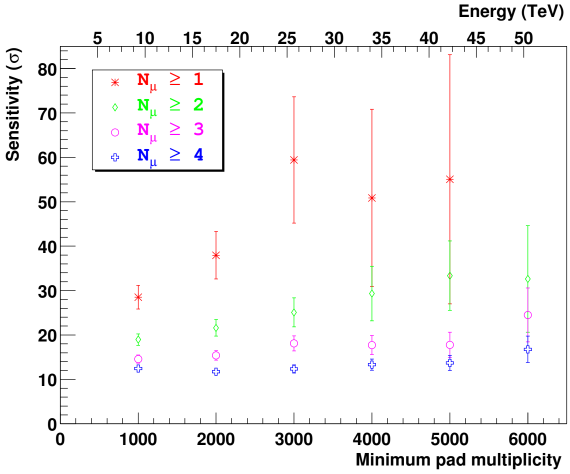

(a)

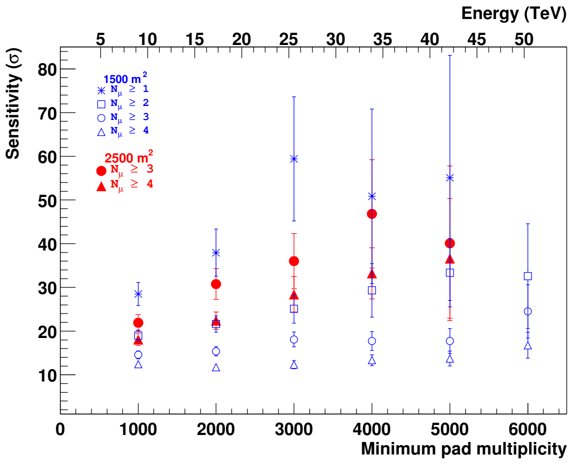

(b)

Figure 5.11: *Sensitivity as a function of the minimum pad multiplicity and the median energy with the enlarged active detector surface and with a muon detector of 1500 m^2. N_μ is the number of muons used to discriminate among the electromagnetic and hadronic showers (a). The sensitivity with a muon detector of 2500 m^2 is superimposed in the case of discriminating muon numbers equal to 3 and 4 (b).*

chosen with the purpose of maximising the number of detected events. Apart from the detector setup, two other conditions have been changed with respect to the calculation presented in the earlier Section: the "fiducial area" which is now A_f = 107X95 m^2, and the limit of the reconstructed zenith angle, $\theta \leqslant 40°$. The integrated sensitivity as a function of the minimum pad multiplicity and the median energy with the upgraded setup is plotted in Fig. 5.10. This estimate of the sensitivity does not exploit the background rejection achievable thanks to the muon identification while Fig. 5.11a shows the expected sensitivity as a function of the minimum pad multiplicity and the median energy when making use of this discrimination technique in the case of a detection surface of 1500 m^2, for different values of the muon number N_μ chosen to tag the events. Figure 5.11b shows again this sensitivity together with the sensitivity estimated in the case of 2500 m^2 detection surface, setting the value of the discriminating number of muons N_μ to 3 and 4. The sensitivity obtained in this second experimental configuration is higher for equal values of N_μ. In particular the results showed in Fig. 5.11b are in between those obtained using 1500 m^2 of muon detector with N_μ equal to 1 and 2.

5.3 Discussion on the possible Crab nebula cutoff

The background reduction achieved by means of the muon identification method is rather high. Thus, the study of the Crab spectrum at the highest energies can be faced. In particular, the ability of the Argo experiment to distinguish among two different behaviours of the Crab spectrum has been examined in the case of a muon detector surface of 1500 m^2. Two hypothetical scenarios have been considered:

- the energy spectrum has a cutoff at 40 TeV;
- the energy spectrum has a cutoff at 70 TeV.

The aim is to understand if these two situations can be separated with the help of the muon identification technique. The study has been performed on simulated data corresponding to three years of data taking. Figure 5.12 shows the total number of proton- and photon-initiated air-showers left after rejecting those containing 2 or more muons, as a function of the minimum pad multiplicity, in the two cases above. The two scenarios are best separated at with high values of the minimum pad multiplicity. The estimate has been performed with the conditions described in the previous Section.

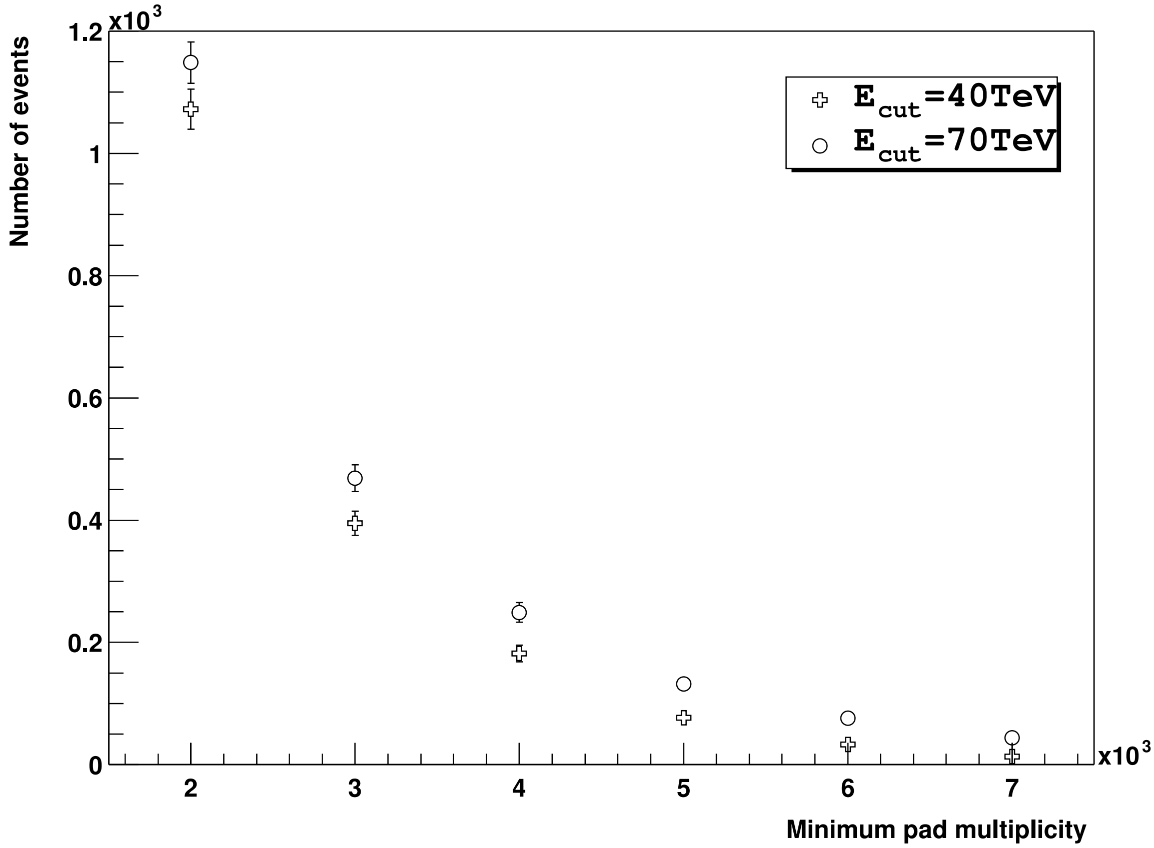

Figure 5.12: *Number of events as a function of the minimum pad multiplicity*

Figure 5.13 shows a zoom of both spectra in the pad multiplicity range 3000-7000. A fit to a negative power law, with three parameters is superimposed in Fig. 5.13a and b in the 70 TeV and 40 TeV cutoff scenario, respectively. In order to test the discrimination power for the two hypotheses, the same fit has been repeated, but with one parameter fixed to the value obtained for the other scenario: this results in a much worse agreement, as seen in Fig. 5.13c and d.

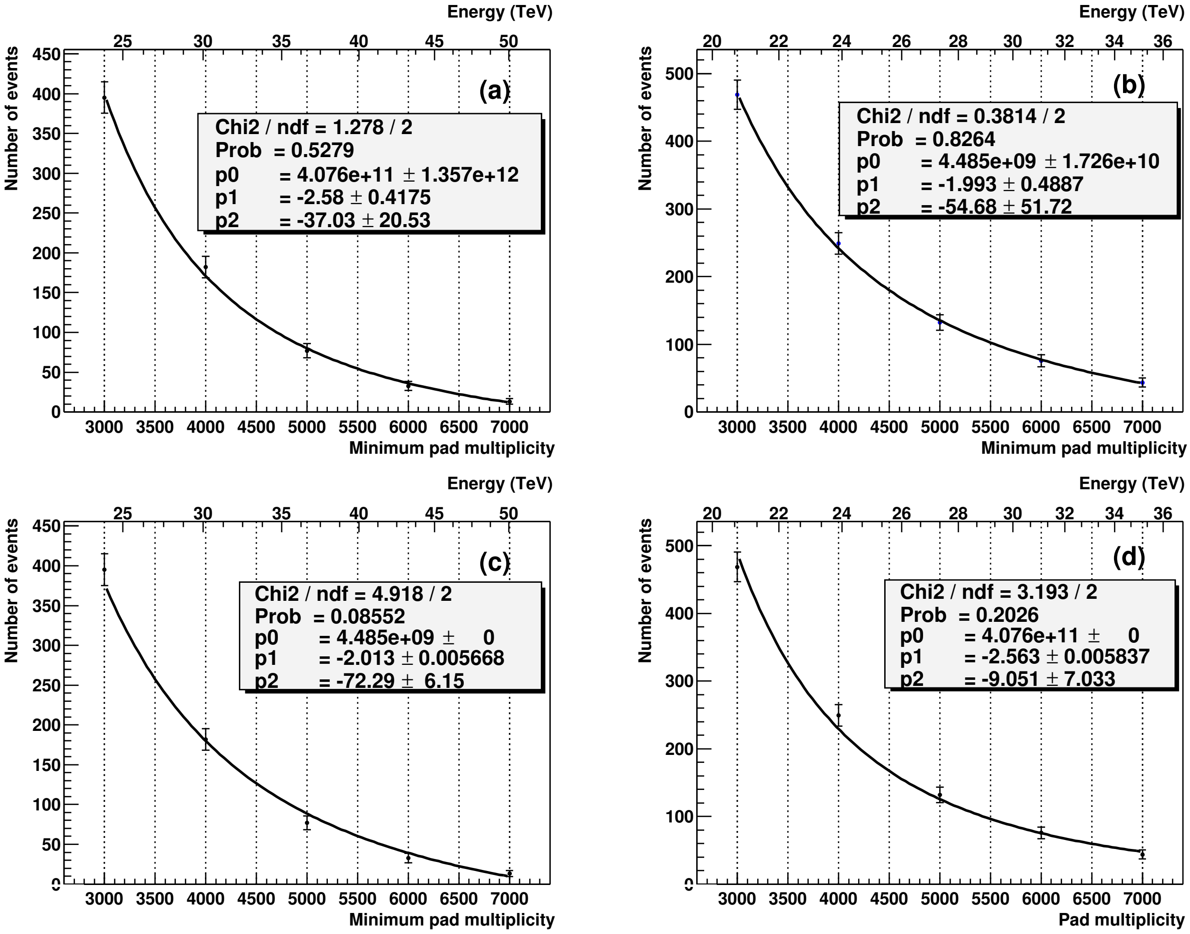

Figure 5.13: *Number of events as a function of the minimum pad multiplicity and the median energy with the result of the fits superimposed*

Conclusion

In this work a simulation study has been conducted, aimed at identifying and rejecting the background component, constituted by hadronic cosmic rays, in γ-ray detection performed with the Argo experiment at energies of tens of TeV. The identification of the hadronic cosmic component has been based on the muon content of detected air-showers. Indeed, hadron-initiated showers, unlike photon-initiated ones, are rich in muons. Thus, an air-shower containing less than a given number of muons, chosen as discriminating value, can be classified as generated by a primary photon, otherwise by a primary hadron.

In order to apply this background rejection method, the Argo collaboration is going to propose an upgrade of the experimental setup: first, the extension of the active surface of the apparatus in order to increase the number of detected signal events, required because of the low γ-ray flux at high energies; second, the introduction of a muon detector in order to perform muon identification and therefore reduction of the background component. The standard Argo simulation software has therefore been modified to include these configuration changes, in order to evaluate the background rejection effectiveness in the case of the Crab nebula detection. In this study, two values for the muon detection surface have been considered: 1500 m^2 and 2500 m^2.

First, the sensitivity to the "standard candle" for γ-ray astronomy has been evaluated in the original detector configuration at high energies without considering the improvement that the addition of muon detection and the extension of active surface could give: a signal with significance 6.5σ (4σ) is expected in one year of data taking at median energy equal to about 10 (20) TeV.

Then, using the upgraded detector configuration, the quality factor Q, which measures the discrimination power, has been estimated as a function of the median energy, for different values of the number of muons utilised in order to identify photon-initiated air-showers against hadron-initiated ones. The muon identification method as a background rejection technique has been shown to become interesting at a median energy around 10 TeV with the smallest apparatus considered. The quality factor Q has been showed to be a rising function of the energy: for example, when the discriminating muon multiplicity is set to 1, Q is about 3 (6) at a median energy of 10 TeV and about 13 (25) at a median energy of 35 TeV, when operating with a muon detection surface of 1500 m^2 (2500 m^2). This condition appears as the most favourable one.

These results cause the sensitivity to the Crab nebula to grow up to almost 20σ (40σ) at a median energy of 10 (20) TeV in one year of data taking with a muon detector of 1500 m^2. This means that, at these energies, a signal with 5σ significance would be detected in less than 6 days. Moreover, the Argo experiment would become effective also at higher energies: for one year of observation, at a median energy of 50 TeV the sensitivity is more than 50σ. The option of a larger detector (2500 m^2) would allow the achievement of these same results, using a safer discriminating cut on the number of muons. The large values of the Q factor at high energy compensate for the lowering of the Crab nebula flux at the same energy. This technique would allow the Argo experiment to detect and study the Crab nebula spectrum at the highest energy ever observed.

These results seem to be very promising. Another background rejection technique which is being explored by the Argo experiment is based on a detailed study of the shower images detected by the apparatus. In this case the Q factor reaches interesting values also at the lowest energies detectable by Argo. At high energies this technique seems to approach a limit, and indeed the Q factor seems to stabilise at a value equal to about 2. Thus, these two independent methods of background rejection are somehow complementary, and they can be used together to improve γ-ray detection.

Bibliography

[1] T.C. Weekes et al., *Phys. Rep.* **160**, 1 (1988)

[2] C. M. Hoffman et al, *Rev. Mod. Phys.* **71**, (1999)

[3] C. E. Fichtel et al., *ApJ* **198**, 163 (1975)

[4] K. Bennett, *Nuclear Physics B (Proc. Suppl)* **14B** 23-34 (1990)

[5] V. Schnfelder et al., *Memorie della Societa Astronomica Italiana*, **67** 143 (1996)

[6] G. Kanbach et al., *Space Sci. Rev.* **46** 69 (1988); D.J. Thompson et al., *Astrophys. J. Suppl.* **86** (1993)

[7] T.C. Weekes et al., *ApJ* **342**, 379 (1989)

[8] R.C. Hartman et al., *ApJS* **123**, 79-202 (1999)

[9] R. Ong, *astro-ph/0304336* (2003)

[10] Asakimori et al., *ApJ* **502**, 278 (1998)

[11] Thomas K. Gaisser, *Cosmic Rays and Particle Physics* **Cambridge University Press**, (1990)

[12] R. D. Blandford & J. P. Ostriker, *ApJ* **221**, L29 (1978)

[13] A. R. Bell *MNRAS* **182**, 147 (1978)

[14] P.O. Legage & C. J. Cesarsky, *A&A* **118**, 223 (1983)

[15] V. Schnfelder, *The Universe in Gamma Rays* **Springer** (2001)

[16] M. C. Begelman, R. D. Blandford, and M. J. Rees, *Rev. Mod. Phys.* **56**, 255 (1984)

[17] A.C. Phillips, *The Physics of Stars*, **Wiley & Sons** (1994)

[18] M. S. Longair, *High Energy Astrophysics* , Vol. I II **Cambridge University, London/New York** (1994)

[19] M. Tarenghi, *186th AAS Meeting, #41.02; Bulletin of the American Astronomical Society*, **Vol. 27** 869; http://www.eso.org/paranal

[20] J. J. Hester,The sixth Texas-Mexico conference on astrophysics **QB1 R384 v. 7** 90 (1998)

[21] M. C. Weisskopf*195th AAS Meeting, #96.01; Bulletin of the American Astronomical Society* **Vol. 31** 1514 ; http://chandra.harvard.edu/about/axaf_mission.html

[22] O. C. De Jager, and A. K. Harding, *Astrophys. J.* **396**, 161 (1992)

[23] Miller R.S, Westerhoff S. *Astropart. Phys.* **11** 379-393, (1999)

[24] P. Fleury, *Frascati Physics Series* **XXIV**, 305-324 (2002)

[25] F. Krennrich et al., *Astroparticle Physics* **8** 213-221 (1998)

[26] Barrau, A., et al., *Nucl. Instrum. Methods Phys. Res. A* **416** 278 (1998)

[27] J. A. Hinton, *New Astronomy Reviews* **48** 331-337(2004)

[28] F. Krennrich et al., *New Astronomy Reviews* **48** 345-349(2004)

[29] H. Kubo et al., *New Astronomy Reviews* **48** 323-329(2004)

[30] E. Lorenz, *New Astronomy Reviews* **48** 339-344(2004)

[31] P. Sokolsky, *Introduction to ultrahigh energy cosmic ray physics*, **Frontiers in physics**

[32] R. M. Baltrusaitis et al., *Nuclear Instruments and Methods* **A 240** 410-428 (1985)

[33] D. A. Williams et al., *New Astronomy Reviews* **48** 359-366(2004)

[34] J. Busson-Gordo, *New Astronomy Reviews* **48** 351-357(2004)

[35] T. Tumer *Astropart.Phys.* **11** 271-273 (1999)

[36] E. Blaufuss, *New Astronomy Reviews* **48** 513-518(2004) A. Atkins et al., *astro-ph/0403097* (2004)

[37] N. Gotting for the collaboration, *astro-ph/0310308* (2003)

[38] M. Catanese and T.C. Weekes *astro-ph/9906501* (1999) and references quoted therein

[39] R. J. Goret et al., *Astron. Astrophys.* **270**, 401 (1993)

[40] T. Tanimori et al., *Astrophys. J* **429**, L61 (1994)

[41] F. Krennrich et al., *23rd International Cosmic Ray Conference* **Vol. 1**, 251 (1993)

[42] M. Amenomori et al. *astro-ph/9909172* (1999)

[43] P. Sommers & J. W. Elbert, *J. Phys. G: Nucl. Phys* **13**, 553 (1987)

[44] A. M. Atoyan et F. A. Aharonian, *MNRAS* **278** , 525 (1996)

[45] C. F. Kennel et F. V. Coroniti, *ApJ* **283**, 694 (1984)

[46] C. F. Kennel et F. V. Coroniti, *ApJ* **283**, 710 (1984)

[47] J. J. Hester et al., *ApJ* **448**, 240 (1995)

[48] R. D. van der Meulen et al., *A&A* (1998)

[49] G. V. Jung, *ApJ* **338** , 972 (1989)

[50] L. M. Bartlette et al., *Ph.D. Thesis, University of Maryland* , (1994)

[51] O. C. De Jager et al., *ApJ* **457** , 253 (1996)

[52] F. A. Aharonian, *astro-ph/9803091* , (1998)

[53] W. M. Cheung, & K.S. Cheng, *ApJS* **90**, 827 (1994)

[54] M. Abbrescia et al., Astroparticle Physics with ARGO Proposal, 1996

[55] C. Bacci et al., The ARGO-YBJ Project, Addendum to the Proposal, 1998. These unpublished documents can be downloaded at the URL: http://www1.na.infn.it/wsubnucl/ cosm/argo/argo.html

[56] S. Mastroianni et al, *Proc XXVIII ICRC*, (2003)

[57] A. Surdo et al, *Proc XXVIII ICRC*, (2003)

[58] M. Iacovacci et al, *Proc XXVIII ICRC*, (2003)

[59] C. Bacci et al., *Nucl. Instr. Meth.* **A 443** 342 (2000)

[60] C. Bacci et al., *Nucl. Instr. Meth.* **A 508** 110 (2003)

[61] G. Di Sciascio et al, *Proc XXVIII ICRC*, (2003)

[62] A. M. Hillas et al. *ApJ* **503**, 744 (1998)

[63] T.K. Gaisser et al. *Proc XXVII ICRC*, 1643 (2001)

[64] S. Vernetto et al, *Proc XXVIII ICRC*, (2003)

[65] T. Di Girolamo, *Proc Incontro Nazionale di Astrofisica delle Alte Energie* to be published on Frascati Physics series

[66] S.Bussino and S.M.Mari, *Astroparticle Phys.* **15**, 65 (2001)

[67] I. De Mitri, F. Salamida and G. Marsella *astro-ph/0307535* (2003)

[68] B.Rossi *High-Energy Particles Prentice-Hall*, **Englewood Cliffs** (1952)

[69] K. Greisen, *Prog. Cosmic Ray Phys. 3* (1956) 1

[70] M. Unger, *hep-ex* **0309002** (2003) published in eConf **C030626:FRAP03** 2003, also in Tsukuba 2003, Cosmic Ray 1179-1182, also in Zeuthen 2003 Physics in collision 348-350

[71] O. C. Allkofer et al., Phys. Lett. **B36**, 425 (1971); C. A. Ayre et al., J. Phys. **G1**, 584 (1975); B. J. Bateman et al., Phys. Lett. **B36**, 144 (1971); M. P. De Pascale et al., J. Geoph. Res. **98**, 3501 (1993); P. J. Green et al., Phys. Rev. **20**, 1598 (1979); J. Kremer et al., Phys. Rev. Lett. **83**, 4241 (1999); M. Boezio et al., Phys. Rev. **D67**, 7 (2003)

[72] P. K. F. Grieder, *Cosmic Rays at Earth*, **Elsevier** (2001)

[73] K. Hagiwara et al., *Physical Review* **D66**, 010001-1 (2002)

[74] D. Heck, J. Knapp, J.N. Capdevielle, G.Schatz and T. Thouw, *Report FZKA* **6019**, (1998), Forschungszentrum Karlsruhe; http://www-ik.fzk.de/~heck/corsika/physics_description/corsika_phys.html

[75] J. Ranft, *Phys. Rev* **D51**, (1995) 64; preprint hep-ph/9911213 and hep-ph/9911232 (1999)

[76] J. N. Capdevielle et al., *Report* **KfK 4998** (1992), Kernforschungszentrum Karlsruhe

[77] N. N. Kalmykov and S. S. Ostapchenko, *Yad. Fiz.* **56** (1993) 105

[78] R.S. Fletcher, T. K. Gaisser, P. Lipari, and T. Stanev, *Phys. Rev* **D50** 5710 (1994)

[79] K. Werner, *Phys. Rep.* **232** 87 (1993)

[80] H. J. Drescher, M. Hladik, S. Ostapchenko, T. Pierog, and K. Werner, *Phys. Rep.* **350** 93 (2001)

[81] W. R. Nelson, H. Hirayama and D. W. Rogers, Report **SLAC 265** (1985), Stanford Linear Accelerator Center

[82] T. Stanev et al., *Phys. Rev.* D**32**, 1244 (1985)

[83] K. Greisen, *Prog. Cosmic Ray Physics III*, **J. G. Wilson ed. (North Holland Publishing Co., Amsterdam** 1 (1965)

[84] D. Heck, for the KASCADE Collaboration, *astro-ph/0103073* (2001) published in Tihany 2000, From e+ e- to heavy ion collisions 252-259

[85] H. H. Mielke et al., *J. Phys. G: Nucl. Part. Phys.* **20**, 637 (1994)

[86] G. B. Yodh et al.,*Phys. Rev.* D**27**, 1183 (1983)

[87] R. M. Baltrusaitis et al, *Phys. Rev Lett.* **52**, 1380 (1984)

[88] M. Honda et al., *Phys. Rev. Lett* **70**, 525 (1993)

[89] M. Aglietta et al. (EAS-TOP Coll.) in *Proc.* 25^{th} *Int. Cosmic Ray Conf.*, Durban (South Africa), **6**, 37 (1997)

[90] M. M. Block et al, *Phys. Rev.* D**62**, 077501 (2000)

[91] R. Brun et al., *GEANT - detector description and simulation tool*, CERN Program Library Vers. 3.21, W5013 (1993)

[92] T. Antoni et al. (KASCADE Collaboration) *J. Phys. G: Nucl. Part. Phys.* **25** 2161 (1999)

[93] A.D. Erlykin A.W. Wolfendale, *Astrop. Phys.* **9** 213 (1998)

[94] D. Martello, *ArgoYBJ-Note 001/02*

[95] C. Bleve et al., *ArgoYBJ-Note 002/03*

[96] D. Martello et al., *27th International Cosmic Ray Conference (ICRC)* **OG 2.5, Vol. 7** 2927 (2001)

Contents

Acknowledgements

I'm very glad I have had the chance to work in the Argo experiment during these last three years. I would like to thank all the people working in the Argo group in Rome for their useful suggestion and fruitful discussion. In particular I'm grateful to my supervisor Pio Pistilli.

I want to mention also the Argo collaborators in Lecce and Napoli for their availability and support: especially I'm indebted to Tristano Di Girolamo, Pino Di Sciascio and Daniele Martello.

A very special thank to Enrico.